EXPERIMENTAL AND THEORETICAL STUDIES OF NANOSTRUCTURED ELECTRODES FOR USE IN DYE-SENSITIZED SOLAR CELLS

A Dissertation
Submitted to the Graduate Faculty
of the
North Dakota State University
of Agriculture and Applied Science

By

Jiawei Gong

In Partial Fulfillment of the Requirements
for the Degree of
DOCTOR OF PHILOSOPHY

Major Department:
Mechanical Engineering

December 2016

Fargo, North Dakota

North Dakota State University
Graduate School

Title

Experimental and Theoretical Studies of Nanostructured Electrodes for Use in Dye-Sensitized Solar Cells

By

Jiawei Gong

The Supervisory Committee certifies that this ***disquisition*** complies with North Dakota State University's regulations and meets the accepted standards for the degree of

DOCTOR OF PHILOSOPHY

SUPERVISORY COMMITTEE:

Dr. Sumathy Krishnan
Chair

Dr. Xiangfa Wu

Dr. Long Jiang

Dr. G. Padmanabhan

Approved:

4/11/2017
Date

Dr. Alan Kallmeyer
Department Chair

ABSTRACT

Among various photovoltaic technologies available in the emerging market, dye-sensitized solar cells (DSSCs) are deemed as an effective, competitive solution to the increasing demand for high-efficiency PV devices. To move towards full commercialization, challenges remain in further improvement of device stability as well as reduction of material and manufacturing costs. This study aims at rational synthesis and photovoltaic characterization of two nanostructured electrode materials (i.e. SnO_2 nanofibers and activated graphene nanoplatelets) for use as photoanode and counter electrode in dye-sensitized solar cells. The main objective is to explore the favorable charge transport features of SnO_2 nanofiber network and simultaneously replace the high-priced conventional electrocatalytic nanomaterials (e.g. Pt nanoparticles) used in existing counter electrode of DSSCs. To achieve this objective, a multiphysics model of electrode kinetics was developed to optimize various design parameters and cell configurations.

The porous hollow SnO_2 nanofibers were successfully synthesized via a facile route consisting of electrospinning precursor polymer nanofibers, followed by controlled carbonization. The novel SnO_2/TiO_2 composite photoanode materials carry advantages of SnO_2 nanofiber network (e.g. nanostructural continuity, high electron mobility) and TiO_2 nanoparticles (e.g. high specific area), and therefore show excellent photovoltaic properties including improved short-circuit current and fill factors. In addition, hydrothermally activated graphene nanoplatelets (aGNP) were used as a catalytic counter electrode material to substitute for conventionally used platinum nanoparticles. Improved catalytic performance of aGNP electrode was achieved through increased surface area and better control of morphology. Dye-sensitized solar cells using these aGNP electrodes had power conversion efficiencies comparable to those using platinum nanoparticles with I^-/I_3^- redox mediators. Moreover, a multiphysics model at the device level was

developed to predict the power output characteristics of DSSC using different electrode materials. The developed model was validated by the experimental data acquired from lab-fabricated DSSCs. Further, parametric simulation was conducted to analyze the effect of series resistance, shunt resistance, interfacial overpotential, as well as difference between the conduction band and formal redox potentials on device performance. This model correlates the maximum power output of DSSC devices to various design and operating parameters, and it also provides insight into the working principles of newly designed devices.

ACKNOWLEDGEMENTS

I dedicate my deepest thanks to my advisor, Dr. Sumathy Krishnan, for her guidance, patience, kindness, and motivation during the development and completion of this dissertation. Without her persistent help and support, this dissertation would not be in the present form. Through her guidance, I have gradually developed into an independent researcher. Her enthusiasm, vision, and work ethic have always been an inspiration for me to overcome difficulties in research and life. During this Ph.D. study, I have learned from her not only the methodology to conduct research, but more importantly, the unwavering commitment to accomplish goals with faith, responsibility, and confidence. Her invaluable mentoring in my six years of graduate study will guide me throughout my entire life journey.

I am very thankful to my supervisory committee members Dr. Xiangfa Wu, Dr. Long Jiang, and Dr. Padmanabhan for their time and effort in guiding my work. In particular, I want to thank Dr. Xiangfa Wu for enlightening discussions and sharing his extensive knowledge on the device modeling and numerical methodology. I must thank Dr. Long Jiang for contributing his expertise in activated carbon materials as well as introducing me to Dr. Qiquan Qiao at South Dakota State University (SDSU).

Special thanks are given to Dr. Qiquan Qiao for providing me the opportunity to conduct experimental research in his lab. Without his support, this dissertation would not have been possible. In addition, I owe many thanks to all the lab mates at SDSU for numerous helpful discussions on topics of organic PV, dye-sensitized solar cells, and solar cell-battery integrated systems. I have to thank Mr. Sudhan Sigdel for providing his valuable time in my lab training, Dr. Hytham Elbohy for preparing materials used in device fabrication, Dr. Nirmal Adhikari for conducting TPV and TPC analysis, Dr. Zhengping Zhou for continuing the study on activated

graphene nanoplatelets, and Mr. Abu Mitul for opening the lobby door for me on many Sunday mornings.

Last but not least, I would like to express my gratitude to Chair Dr. Alan Kallmeyer for financially supporting my three conference trips. Also, I have to thank all secretaries and office staff in ME department for their always timely assistance and advice.

DEDICATION

This dissertation is dedicated to Ms. Lina Gong and Ms. Jing Liang.

TABLE OF CONTENTS

LIST OF TABLES

LIST OF FIGURES

LIST OF ABBREVIATIONS

AC .....Alternating current

aGNP .....Activated graphene nanoplatelets

BET .....Brunauer-Emmett-Teller

BJH .....Barrett-Joyner-Halenda

CE .....Counter electrode

CSP .....Concentrated solar power

CV .....Cyclic voltammetry

DC .....Direct current

DFT .....Density functional theory

DI .....Deionized

DMF .....Dimethylformamide

DOS.....Density of states

DSSC.....Dye-sensitized solar cells

EIS.....Electrochemical impedance spectroscopy

EQE.....External quantum efficiency

FESEM.....Field emission scanning electron microscopy

FF .....Fill factor

FTO .....Fluorine-doped tin oxide

GNP.....Graphene nanoplatelets

HOMO .....Highest occupied molecular orbital

IPCE.....Incident photon-to-electron conversion efficiency

IMPS .....Intensity-modulated photocurrent spectroscopy

I_{sc} .....Short-circuit current

J_{sc}.....Short-circuit current density

KOH.....Potassium hydroxide

LCOE.....Levelized cost of energy

LHE.....Light harvest efficiency

LUMO.....Lowest unoccupied molecular orbital

OPV.....Organic photovoltaics

Pt.....Platinum

PCE.....Power conversion efficiency

PV.....Photovoltaics

QSDFT.....Quenched solid density functional theory

SBH.....Schottky barrier height

SEM.....Scanning electron microscope

SSD.....Solid-state detector

TCO.....Transparent conductive oxide

TEM.....Transmission electron microscope

TPC.....Transient photocurrent

TPV.....Transient photovoltage

UV.....Ultraviolet

UV-Vis.....Ultraviolet-visible

V_{oc}.....Open-circuit voltage

XRD.....X-ray diffractometer

LIST OF SYMBOLS

k_e ..... Electron relaxation rate constant

μ_e ..... Electron mobility

D_{I^-} ..... Iodide diffusion constant

$D_{I_3^-}$ ..... Triiodide diffusion constant

C_{I^-} ..... Initial concentration of iodide (M)

$C_{I_3^-}$ ..... Initial concentration of triiodide (M)

m_e^* ..... Effective mass of electron

ϵ ..... Effective relative dielectric constant

d ..... Thickness of inner cell (μm)

L ..... Diffusion length

A ..... Cell area (cm^2)

p ..... Porosity of TiO_2 semiconductor

R_f ..... Roughness factor of TiO_2 semiconductor

T ..... Temperature (K)

k ..... Boltzmann constant, equal to 1.38066×10^{-23} JK^{-1}

Φ_0 ..... Incident photo flux ($cm^{-2}s^{-1}$)

μ ..... Electrical mobility

η ..... Quantum yield of photogenerated electron/photoelectric conversion efficiency

$E_{CB} - E^0_{Redox}$ ..... Difference of conduction band and standard electrolyte redox energy (eV)

1. INTRODUCTION

1.1. Background

Energy is an essential part of daily life, and demand for it is tremendous. At present, over 80% of the world's energy consumption comes from fossil fuels such as oil, natural gas, and coal, which are non-renewable resources. For instance, in the United States, the consumption of energy derived from fossil fuels was approximately 80 quadrillion British thermal units in 2015 [1]. It is predicted that the reserves of fossil fuels throughout the world could only last 40 years for oil, 60 years for natural gas, and 200 years for coal [2].

In contrast to fossil fuels, renewable energy is considered to be naturally replenished and poses minimal impact on the environment as it produces little or no net waste products such as carbon dioxide or other chemical pollutants. Various renewable resources are solar power, wind, hydropower, biomass, geothermal resources, as well as biofuels derived from crops and plants. North Dakota has abundant wind and biomass resources [3], and each of these renewable energy technologies has its advantages and limitations. For example, wind energy generation takes advantages of wind produced by uneven heating of the earth to generate electricity via a wind turbine; however, this technology is subject to high maintenance costs and opposition due to aesthetic and environmental reasons. Biomass energy relies on corn, switchgrass, and other materials as a replacement for conventional fossil fuels, yet a substantial amount of energy is required in biofuel production and the increasing use of biofuels might cause food shortage [4].

When comparing technologies for renewable energy, photovoltaic (PV) solar cells have grown the most in recent years. PV solar cells use semiconducting materials to convert abundant solar energy into direct current electricity. Multiple solar cells combine together to form a PV panel which can be installed on preexisting structures such as windows and rooftops, and are

relatively maintenance free. It is due to these advantages that the development of PV systems has gained momentum. It can be seen from Figure 1.1 that solar PV energy generation had a 30% annual growth rate in 2014, and 50% annual growth rate in the 5-year period between end-2009 through 2014, which was the fastest among all other renewable technologies [5]. In the same period, solar PV also experienced a significant expansion in the capacity installation. As shown in Figure 1.2, the solar PV global capacity dramatically increased from 23 GW in 2009 to 177 GW in 2014. The year 2014 witnessed a remarkable growth of 40 GW of capacity added towards a global total of about 177 GW. Notably, more than 60% of all PV capacity in operation worldwide at the end of 2014 was added over the last three years.

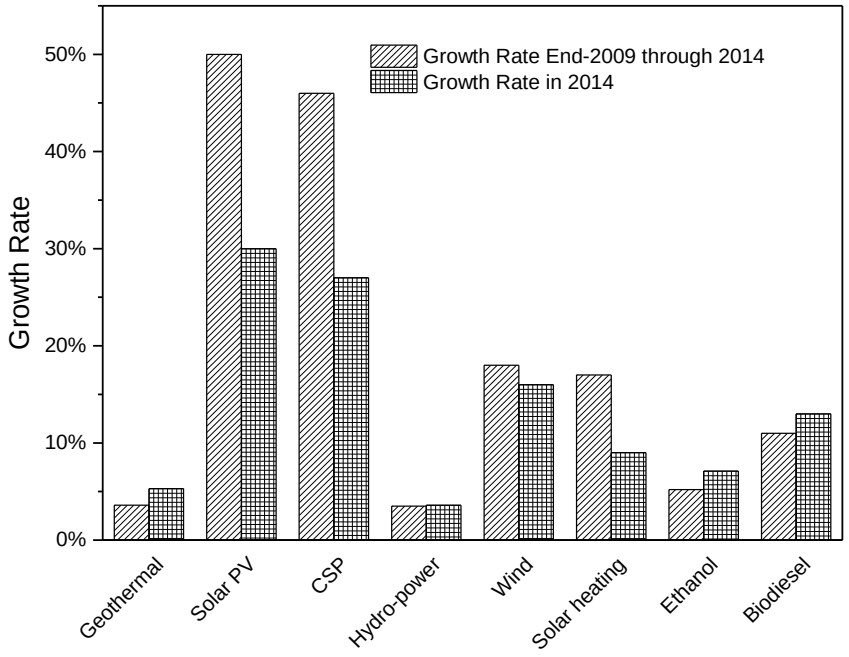

Figure 1.1. Average annual growth rates of renewable energy capacity and biofuel production, end-2009 to 2014. Solar PV capacity is based on 23.2 GW in operation at the end of 2009, 138 GW at the end of 2013, and 177 GW at the end of 2014. [5]

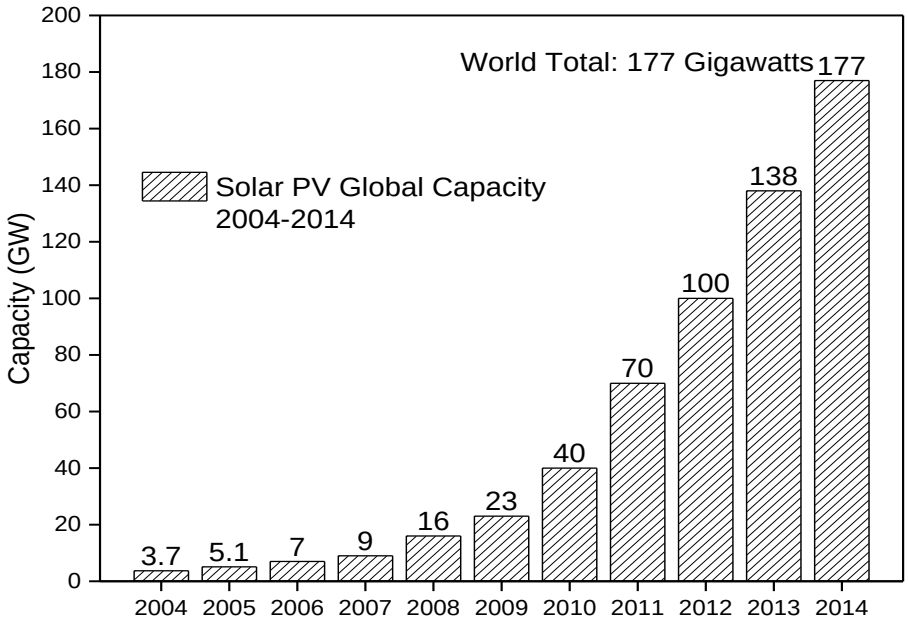

Figure 1.2. Solar PV global capacity, 2004-2014. [5]

Although the photovoltaic effect was discovered in 1839, the first practical PV solar cell had only been invented at Bell Labs a century later (1954). It utilizes a p-n junction to drive the separation of electrons and holes formed in the semiconductor upon light absorption. In order to prevent electron and hole recombination, high purity silicon (>99.99%) is used to maximize the device efficiency. Typical power conversion efficiencies in commercial modules are around 15%, and these devices generally last over 20 years under continuous use without loss of performance. At present, most of the commercially available PV solar cells are made up of crystalline silicon (> 80%) [6]. Although crystalline silicon (c-Si) has dominated the PV market, it has two major disadvantages: c-Si is a relatively poor light absorber requiring a thick active layer (200-500 μm) which increases the material cost, and it also requires expensive processing techniques such as high temperature and high vacuum, leading to an increase in manufacturing costs. Due to these two disadvantages, the electricity generated using solar PV has not been competitive with the conventional power plants. In 2009, the average price of electricity from solar modules was

~21 cents per kWh, whereas the electricity generated from a conventional coal source was only ~11 cents per kWh in the US energy market [7]. These high solar electricity prices have prevented widespread use of solar modules. For instance, in 2010, only ~0.03 % of the total electricity production was generated using solar power systems compared with ~70% from fossil fuels in the US [8].

Compared to large c-Si, polycrystalline films are less expensive to produce; however, grain boundaries of polycrystalline silicon reduce the efficiency of the solar cells. In order to maintain a high efficiency along with a significant reduction in the material and manufacturing costs, thin film technologies including CdTe/CdS, $Cu(In,G)Se_2$ (CIGS) and amorphous silicon are currently under development. Thin film technology has several advantages because it uses materials that absorb light much more than silicon. This quality allows the creation of thinner devices that use much less material, and can be fabricated via high throughput deposition schemes such as solution processing, chemical vapor deposition, and sputtering. Nevertheless, these solar cells have relatively low efficiencies (e.g. amorphous silicon), or require high-priced rare elements such as indium and tellurium.

In the last three decades, solar cells made from organic semiconductors have offered the potential to provide inexpensive solar power. Cost savings of organic photovoltaics (OPVs) are realized through the use of low-cost raw materials, simple manufacturing processes (especially solution-based deposition), and easy installation procedures due to the flexibility of thin film modules. However, a significant improvement in terms of both device efficiency and lifetime must be made towards practical applications. It is believed that to realize widespread adoption, OPVs have to meet minimum power conversion efficiencies of 10% and a minimum lifetime of 10 years. The current state-of-the-art laboratory efficiency of OPV multi-junction cell has reached 13.2%

[9], whereas outdoor lifetime has been estimated to be 1~2 years depending on how well the device terminals are sealed [10].

Similar to an organic solar cell, dye-sensitized solar cell (DSSC) is yet another type of cost-effective photovoltaic device because it could be fabricated through a simple process using inexpensive materials. Dye-sensitized solar cells are composed of titanium oxide (TiO_2) semiconductor which is commonly used as a paint base in the pigment industry, and the dye sensitizer which can be extracted from a variety of natural resources with minimum cost. In addition, carbonaceous materials could be used to replace the platinum catalyst at the counter electrode to further reduce the material costs. As such, DSSCs are easy to fabricate since they are insensitive to environmental contaminants and could be processed under ambient conditions. These unique features are favored in the roll-to-roll process which is a continuous, low-cost manufacturing method to print dye-sensitized solar cells on flexible substrates. Furthermore, DSSCs work better even under darker conditions such as in the dawn or dusk, as well as in cloudy weather. This exclusive capability to effectively utilize diffused light makes DSSCs an excellent choice for indoor applications like windows and sunroofs.

The advantages of dye-sensitized solar cells have intensified research interest, which is reflected by a tremendous number of research articles published in the past decade (Figure 1.3). It is noticed that the number of publications drastically declines after 2014 due to the paradigm shift toward perovskite solar cells, which emerged from the field of dye-sensitized solar cells. Though the seminal work on dye-sensitized solar cells (DSSCs) was initiated in 1991 by O'Regan and Grätzel [11], the research has advanced at a rapid pace in the 21st century. In particular, the development of new materials has considerably improved device efficiency from 7.1% in 1991 to 15% in 2016, which meets the requirement for commercial use [12-15].

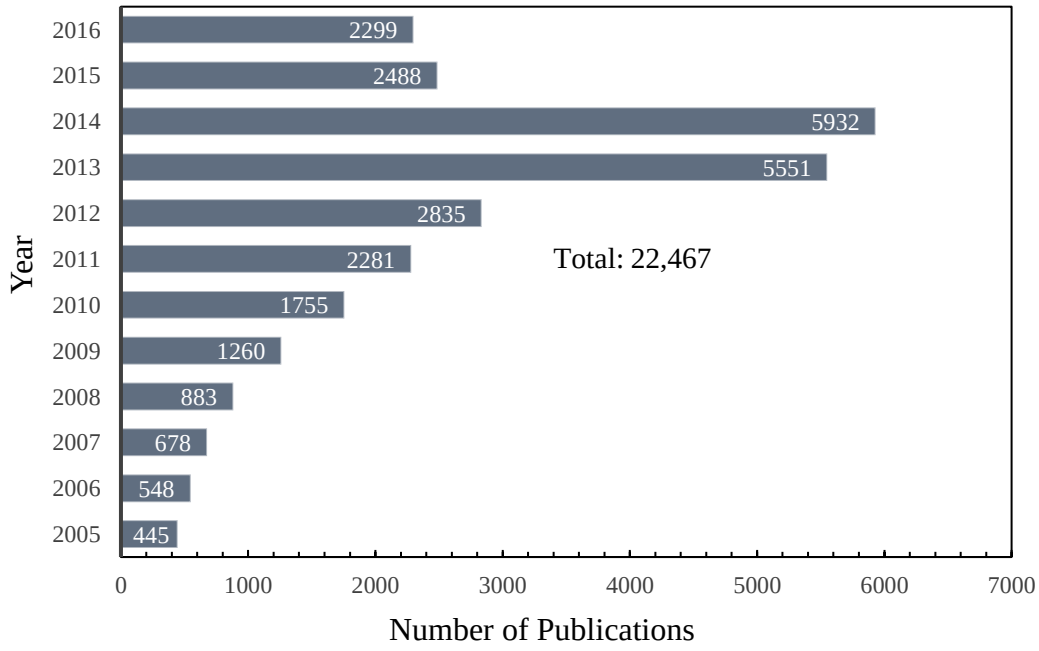

Figure 1.3. Number of publications published per year from literature search using the keywords "dye sensitized" and "solar" (data source ISI Web of Knowledge).

1.2. System Description

A dye-sensitized solar cell (DSSC) is a photoelectrochemical cell which uses specialized materials for specific cell functions such as photon absorption, charge separation, and charge transport. In this study, the schematic representation of a standard DSSC device is illustrated in Figure 1.4. The system is composed of four main components:

(i) a photoanode made up of a mesoporous oxide layer (typically, TiO_2) deposited on a transparent conductive oxide (TCO) glass substrate;

(ii) a monolayer of dye sensitizer covalently bonded to the surface of the TiO_2 layer to harvest light and generate photon-excited electrons;

(iii) an electrolyte containing redox couple (typically, I^-/I_3^-) in an organic solvent to collect electrons at the counter electrode and effecting dye-regeneration; and

(iv) a counter electrode made of a platinum coated conductive glass substrate.

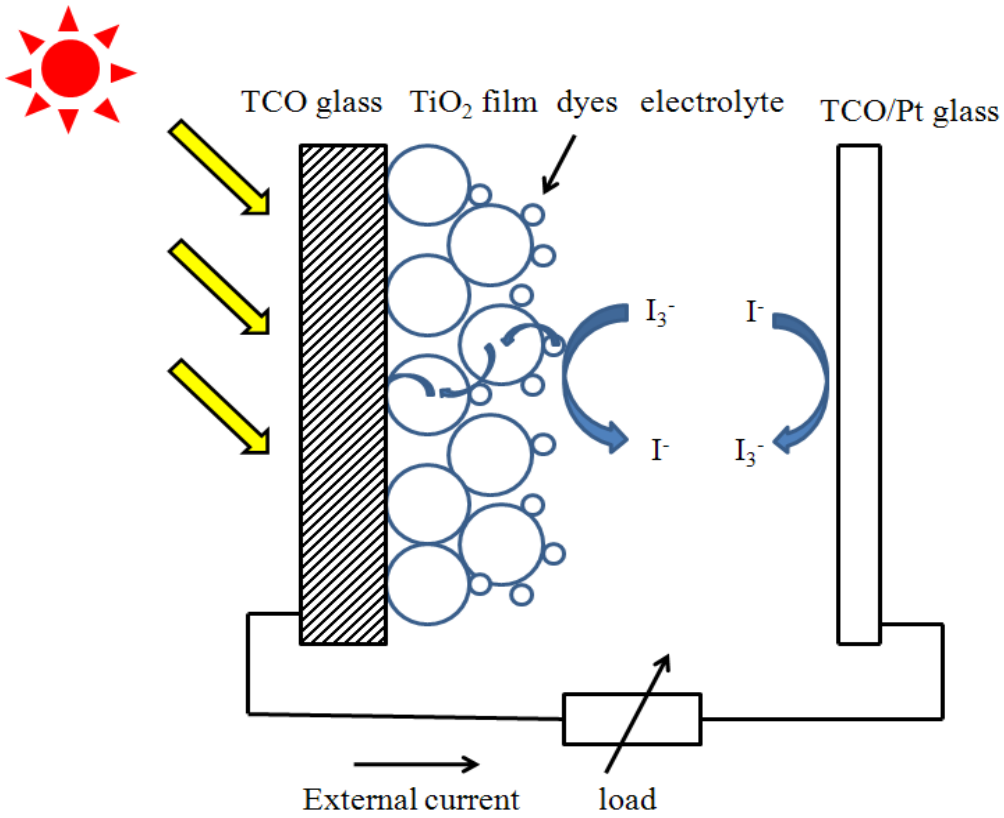

Figure 1.4. Schematic diagram of the dye-sensitized solar cell [16].

When sunlight strikes the solar cell, dye sensitizers on the surface of the TiO_2 film get excited and the electrons in turn get injected into the conduction band of TiO_2. Within the TiO_2 film, the injected electrons diffuse all the way through the mesoporous film to the anode and are utilized to do useful work at the external load. Finally, to complete the cycle, these electrons are collected by the electrolyte at the counter electrode and in turn are absorbed to regenerate the dye sensitizer. The overall performance of the DSSC can be evaluated based on the sunlight-to-electric power conversion efficiency (η),

$$\eta = \frac{V_{oc} J_{sc} FF}{P_{in}} \times 100\% \tag{1.1}$$

where V_{oc} is the open-circuit voltage (V), J_{sc} the short-circuit current density (mA/cm^2), FF the fill factor, and P_{in} the power of the incident light. The photovoltage (V_{oc}) is determined by the potential difference between the Fermi-level of electrons in the TiO_2 film and the redox potential of the electrolyte. Similarly, the photocurrent (J_{sc}) is determined based on the incident light harvest efficiency (LHE), charge injection, and collection efficiencies. The fill factor represents the ratio of the actual maximum obtainable power to the product of the open circuit voltage (V_{oc}) and short circuit current density (J_{sc}). In general, the overall conversion efficiency of dye-sensitized solar cells are tested under standard irradiation conditions (100 mW/cm^2, AM 1.5).

Under standard test conditions, the device efficiency can be maximized through optimizing each of the above-mentioned parameters (V_{oc}, J_{sc}, and FF). For instance, high open-circuit potential can be obtained by using Co(II/III) redox couple which has more positive redox potential and therefore increases the potential difference. Likewise, the short-circuit current can be enhanced by using panchromatic dye sensitizers which can absorb broad sunlight covering the visible to near-infrared range in solar spectrum. The fill factor is yet another important parameter that reflects the quality of solar cells. Increasing the shunt resistance and decreasing the series resistance as well as reducing the overvoltage for diffusion and electron transfer will lead to a higher FF value, thus resulting in greater efficiency and pushing the output power of the solar cell closer towards its theoretical maximum. In fact, the parameters (V_{oc}, J_{sc}, and FF) are highly dependent on material properties and physical processes within the device. Therefore, theoretical models that can capture the characteristics of physical process and materials properties are critical to optimize various operation parameters and cell configurations.

1.3. Outline of Dissertation

This dissertation is presented in seven chapters. In this chapter 1, a brief introduction and objectives of the study are presented. Chapter 2 provides detailed information on the DSSC operation and presents a literature review of theoretical and experimental studies on DSSCs. This review concentrates on the research trends of DSSC technology in terms of device modeling, state-of-art techniques, and novel device structures. It also discusses important results from the literature that provide a basis of knowledge for work presented in the subsequent chapters.

Chapter 3 and Chapter 4 describe the fabrication and characterization of two types of porous SnO_2 nanofibers and their composites as photoanodes for use in dye-sensitized solar cells. These two SnO_2 nanofibers were produced using the same electrospinning procedure under different carbonization temperatures. The microstructure of electrospun SnO_2 nanofibers is characterized by X-ray diffraction (XRD) and transmission electron microscopy (TEM). The morphological differences between SnO_2 nanofibers and SnO_2/TiO_2 composites are observed based on scanning electron micrographs (SEM). The photovoltaic performance of SnO_2 nanofiber based photoanodes is correlated to the light absorption and electron lifetime derived from transient techniques. These results have been published in *AIP Advances* [17] and *IEEE Transactions on Electron Devices* [18].

Chapter 5 describes the fabrication and characterization of activated graphene nanoplatelets (aGNP) as counter electrodes for use in dye-sensitized solar cells. The aGNP are prepared through the hydrothermal method using KOH solution as the activating agent. The morphology evolution from pristine GNP to aGNP is studied using XRD and SEM. Further, the effect of aGNP thickness on electrochemical activity is investigated using cyclic voltammetry (CV)

and electrochemical impedance spectroscopy (EIS). This work has been published in the *Journal of Applied Physics* [19].

Chapter 6 presents a simple, first-principles mathematical model which can predict the power output characteristics of dye-sensitized solar cells (DSSCs) under steady state operating conditions. The Butler-Volmer equation and Schottky barrier model are integrated into the developed model to include interfacial voltage losses at the counter electrode/electrolyte and TiO_2/TCO interfaces, respectively. Parametric simulations are conducted to analyze the effect of electrical resistance, interfacial voltage loss, and operating temperature on DSSC performance. The simulated results include the model validation, the outcomes, and the implications of parametric study, as well as a comparison to existing models. Details of the numerical approach applied to obtain these results are also discussed.

Finally, in chapter 7 the results and conclusions of the experimental and modeling work presented in this dissertation are summarized. Suggestions for further experimental investigations and modeling work are also presented. Appendix illustrates the procedure of a typical relaxation method.

2. LITERATURE REVIEW

The dye-sensitized solar cell is on the verge of commercialization and the manufacturing cost estimates for the technology are close to the projected costs of other PV technologies. To make DSSC technology more competitive, it is crucial to improve the device efficiency and stability, as well as to further reduce the material and manufacturing costs. To achieve these goals, models should be developed to quantitatively identify the promising semiconductors, dyes, and electrolytes, as well as their assembly. A well-developed model could be utilized to accelerate the development process with a substantial saving of experimental time and resources. Apart from rationale design and modeling, practical techniques are also very critical to maximize the light harvesting and minimize the electron losses. In addition, tandem and solid-state DSSCs represent two attractive device structures due to their high efficiency and excellent stability, respectively. In this chapter, advanced techniques and research trend of this promising technology from the perspective of device modeling, state-of-art techniques, and novel device structures are reviewed.

2.1. Device Modeling

Dye-sensitized solar cells comprise a variety of elementary components and multiple possible combinations. It is challenging to fine-tune each material and identify ideal conditions to optimize their overall performance in assembled devices. The development of models that could quantitatively identify the promising semiconductors, dyes, and electrolytes, as well as their assembly, could substantially save experimental time and resources. In addition, models also serve as a tool to gain detailed scientific insight into a range of phenomena occurring in the DSSC and extract information about the internal mechanisms.

2.1.1. Macroscopic diffusion model

Ferber's electrical model [20] integrates physical charge transport process with interfacial chemical reactions, and this developed framework has been adopted by many researchers [21-24] to compare the role of drift and diffusion in charge transport. It was identified that diffusion process dominates the charge transport in TiO_2 network and the capability of electron diffusion in the network can be quantified by the apparent diffusion coefficient.

The diffusion coefficient mainly depends on the TiO_2 structural parameters such as particle diameter, porosity, and neck size. For the given particle diameter, neck size has a significant influence on the porosity, and neck size can be accurately described by the overlap ratio. Ni et al. [25] developed two methods, namely, constant overlap and variable overlap, to determine the connectivity of dye-sensitized TiO_2 particles in high and low porosity levels, respectively. Given 10 nm particle size, these two methods quantitatively correlate the porosity with diffusion coefficient and light absorption coefficient, and derived an analytical equation of I-V output. Ogiya et al. [26] had developed a three-dimensional porous structure simulator, $POCO^2$, to examine the effect of overlap ratio, porosity, and particle size distribution on electron diffusivity. It was found that for a given porosity, TiO_2 particles with narrow size distribution and well-formed necks realized the optimal electron diffusivity. This simulator was later used to perform multiscale simulation [27], which included microscopic physical properties of the materials based on quantum chemistry calculation using a tight-binding quantum chemical molecular dynamics program [28]. The simulator was also utilized to investigate the Schottky barrier effect at photoelectrode, which is an improvement to the analytical method proposed by Ni and coworkers [29, 30].

Based on the Ferber's framework, many other physical processes such as transient response, and recombination can be also evaluated and correlated with the performance of DSSCs. Andrade

et al. [31] conducted phenomenological modeling of dye-sensitized solar cells under transient conditions. The developed model was used to compare experimental EIS results with the theoretical data, and obtain the relevant kinetic parameters with higher accuracy. Mitroi et al. [32] further simplified the physical model by assuming purely diffusive electron transport and linear recombination process. The simulated results were found to be still acceptable. Filipič et al. [33] analyzed a detailed recombination model which included both exponential distribution of trap states in TiO_2 and Gaussian distributions of energy levels in the electrolyte within the active layer. Shockley-Read-Hall statistics [34] were applied to determine trapping and detrapping rates in TiO_2 while Marcus-Gerischer theory [35] was used to determine electron transfer rate between the semiconductor and ions in the electrolyte. Simulations had shown that the optimal active layer thickness and efficiency of the cell increase for thinner electrolyte layers. Nithyanandam and Pitchumani [36] explored the possibility of DSSCs in real world application. The cell performance in different geographical regions was evaluated by using actual weather data, which could serve as guidelines for cell design as well as real-time active tracking and control.

In order to systematically analyze and model DSSCs, a reliable and consistent simulator is essential to facilitate an optimal design and fabrication process towards commercialization. Tanaka [37] developed a simulator for the dye-sensitized mesoporous TiO_2 solar cells applicable for both liquid and solid states. It was found that the detachment of the hole-conducting layer from the TiO_2 electrode coated with the dye sensitizer would remarkably reduce the magnitude of the external current. To study coupled charge transport in DSSCs, Fredin et al. [38] presented a simulation platform-SLICE to exclusively study the influence of ions in the electrolyte on electron transport in the nanoporous medium. The results showed that the effective permittivity coefficient, ε, had no influence on the electron transport when the ionic concentration was

sufficiently high. It should be noted even other simulations developed for silicon-based solar cells are capable of predicting the photoresponse of the semiconductor layer in DSSCs. For instance, Chitambar et al. [39] employed wxAMPs [40] program to interpret the photoresponses of sensitized p-GaP under the steady-state condition. However, this software has been mainly designed to describe and interpret only the semiconductor photovoltaic behavior.

Beyond aforementioned simulators built upon one-dimensional models, Ferber et al. [20] extended their previous model to two dimensions and discarded the effective medium approach; the electrical fields within the TiO_2 semiconductor and within the redox electrolyte are explicitly distinguished. It was found that the drift current was not negligible and the electric potential dropped mainly at the TCO/TiO_2 interface and not at a Helmholtz layer. Miettunen et al. [41] also developed a two-dimensional transient model to study the edge effect in DSSCs. The equations in 2D format were solved numerically using COMSOL Multiphysics modeling software. It was revealed that a typical small blank space (0.5 mm) on the photoelectrode side can significantly change the distribution of ions and the time to reach steady state. To further increase the accuracy of the modeling, a three-dimensional simulation on DSSCs has been recently developed by Gagliardi et al. [42, 43]. A computer-aided design software (TiberCAD) based on the finite element method has been used to simulate the DSSCs' performance in 1D, 2D, and 3D cell configurations. Gagliardi et al. [44] used a 3-D model of DSSCs to simulate the performance of an optical fiber wrapped DSSC. This work has provided a helpful guidance to the design of future cell structural aspects.

2.1.2. Trap-limited diffusion model

There are two trap-limited diffusion models. One is continuous-time random-walk (CTRW) model. In this model, charges hop from one trap to another, and the hopping rate depends on the

distance between them. The closer the traps are, the faster charges hop. Since the traps are distributed spatially, the distance to the nearest trap from one trap is distributed randomly. Thus, the transport of charges becomes dispersive. Based on CTRW model, Nelson [45] showed numerically that the recombination kinetics follows power law at long times.

The other model for transport of charges is multiple trapping (MT) model. From a physical point of view, electrons in TiO_2 nanoparticles undergo many trapping-detrapping events as illustrated in Figure 2.1; during charge transport process, the dye injected electrons can be captured by trap states or thermally emitted back to conduction [46, 47]. The trap states may originate due to the structural defects at the surfaces and the grain boundaries of TiO_2 particles, as well as in the interior of TiO_2 nanocrystallites [48]. The defects serve as an electron trap state which retards electron transport and also increases the traveling time prior to recombination [49]. In order to determine the spatial location of transport-limiting traps, Kopidakis et al. [50] derived the dependence of total trap density on the roughness factor. The best fit of the data confirmed that the density of electron traps in the film is directly proportional to the internal surface area, indicating that the traps are predominately located at the surface of TiO_2 particles compared to the bulk of the particles or interparticle grain boundaries.

The energetics of trapped electrons described by the density of states (DOS) influence a number of electronic phenomena. The exponential DOS distribution proposed by Nelson [45] is generally accepted as it is in accordance with the dynamics of transient photocurrent and photovoltage. Based on the assumption the surface is the main origin of traps and DOS obeys an exponential distribution, Lagemaat et al. [51] successfully interpreted the power-law dependence of the short-circuit current density on the electron concentration. Recent studies [48, 52] compared the role of shallow traps and deep ones in DOS distribution. Wang, et al. [48] differentiated the

shallow traps (>700 meV) from the deep ones (<350 meV) by the characteristic energy of 48 meV (K_BT_s) and 765 meV (K_BT_D), respectively. It was found that the K_BT_s energy of shallow trap states was comparable to the K_BT_0 energy of the overall electron trap states (46 meV), and that the amount of shallow traps was more than an order of magnitude larger than that of the deep ones.

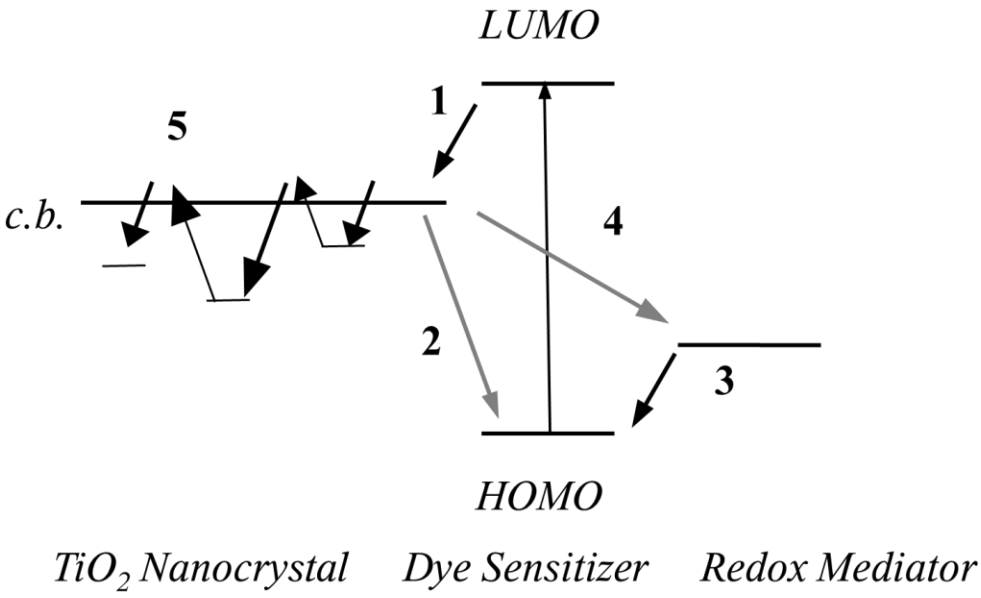

Figure 2.1. Illustration of electron transfer processes in a DSSC. Electrons get injected into conduction band (c.b.) of TiO_2 nanocrystal (1), and diffuse all the way through multiple traps to the TiO_2/TCO contact (5). A redox couple regenerates dye sensitizer (3). Two major electron loss pathways are with the dye cation (2) or with the redox couple (4).

Similarly, the spatial distribution of intragap trap states also plays an important role in charge transport and recombination process. In fact, the photoinjected electrons spend most of their time in traps. Hence in the presence of traps, electron transport was 10^3-10^5 times slower in nanoparticle films than in the single crystal [53]. Thus, the recombination of electrons occurs principally via trap states rather than via the conduction band, and the dynamics of electron recombination is dominated by shallow trap states in the bulk [52]. The slow recombination kinetics observed in high-efficiency DSSCs could be a result of multiple trapping with a broad energetic distribution of electron traps [54]. Unlike macroscopic diffusion model in which the

diffusion coefficient (D) is assumed to be a constant, the nature of the electron traps make D a function of the carrier density (n). Recently, Ansari-Rad et al. [55] found that D was independent of nanoparticle size for both surface and volume diffusion, and that increasing D with the particle size was a consequence of the trap-filling electronic effect and not a geometrical effect.

2.1.3. Equivalent circuit model

The mechanism of dye-sensitized solar cells can be understood through equivalent circuits, which are considered to be useful tools to analyze cell devices and improve cell performance. The information obtained from the equivalent circuit model of DSSCs includes electrical processes, system simulation, and cell modules.

A single diode model widely used for the analysis of silicon solar cells is also applicable to dye-sensitized solar cells. In DSSCs the diode-like behavior is originated from charge transport at the TiO_2/dye/electrolyte interface [56]. Figure 2.2 shows the equivalent circuit of the single diode model. The relation between external cell current and voltage can be expressed as

$$I = I_{ph} - I_0\left(e^{\frac{-q(V-IR_s)}{mk_BT}} - 1\right) + \frac{V - IR_s}{R_{sh}} \tag{2.1}$$

where I_{ph} is the photogenerated current density, I_0 the dark saturation current density, m the ideality factor, R_s the series resistance, R_{sh} the shunt resistance, k_B the Boltzmann's constant, q the elementary charge, and T the absolute temperature. The ideality factor m was quantitatively recognized as the inverse of the transfer factor β , and approaches to unity at high Fermi level [57]. Note the sign convention that $V < 0$ and $I > 0$ in the potential range of 0 to open-circuit voltage (V_{oc}).

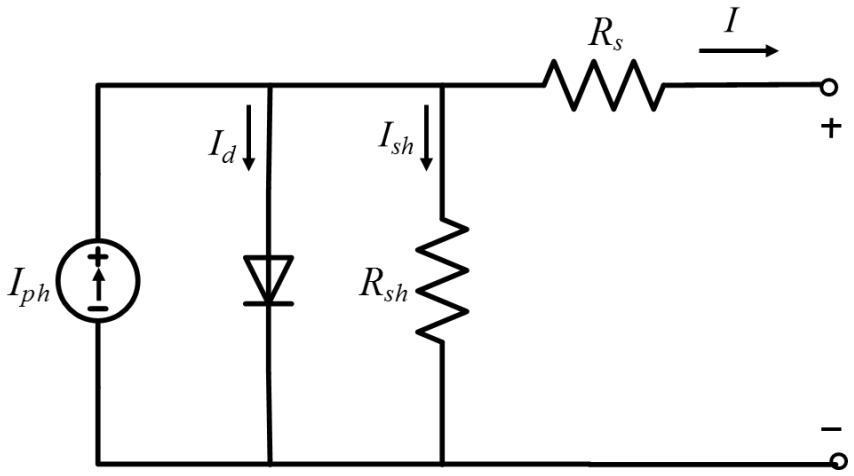

Figure 2.2. A schematic diagram of the single-diode equivalent circuit.

Though external cell current and voltage can be explicitly related by a set of five parameters expressed in Eq. (2.1), the same experiment measured I-V curve could often be well fitted with several different groups of parameter values. The difference between some parameter values in those groups is so large that it reaches up to several orders of magnitude. To eliminate the uncertainty, Tian et al. [58] developed an exclusive method to determine a group of parameter values for a specific DSSCs equivalent circuit. This method included the regular scanning voltage as well as a range of negative voltage (reverse stopping voltage). This linear extension of formal I-V ensures the unique values of DSSCs equivalent circuit parameters. Yet, another method was proposed by Wang et al. [59] to determine the parameter values pertaining to DSSCs. It is a two-step fitting procedure through which the entire five parameters of the single-diode equivalent circuit model could be predicted with high accuracy (root-mean-square errors less than 1%). In this two-step method, the five parameters were extracted by the graphic method as the preliminary values, and were further refined to the final accurate values through nonlinear least squares fitting. Further, Sarker et al. [60] developed an I-V curve based method to derive equivalent circuit parameters of DSSCs. Their method avoided iterative fitting procedure required by the two-step

method. In addition, it does not require combined analyses of EIS and I-V data, and thus is suitable for any routine analysis of DSSCs.

Equivalent circuit and its variants not only provide information of a single cell, but also serve as a powerful tool in analyzing of DSSC modules. Based on equivalent circuit, Huang et al. [61] investigated the role of FF in the design of large-scale DSSC module, and found that the high resistivity of transparent conducting oxides (TCO) and the high illumination intensity resulted in a lower optimal width. The intensity of illumination could impact the electrical characteristics of a DSSC module. This is a situation similar to partial shade which causes mismatch problem in a PV system. To analyze the partially shaded DSSC module, Giannuzzi et al. [62] modified the classical single diode model by adding a second diode to capture the behavior of the reverse-biased cells. The simulated results on a DSSC module made by four W-connected cells perfectly matched the experimentally measured I-V characteristics.

One of the major advantages of equivalent circuit model is that it avoids the cumbersome use of a number of physical and chemical parameters, but instead projects the PV system as a combination of minimal number of electrical circuit elements. The characteristic of each circuit elements implicitly reflect the physicochemical processes occurring in the cell. For example, a capacitance is used to reflect the existence of double-charged layer (Helmholtz layer) at the interface of porous semiconductor electrode and electrolyte of DSSCs. As in the case of classic single diode equivalent circuit, the capacitance could be omitted to reduce the mathematical complexity, since equivalent circuit model could precisely predict the cell operation under steady state condition. However, the capacitance in DSSC could play a role in transient analysis, such as real-time I-V measurement. Tian et al. [63] found that if the scan speed of measurement is too high, the measured energy conversion efficiency (η) of DSSCs will be much higher than that for

steady state conditions. However, for a scanning speeds lower than $2Vs^{-1}$, the measured I-V curve reflects the true DSSC's efficiency.

2.2. Routes to High Efficiency DSSCs

Similar to existing PV technologies, the development objectives of DSSCs mainly focus on lowering the levelized cost of energy (LCOE) which is dictated by the concept of critical triangle, namely, light-to-electric energy conversion efficiency, stability, and cost. Although no issue can be argued more important than another, the device efficiency has long been given special attention. Hence, it is critical to justify the competence of DSSCs with more mature silicon technologies in terms of the power conversion efficiency. To achieve this goal the strategy is to maximize the light harvesting and minimize the electron losses. The critical technologies are reviewed in this section.

2.2.1. Effective light harvesting

2.2.1.1. Co-sensitization

Dye-sensitizer plays a key role to ensure effective light harvesting in DSSCs: it is desirable to have a sensitizer that absorbs all incident light from the visible to the near-infrared region of solar spectrum up to the wavelength of approximately 920 nm. Since the invention of DSSCs, various ruthenium(II)-polypyridyl complexes such as N3, N719, N749, and black dyes have been synthesized and served as the paradigm of efficient charge-transfer sensitizers. However, there are several drawbacks of them: the high cost and the limited amount of noble metals, and also the sophisticated synthesis and purification steps. In general, metal-free organic dyes have proved to be promising candidates to replace Ru (II) based dyes, due to their intrinsic high molar absorptivity and broad absorption by co-sensitization approach.

Co-sensitization, combining two spectrum complementary dyes (i.e., blue and red absorbing sensitizers) into a DSSC, offers a cost-effective route to the panchromatic sensitization. Cid et al. [64] demonstrated high IPCE (80%) of primary dye sensitizer (TT1) at 690 nm, and used a secondary dye JK2 that complemented the absorption spectra by matching the optical window of phthalocyanine between 400-550 nm. The efficiency of co-sensitized device was 7.74% exceeding efficiencies as single-dye solar cells (3.52% for TT1, and 7.08% for JK2). Apart from two-dye sensitization approach, co-sensitization could involve plural organic dyes provided that each of them has different absorption wavelengths. Chen et al. [65] experimented triple-dye-sensitization using organic dyes: a merocyanine dye (Y), a hemicyanine dye (R), and a squarylium cyanine dye (B) named after their colors respectively. It was found all three dyes behaved better in triple-dye sensitization than in single-dye sensitization.

In addition to the complimentary spectrums, the criteria for dye co-sensitizer selection also include chemical compatibility between dye co-sensitizers, and a high molecular extinction coefficient: this is key for co-sensitization in allowing attachment of multiple dyes, while minimizing their mutual interactions [66, 67]. One strategy to enhance the dye compatibility and minimize the dye interactions is to utilize a spatial separated double layer architecture. For example, a primary monolayer of dye spatially separated from a secondary monolayer of another dye using a layer of Al_2O_3, resulted in a configuration of TiO_2/Dye-1/Al_2O_3/Dye-2 [68]. This architecture formed a molecular electron-transfer cascade at a dye/TiO_2 interface, and also achieved a vectorial movement of the oxidized dye species away from the TiO_2 surface [69]. Based on the similar design principle, Yella et al. [70] synthesized a donor-π bridge-acceptor zinc porphyrin dye (YD2-o-C8) and further co-sensitized with Y123 dye to enhance the performance of the device. The YD2-o-C8/Y123 co-sensitization lead to a strikingly high power conversion

efficiency of 12.3% under simulated air mass 1.5 global sunlight. The co-sensitized nanocrystalline TiO_2 film exhibited an impressive panchromatic photocurrent response over the whole visible range, achieving incident photon-to-electron conversion efficiencies of >90%.

Yet another co-sensitization method that eliminated Al_2O_3 separating layer was proposed by Lee and coworkers [71]. In their method, selectively positioning of organic dyes in a mesoporous TiO_2 film was first time realized by mimicking the working principle of column chromatography. A sequential adsorption of dyes was carried out to position three different dyes in one integrated film. Although the procedure was relatively complicated, the advantages are prominent; it facilitates the positioning organic dyes on the desired site in the mesoporous TiO_2 film while it prevents the interaction between each other. Latter, Miao et al. [72] developed a film-transfer technique which is a convenient way to fabricate the multilayered photoanode (TiO_2/dye-1/transferred TiO_2/dye-2). The fabricated photoanode achieved an excellent overall device efficiency of 11.5%.

2.2.1.2. Light scattering

Development of photosensitizers with improved spectral response at the low-energy end of the solar spectrum has not proven so successful because dye molecules with high red absorbance have lower excited-state excess free energy, thus lowering the quantum yield for charge injection. One way to increase the absorbance in the red is to increase the film thickness beyond 10 μm. However, this would result in an increased electron transport length and recombination rate; a marginal decrease in photocurrent will also be experienced [73]. An alternative approach to improve efficiency is to increase the path length of light by enhancing light scattering in the TiO_2 films.

To increase the light path length, Usami [74] proposed a structure that effectively confines incident light in the thinner cells by multiple scattering. The optimal backscattered intensity could be attained when the backscattering angle equalizes the critical angle of reflection at the surface. Later, Usami [75] examined the light scattering effect induced by submicron TiO_2 particles by applying Monte Carlo simulation. The optical confinement was found to have a much greater effect than the increase of photon absorption path length. As a matter of fact, almost entire incident light on the nanocrystalline films in the photoelectrochemical solar cells penetrates without effective scattering [46].

One way to enhance the light scattering is to incorporate larger particles as effective light scatterers. Based on Mie theory and computer simulation, a suitable mixture of small particles (20 nm diameter) and larger particles (250-300 nm diameter) could effect an increase in surface area and enhance effective light scattering, respectively. Simulated results showed that by using a mixture of particles a 33% increase in photon absorption is achievable for a 10 μm thick film [76]. To estimate the optical path length in TiO_2 electrodes, Chitba et al. [77] introduced a new concept of "haze". Haze, defined as the ratio of diffused transmittance to total optical transmittance, was controlled by the addition of submicron particles (400 nm diameter) to the TiO_2 electrodes. It was found that an increase in the haze of the TiO_2 significantly improved the incident photon to current efficiency (IPCE) of DSSCs in the near infrared wavelength region, and achieved a conversion efficiency of 11.1%.

Besides the inclusion of larger particles, coating a scattering-layer on the top of active layer is yet another way which could enhance the light scattering. The influence of scattering layers on efficiency of dye-sensitized solar cells was investigated by Hore et al. [78]. The additional light scattering layer consisting of TiO_2-rutile and ZrO_2 in a ratio of 1:3 improved cell efficiency from

3.8 to 6.8%. A hierarchically structured multi-layer TiO_2 architecture (shown in Figure 2.3) showed a remarkable improvement in the overall efficiency for dye-sensitized solar cells (DSSCs): a maximum of 11.43% at 1 Sun (12.16% at 1/8 Sun) versus 8.15% at 1 Sun (8.26% at 1/8 Sun) for the reference cell made of a nanocrystalline TiO_2 single-layer [79].

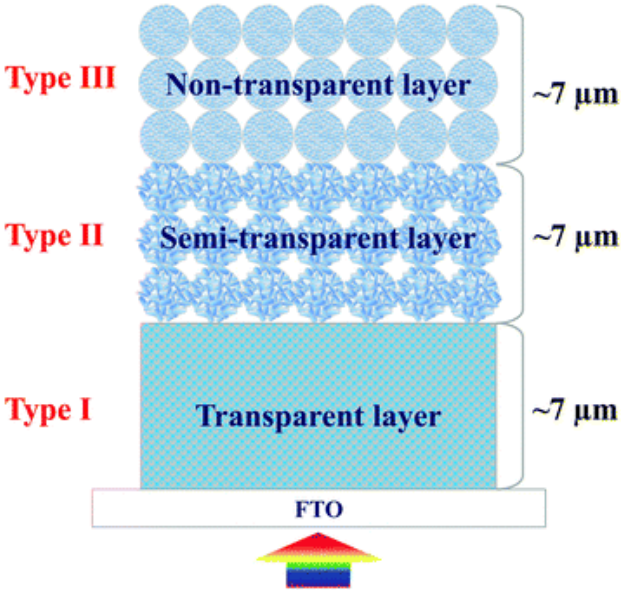

Figure 2.3. A hierarchically structured multi-layer TiO_2 architecture [79].

Recently, three-dimensional (3D) TiO_2 nanostructures such as network of nanofibers [80], nanotube arrays (TNAs) [81], submicron sized hollow spheres [82], and aggregates [83, 84] have been developed to enhance light scattering. These structures could further benefit the solar cells by providing other functions, for example, offering a large internal surface area for sufficient dye loading, or forming an internally connected core-shell structure to reduce the charge recombination in DSSCs [85]. The same strategy can be applied for ZnO or SnO_2 based dye-sensitized solar cells as well. Qian et al. [86] first synthesized TiO_2-coated multilayered SnO_2 hollow microspheres which exhibited a high photoconversion efficiency of 5.65%, a 34% improvement compared to the TiO_2-nano-SnO_2 film [16]. Another double-layered TiO_2-SnO_2 structure was developed by Lim

et al. [87]. Using a hydrothermal method, TiO_2 nanoflakes were grown on SnO_2 nanofibers to achieve a core-shell nanostructure, leading to a 4-fold efficiency improvement compared to pure SnO_2 nanofibers.

Similarly, a simple, versatile electrospinning technique can be used to produce SnO_2 nanofibers in various morphologies. Using this technique, Wali et al. [88] found the multiporous nanofibers excelled in high surface area (78 m^2/g) as well as diffusion length (~70-75 μm) compared to TiO_2 nanoparticles (~30 μm). By further increasing the tin concentration in electrospinning precursor, a large number of nuclei was formed during annealing such that all could not be accommodated in the fiber, leading to the formation of highly crystalline-cum-higher area SnO_2 nanoflowers [89]. In addition, Krishnamoorthy et al. [90] demonstrated a large-scale production of aligned SnO_2 nanofibers with a multi-nozzle electrospinning method combined with an air-shield enclosed rotating drum collector. This simple high-throughput electrospinning method could be extended to the mass production of core-shell nanofibers, hollow nanofibers, and side-by-side nanofibers.

2.2.1.3. Transparent electrodes

A DSSC can be operated using either frontside or backside illumination. In a frontside illumination arrangement, the light source is on the substrate side of the device, and for a backside illumination, the source is on the electrolyte side. A DSSC consisting of nanoparticulate film generally provides superior light-conversion efficiency for frontside illumination, which is due to the fact that the most efficient charge separation takes place close to the back contact. This phenomenon is confirmed by the experimental data obtained from intensity-modulated photocurrent spectroscopy (IMPS). It showed that electron transport in the front-illuminated cells comprises both trap-free and trap-limited diffusion modes, whereas electrons in the back-

illuminated cells travel only by trap-limited diffusion [49]. However, the TNAs-based DSSC must be operated under backside illumination as TiO_2 nanotube arrays (TNAs) are commonly grown on an opaque titanium foil.

For back-illuminated DSSCs, a counter electrode of high transparency is needed. Backside illumination is not optimal in DSSCs since the platinized counter electrode partially reflects light. The Pt-coated ITO glass exhibits an average light transmittance of 70% in the visible light region, while iodine in the electrolyte absorbs photons at lower wavelength (400-600 nm). Developing optically transparent counter electrode is not only imperative for light harvesting, but also beneficial for certain practical applications, like windows, roof panels, or various decorative installations.

Graphene and its composites are promising alternatives to Pt for high transparent counter electrode and good electrocatalytic activity. The semitransparent (>85%) film made by commercial graphene nanoplatelets exhibited high electrocatalytic activity towards I^-/I_3^- redox couple particularly in electrolyte based on ionic liquid (Z952). It was found that electrocatalytic properties of graphene nanoplatelets are proportional to the concentration of active sites (edge defects and oxidic groups), independent of the electrolyte medium [91]. Functionalized graphene sheets with oxygen-containing sites performed comparably to platinum [92]. Hong et al. [93] deposited composite films of graphene and polystyreneslufonate doped poly(3,4-ethylenedioxythiophene) (graphene/PEDOT-PSS) on indium tin oxide (ITO) substrates by spin coating at room temperature and applied as counter electrodes of dye-sensitized solar cells (DSSCs). A 60 nm thick composite film (contained 1 wt% graphene) coated ITO electrode exhibited high transmittance (>80%) at visible wavelengths and high electrocatalytic activity.

The suitability of other carbon materials used for counter electrodes has also been examined. Ultrapure carbon nanotubes directly transferred to a film could achieve a transparency over 90% at 550 nm wavelength [94]. The followed ozone treatment drastically increased the electrochemical activity and reduced the interfacial charge resistance. Graphite substrate with activated carbon was found to have good flexibility and high catalytic property [95]. This carbon electrode showed very low series resistance (R_S) and charge-transfer resistance (R_{CT}).

2.2.2. Surface engineering

2.2.2.1. Compact layer

The operation of dye-sensitized solar cells (DSSCs) involves a series of intriguing interfacial charge transfer processes. The interfacial energetics and kinetics are far more important in DSSCs than in conventional solar cells, owing to the huge internal surface area of the nanoporous TiO_2 anode with electrolyte permeation [96]. Two interfaces, namely, TiO_2 photoanode/electrolyte and FTO substrate/electrolyte have influences on the rate of electron recombination. At lower light intensities, under the maximum power point or open circuit condition, the latter is the dominant route for the electron recombination with tri-iodide in electrolyte [97, 98]. A common approach to suppress the electron recombination at FTO substrate-electrolyte interface is to use a thin TiO_2 compact layer to minimize the exposed FTO surface that is not covered by the nanoporous TiO_2 film.

A thin TiO_2 compact layer (ca. 100 nm) can be coated on the fluorine-doped tin oxide (FTO) glass by a dip-coating technique [99]. The layer effectively improved adherence of TiO_2 to FTO surface, provided a larger TiO_2/FTO contact area and reduced the electron recombination by blocking the direct contact between the redox electrolyte and the conductive FTO surface. Pulsed laser deposition is yet another method to deposit a Nb-doped TiO_2 (NTO) compact layer on a

commercial FTO substrate. The NTO layer with the anatase phase, having an electrical resistivity of 2.1×10^{-2} Ωcm and thickness of 80 nm, reduced the interfacial resistance by making an ohmic contact between FTO and TiO_2 NP film [100]. The positive shift in the onset of dark current, and a slow V_{oc} decay indicated a suppression in the transfer of back electrons.

The idea of using a compact layer to enhance the conductive contact between semiconductor and FTO substrate is also applicable for ZnO-based dye-sensitized solar cells (DSSCs). Guan et al. [101] introduced a ZnO compact layer prepared by a sol-gel method into photo electrode at the interface between fluorine-doped tin oxide (FTO) substrate and a mesoporous ZnO layer. It was found that the interfacial resistance of the ZnO (0.1 M)/FTO cell sample was considerably lower (6.77 Ω) compared to that of bare FTO substrate (11.57 Ω). Huang et al. [102] also observed synergistic effects between ZnO compact layer and $TiCl_4$ post-treatment on TiO_2 based DSSCs. The $TiCl_4$ post-treatment transformed ZnO compact layer to a bi-functional layer: it not only suppressed back electron transfer from FTO to electrolyte and reduced the FTO/TiO_2 interfacial resistance, but also dispersed abundant Zn element into TiO_2 coating to further facilitate electron transfer at TiO_2 layer.

At the TiO_2 photoanode/electrolyte interface, a conformal coating of insulating layers (such as SiO_2, Al_2O_3, and ZrO_2) on the TiO_2 films are shown to retard interfacial recombination dynamics. It is important to have conduction band edge of these metal oxides more negative compared to both the TiO_2 conduction band edge and dye excited state oxidation potential (ESOP). Therefore, the metal oxide overlayers could function as physical barrier layers for both electron injection and charge electron recombination reactions [103]. Recently, Elbohy et al. [104] reported that a vanadium pentoxide (V_2O_5) insulating layer in DSSCs leads to a significant increase in efficiency from 8.78% to 9.65%. Also, compared to bare TiO_2, an increased capacitance of

TiO_2/V_2O_5 was observed in cyclic voltammetry analysis. This increase in capacitance was interpreted as to indicate a positive shift of Fermi-level.

Although the role of insulating overlayer is critical in SnO_2 based DSSCs, only marginal performance improvement can be expected in mesoporous TiO_2 based device. SnO_2 is advantageous over TiO_2 for the high electron mobility, however, prone to the recombination of photoexcited electrons by the holes in the redox electrolyte due to the low-energy conduction band. One solution to overcome this shortcoming is to incorporate the insulating overlayer to form a core-shell structure: SnO_2 forms the core and a metal oxide semiconductor with higher CB such as TiO_2, MgO, and $CaCO_3$ forms the shell [105].

2.2.2.2. Hydrogenation and protonation

Recently, hydrogenation has emerged as a novel approach to effectively improve the TiO_2 photocatalytic and electronic properties. Black hydrogenated titanium dioxide nanocrystals were initially prepared by Chen et al. [106]. It was found that hydrogenation introduced the lattice disorder in the surface layers of nanophase TiO_2, accompanied by the creation of mid-gap electronic states, and reduced band gap. Latter, Su et al. [107] carried out investigation on hydrogenated titanium dioxide (H-TiO_2) nanocrystals in the application of dye-sensitized solar cells. H-TiO_2 was prepared via annealing TiO_2 in H_2/N_2 mixed gas flow at elevated temperatures ranging from 300 to 600 °C. Photoanodes with H-TiO_2 nanocrystals hydrogenated at 300 °C showed the highest improvement in J_{sc} (27%) and η (28%), in comparison to those with bare TiO_2. The enhancement was mainly attributed to high donor density, narrow band gap and positive of flat band energy of H-TiO_2 that promotes the driving force for electron injection.

Apart from hydrogenation, acid treatment is an alternative method to increase the performance of DSSCs. Acid treatment introduces proton (H+) to TiO_2 surface. This protonation

process changes the TiO_2 surface morphology, shifts the conduction band, and enhances the electronic coupling between dyes. The TiO_2 compact layer surface treated with H_2SO_4 acid was found to result in a rougher surface and more hydroxyl groups [108]. The rough surface increased surface area whereas hydroxyl groups led to the formation of Ti-O-Ti bonds which enhanced adherence of the compact layer with mesoporous TiO_2 film. Wang and Zhou [109] quantitatively studied the influence of HCl-treatment on the charge recombination and conduction band edge movement of TiO_2 film. It was found that the surface protonation of TiO_2 films caused a positive shift of the conduction band edge by 28 mV, and a slower charge recombination rate constant by a factor of 5 corresponding to an increase in V_{oc} by 50 mV. The collective effect 22 mV (50 mV-28 mV) agreed well with the experimentally observed V_{oc} enhancement (19 mV). In addition, HCl acid treatment of mesoporous TiO_2 also improves the electronic coupling between LUMO level of the dye and quasi-Fermi level of TiO_2 leading to higher interfacial charge generation [110]. These results indicated that surface protonation of TiO_2 could simultaneously improve V_{oc} due to the suppression of charge recombination and J_{sc} due to the positive shift of conduction band edge.

2.2.2.3. Plasma and post-treatment

Oxygen vacancies in TiO_2 result in surface defect states which slow down the electron transport in TiO_2 network due to the multiple trapping and detrapping process. Moreover, the oxygen vacancy states exist at about 0.75-1.18 eV below the conduction band edge of TiO_2, causing optical absorption by these surface states, which does not contribute to the photocurrent in a DSSC. Due to the fact that the oxygen vacancies in a TiO_2 film can be reduced by exposing it to an O_2 atmosphere, Kim et al. [111] first reported a low-temperature O_2 plasma treatment on TiO_2 film and the consequent improvement in the performance of DSSCs. XPS spectra revealed that the ratio of TiO_2 to (Ti_2O_3+TiO) increased from 1.30 for the untreated TiO_2 film to 1.62 for

the O_2 plasma-treated film. The study concluded that one of the main reasons for an increase in efficiency was due to a significant increase in dye absorption because of the reduction in the number of oxygen vacancies [112]. A similar effect was also observed in ultraviolet-ozone (UV/O_3) treatment. Along with the reduced number of oxygen vacancies, UV/O_3 treatment facilitates the removal of residual organics originated from the TiO_2 precursor pastes [113].

Apart from the oxygen-enriched atmosphere, the plasma treatment with other materials has been extensively investigated. Kim et al. [114] carried out hydrogen plasma treatment on nanostructured TiO_2 film by using a low-temperature RF plasma-enhanced chemical vapor deposition system, leading to an increased efficiency by 21%. This improvement can be ascribed to the increased hydrophilic property which generated an excess electrons and dye adsorption on TiO_2 surface. Other gases such as nitrogen, nitrogen/methane have also been investigated in plasma treatment. Wu et al. [115] compared oxygen, nitrogen, or nitrogen/methane (1:1) plasma on the TiO_2 photoelectrodes. Compared to the as-sintered sample, the nitrogen, oxygen and nitrogen/methane (1:1) plasma treated samples enhanced the cell efficiency by 5%, 19.7%, and 24.1%, respectively. The differences in the cell efficiency were attributed to the difference in the photoelectrode structures including oxygen vacancy and C-C sp^2 to sp^3 bonding ratio.

2.3. Novel Structured DSSC Devices

Development in the span of last two decades has led to a variety of novel DSSC devices originated from Grätzel cell prototype. The variants include P-type, tandem, hybrid, wire format, solid and quasi-solid state DSSCs. The dye can be replaced by a quantum dot to produce a quantum dot sensitized solar cell (QDSSC). Similarly, the liquid electrolyte can be gelated (quasi-solid-state DSSC) or replaced by a solid hole conductor (solid-state DSSC). Among these possible

options, tandem DSSC is particularly attractive due to its capability of attaining high power conversion efficiency.

2.3.1. P-type DSSCs

In contrast to n-type DSSCs, dye-sensitized photocathode (p-type DSSC), operates in an inverse mode where dye-excitation is followed by rapid electron transfer from p-type semiconductor (p-SC) to the dye sensitizer. Upon light absorption, the excited sensitizer injects a hole into valence band (VB) of semiconductor, leading to the reduction of the sensitizer. The injected holes diffuse through the back transparent conducting electrode (TCO) and then in turn pass through the external circuit and reach the counter electrode where they finally oxidize the redox mediator back to its original state. The operation principle of a typical p-type DSSC is depicted in Figure 2.4. The optical excitation of the absorbed dye is followed by (a) electron transfer from the excited dye to the oxidized species (I_3^-) in the electrolyte, and (b) electron transfer from valence band of p-type NiO to the HOMO level of dye.

In this technology, only few metal oxides exhibit p-type semiconductivity; hence, nanostructured nickel oxide is predominantly used as the p-SC material. He et al. [116] introduced tetrakis(4-carboxyphenyl)porphyrin (TPPC) and erythrosin B-coated porous p-type NiO films as working electrodes in DSSCs. The cathodic photocurrent was identified as hole injection from dye molecule to the valence band of the p-NiO electrode. The low IPCE values of TPPC (0.24%) and erythrosin B (3.44%) resulted in a poor overall conversion efficiencies of 0.0033% and 0.0076%, respectively. Such low IPEC can be attributed to the lack of efficient dye sensitizer for p-SC. To obtain an optimal dye sensitizer, new strategies have been employed to design the dye sensitizer and achieved high IPEC value up to 57% [117-119].

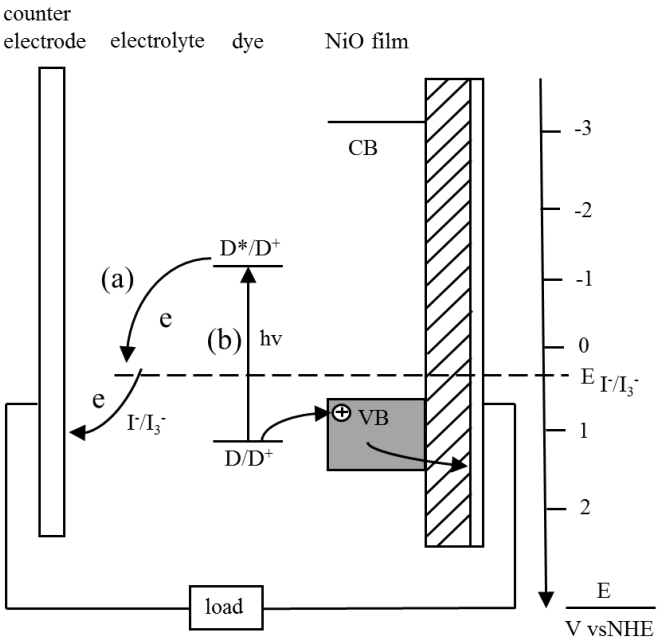

Figure 2.4. Schematic representation of the photoelectrochemical device based on p-SC.

Apart from dye sensitizer, intrinsic properties of p-type metal oxides also play an important role in dictating the p-DSSC performance. Uniform NiO films with a thickness less than 1μm could be prepared by doctor blading technique. However, compared to the n-type metal oxides, porous NiO has much lower electronic conductivity. Photoinduced absorption spectroscopy measurements indicated that the hole diffusion coefficient in NiO films is in the range of 10^{-8} to 10^{-7} cm^2s^{-1}, which is three orders of magnitude lower than electron diffusion coefficient in TiO_2 [120]. The slow diffusion of holes into NiO results in a long time delay between injection of holes and their collection, which increases the hole scavenging by the redox mediator [121]. In addition, the NiO films are prone to poor mechanical stability. Films thicker than 1 μm tend to crack and have poor optical quality [122]. One the other hand, although cracking issue is not a significant with thin NiO film, it inhibits sufficient dye loading which in turn limits the light absorption. As an optimal solution, a double-layered structure could be utilized to maximize the efficiencies of p-

DSSC. The double layered structure showed a significant increase in photocurrent of 64% IPCE (69% APEC) and 5.48 $mAcm^{-2}$ J_{sc}, respectively [123].

In theory, p-DSSCs should be capable to work as efficiently as n-DSSCs. However, the performance of p-DSSCs is far from ideal. The low photovoltage, photocurrent, and overall conversion efficiency result from close proximity of its redox potential (0.4 V vs NHE) to that of the NiO valence band (0.54 V vs NHE at pH 7), the thinness of NiO film, and fast recombination rates. Towards high efficiency p-DSSCs, it is imperative to replace NiO with other p-SCs with deeper valence band potentials and discover new redox mediators that have more negative redox potential. Table 2.1 summarizes the highest efficiency achieved based on available semiconductor materials.

Table 2.1. Summary of p-type DSSCs with their photovoltaic characteristics.

Process	Composition	Dye	Electrolyte	J_{SC} ($mAcm^{-2}$)	V_{OC} (V)	FF	η (%)	Ref
Thermolysis	NiO	Dye 3	0.6 M BMII/0.03 M I_2	6.36	0.208	0.34	0.46	[124]
Low-temperature hydrothermal	$AgCrO_2$	P1	0.5 M LiI/0.1 M I_2	0.1487	0.2463	0.41	0.0145	[125]
Hydrothermal	$CuCrO_2$	P1	0.3 M T_2/ 0.9 M T^-	1.43	0.309	0.38	0.17	[126]
Hydrothermal	$CuCrO_2$@Au	P1	0.3 M T_2/ 0.9 M T^-	2.68	0.305	0.38	0.31	[126]
Hydrothermal	$CuCr_{0.9}Mg_{0.1}O_2$	P1	0.3 M T_2/ 0.9 M T^-	1.51	0.201	0.449	0.132	[127]
Sol-gel	$CuAlO_2$	PMI-6T-TPA	0.6 M BMII/0.03 M I_2	~0.3	0.333	~0.39	0.041	[128]
Hydrothermal	$CuGaO_2$	P1	1.0 M LiI/0.1 M I_2	2.05	0.1993	0.45	0.182	[129]
Annealing	ITO	O18	LiI/I_2	5.96	0.1	-	-	[130]
Solvothermal	LaOCuS	PMI-NDI	Co^{2+}/Co^{3+}	0.039	0.150	0.26	0.002	[130]
Low-temperature hydrothermal	$NiCo_2O_4$	N719	0.1 M LiI/0.5 M BMII/ 0.03 M I_2	8.35	0.189	0.5	0.785	[131]

2.3.2. Tandem DSSCs

An apparent way to improve the DSSC efficiency would be to replace a single junction configuration by a multijunction tandem cell. The tandem DSSCs can enhance the full-spectrum light harvesting by stacking multiple dyes of complementary absorption characteristics. Hence, the theoretical limit of tandem DSSC efficiency could reach as high as 43% under standard test conditions, which is much higher than the 30% of conventional DSSCs with one photoactive dye-sensitized electrode [116]. In general, tandem DSSCs can be categorized into three groups: a stack of preassembled DSSC devices, a combination of dye-sensitized photocathodes with dye-sensitized photoanodes (pn-DSSCs), and a combination of complete dye-sensitized solar cells with other types of solar cells (hybrid).

The simplest tandem structure consists of a top DSSC stacked on a bottom DSSC. Two cells are either series or parallel-connected to form a tandem DSSC, namely, series-connected (ST-DSSC) or parallel-connected T-DSSCs (PT-DSSC). For ST-DSSCs, the short-circuit photocurrent density (J_{sc}) of the top and bottom cells should be same, whereas for PT-DSSCs the open-circuit voltage (V_{oc}) of the top and bottom cells should be identical. Each of these configurations has its unique advantages. Given the fact that shorter-wavelength photon carries higher energy than longer-wavelength photon, series connected cells could fully utilize this characteristic to achieve a higher open-circuit voltage (V_{oc}). In contrast, it is relatively easy for parallel connected cells to match V_{oc} values by adjusting top cell, which in turn maximize the short-circuit photocurrent density (J_{sc}).

Several studies have been carried out to investigate both ST/PT-DSSCs. Yamaguchi et al. [132] examined different combinations of dyes in series ST-DSSCs, and found best efficiency of 10.4% (J_{sc} = 10.8 mA/cm^2, V_{oc} = 1.45 V, and FF = 0.67) using N719 top cell and a black-dye

bottom cell. Latter, Kinoshita et al. [133] reported efficient DSSCs that exploit near-infrared, spin-forbidden singlet-to-triplet direct transitions in a phosphine-coordinated Ru(II) sensitizer, DX1. An ST-DSSC employing both DX1 and N719 could effect a power conversion efficiency over 12% under 35.5 mW/cm^2 simulated sunlight. Similarly, PT-DSSCs also have achieved an overall efficiency of about 10% comparable to ST-DSSCs performance. Dürr et al. [134] developed PT-DSSCs using red dye and black dye in the upper and lower cell, respectively. Such PT-DSSCs achieved an efficiency of 10.5%, with short circuit current densities of 21.2 mA/cm^2. It should be noted the PT-DSSCs also utilized a polyethylene oxide (PEO) based polymer gel to ensure good device stability. The PT-DSSCs were further optimized by Yanagida and coworkers [135]. It was found that top cell thickness (d_T) could be easily adjusted to match V_{oc} values for the top and bottom cells. This reflected in higher conversion efficiencies compared to ST-DSSCs.

In general, ST/PT-DSSCs can be easily fabricated and optimized because top and bottom cells are two separate devices. However, the drawback is also evident that stacked tandem structure requires a strict adjustment of the transmittance of the top cells. Specifically, the transmittance of electrolyte, platinized counter electrode, and TCO glass need to be maximized to allow effective light transmission. One way to maximize the light transmission is to utilize a pn-DSSC which could omit the Pt counter electrode at top cell and TCO glass at the bottom cell.

A tandem pn-DSSC combines p-type photocathode and n-type photoanode in series. The energy diagram of photocathode is schematically illustrated in the right part of Figure 2.5, and the photoanode is on the left side. The energy diagram shows that the open-circuit voltage (V_{oc}) depends on the potential difference between the valence band edge of the p-type semiconductor and the conduction band edge of the n-type semiconductor. Similarly, the photocurrent is dictated by the weakest photoelectrode. The principle of such all-through tandem cell was for the first time

experimentally demonstrated by He and coworkers [136]. In their study, a pn-DSSC was fabricated using N3 dye coated TiO_2 film and erythrosin B-coated NiO film. The fabricated cell had a larger V_{oc} (732 mV) but very limited photocurrent (J_{sc} = 2.26 mA/cm^2), resulting in low efficiency of 0.39%. The limited photocurrent can be attributed to the poor photocurrent matching and low IPCE of photocathode. To address this issue, Nattestad et al. [137] synthesized three donor-acceptor dyes for NiO photocathode. These dyes encompassed a variable-length oligothiophene bridge, which provides control over the spatial separation of the photogenerated charge carriers. Unlike conventional dyes used in TiO_2 photoanode, these newly designed dyes have anchoring groups attached to the donor component. Utilizing these dyes, a pn-DSSC was fabricated and optimized for illumination through TiO_2 photoanode (0.8 um). The obtained overall efficiency (1.91%) for the first time exceeded the value obtained by n-DSSC (1.79%).

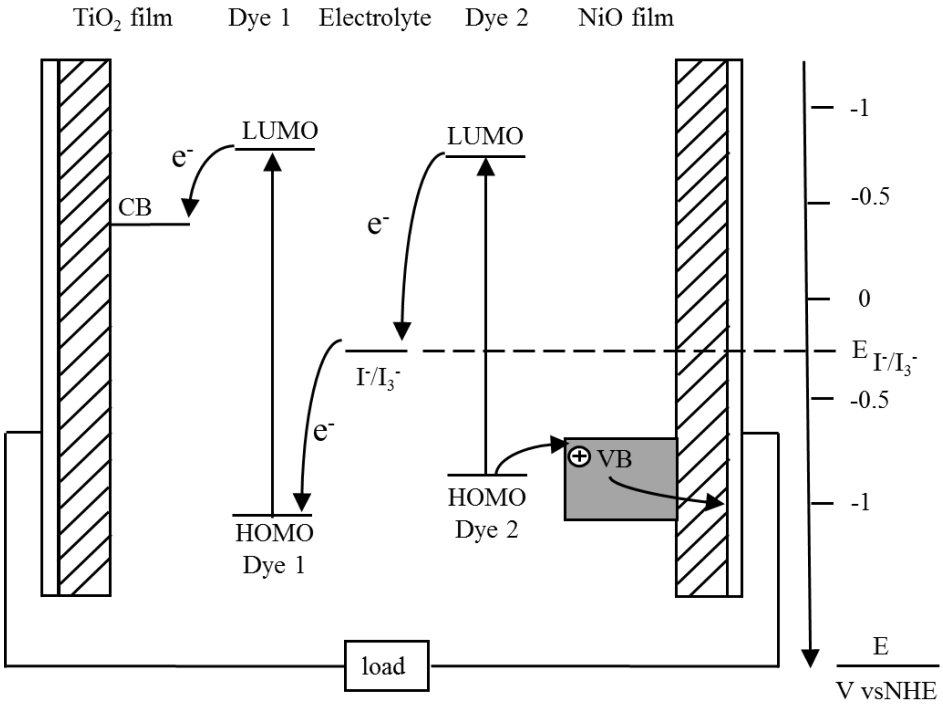

Figure 2.5. Schematic representation of tandem pn-DSSCs.

To date, the device efficiencies of pn-DSSCs are considerably lower compared to those high efficiency n-DSSCs. The bottleneck of further advancement lies in developing high efficiency photocathode. A systematic work is required to optimize all key components in p-DSSCs, including conscientious selection of p-type semiconductors, and synthesizing suitable dyes as well as electrolytes for p-semiconductors. Given the fact that the research on p-DSSC is of a late start and insufficiently studied in the past decade, the rudimentary results appear to be still very promising. In addition, the concept of pn-DSSCs can be considered as an extension to existing n-DSSC technology by replacing Pt-counter electrode with photocathode. Great potential along with marginal addition of process and material cost will make such pn-DSSCs an economically attractive option among all other tandem technologies.

Apart from tandem pn-DSSC, inexpensive dye-sensitized solar cells could also be printed on a variety of more traditional inorganic solar cells to achieve power conversion efficiency above 20%. Such hybrid tandem photovoltaic (HTPV) device will be exceptionally ideal, if band gaps in thin-film tandem solar cells are ~1.7 eV for a top cell and ~1.1 eV for a bottom cell. Coincidentally, this combination is well matched to the 'HOMO-LUMO' energy gap of the N719 dye in DSSC and the band gap energy of the $Cu(In_xGa_{1-x})Se_2$ absorber in CIGS solar cell. Liska el al. [138] first attempted the photovoltaic tandem cell comprising a nanocrystalline DSSC as a top cell for high-energy photons and a copper indium gallium selenide thin-film bottom cell for low energy photons. This DSSC/CIGS tandem cell shows a promising power conversion efficiency greater than 15%. Although the IPCE of DSSC and CIGS were compared, the IPCE of DSSC/CIGS tandem cell was not reported because of the difficulty in evaluation of IPCE. The difficulty results from the fact that the response time and absorption wavelength range of DSSC are different from those of CIGS. To overcome this issue, Jeong et al. [139] simulated and

identified a specific condition to evaluate external quantum efficiency of tandem cells under AC modes. It was found that at given chopping frequency (10 Hz) and bias light (1 Sun) the experimentally measured IPCE was consistent with the simulated results.

One of the key factors that limit the efficiency of DSSC/CIGS tandem solar cells is the transmittance of DSSC top cell. Wang et al. [140] estimated the efficiency loss using equivalent circuit analysis and pointed out that TCO substrates have a strong absorption in near infrared region. One way to overcome the optic loss at TCO substrates is to employ arc-plasma deposition (APD) technique for Pt interfacial layer, which maximizes the transmittance and minimizes the damage to the layers of CIGS bottom cell. Based on this technique, Moon et al. [141] fabricated a DSSC/CIGS tandem solar cell with higher efficiency (13%) than the corresponding single-junction devices of DSSCs (~7.25%) and CIGS (~6.2%). Similar to CIGS, GaAs can serve as an alternative and be used as a bottom cell. Ito el al. [142] developed a stacked tandem solar cell by mechanically stacking DSSC on a GaAs/$Al_XGa_{(1-X)}As$ graded solar cell (GGC). The resulting high open-circuit voltage (1.85 V) make it very promising for the application of water splitting.

2.4. Objectives of the Present Study

The primary objective of this study is to investigate innovative electrode materials for use as photoanode and counter electrode in DSSCs. The newly designed electrode materials are anticipated to be highly efficient with a low cost, and have potential to be scaled up for the mass production of DSSC devices. To achieve these goals, it is critical to develop a mathematical model that links the material properties to device performance. This model can be used to predict the power output characteristics of newly designed DSSCs using innovative materials as electrodes.

From the literature, several observations have been made: (a) one-dimensional nanostructured tin dioxide (SnO_2) is a promising photoanode material; (b) graphene nanoplatelets (GNP) have outperformed platinum as the electrocatalyst for Co(II)/(III) mediated DSSCs; (c) use of SnO_2 photoanode and GNP counter electrode may increase device efficiency of DSSCs as well as reduce the material costs; (d) material design and device modeling are critical to maximize the light harvesting and minimize the electron losses.

In light of these observations, this study investigates the fabrication and characteristics of two innovative electrode materials (SnO_2 and activated GNP) for use as photoanode and counter electrode in DSSCs. The objectives of this study are: (i) to explore SnO_2 nanofibers and their TiO_2 nanoparticle composites as photoanodes; (ii) to analyze the microstructure, transient response, and recombination dynamics of SnO_2/TiO_2 composite-based DSSCs; (iii) to replace thermally deposited platinum catalyst with activated graphene nanoplatelets (aGNP) as counter electrodes; (iv) to conduct an in depth analysis on the factors (e.g. morphology, porosity, and surface area) that influence the electrocatalytic properties of aGNP; (v) to develop a mathematical model to understand physical mechanisms of these newly designed DSSCs; (vi) to simulate the performance of the DSSCs and investigate important design and operating parameters.

3. CHARACTERISTICS OF TIN OXIDE NANOFIBER AND TITANIUM DIOXIDE NANOPARTICLE COMPOSITE FOR DYE-SENSITIZED SOLAR CELLS

3.1. Introduction

One-dimensional (1D) SnO_2 nanofibers carry high electron mobility (100-200 $cm^2V^{-1}S^{-1}$) and ultraviolet stability due to their large band gap (3.6 eV). However, the application of SnO_2-based DSSCs has been limited due to poor photovoltaic performance caused by fast interfacial electron recombination and insufficient attachment of dye molecules. For DSSCs incorporating "bare" SnO_2 with no surface treatment, dye cation regeneration by the iodide/iodine redox couple is often not sufficiently fast, and thus, it does not compete with recombination of conduction band electrons with the dye cation [143]. In view of this concern, in this chapter, a recently reported innovative rational synthesis route [144] was adopted for fabrication of continuous SnO_2 nanofibers and their composites [145] for use as flexible, porous electrode materials of dye-sensitized solar cells. This rational synthesis consisted of electrospinning the polyvinyl pyrrolidone/stannic chloride pentahydrate ($PVP/SnCl_4{\cdot}5H_2O$) precursor polymer nanofibers, followed by controlled carbonization. Prototype dye-sensitized solar cells were fabricated with the fibrous SnO_2 films as photoanode, thermally deposited platinum as counter electrode, and a thin layer of I^-/I_3^- solution as electrolyte. The transient response of SnO_2-based DSSCs was characterized using transient photocurrent (TPC) and transient photovoltage (TPV). Experimental results showed that electron recombination time of SnO_2/TiO_2 composite is comparable to SnO_2 nanofiber (21.8 ms), and incorporating TiO_2 nanoparticles in SnO_2 nanofibers reduces the decay time constant τ from 0.2 ms to 0.15 ms, indicating an improvement in charge transport and

collection. SEM and TEM were used to characterize the morphology and structure of the porous SnO_2/TiO_2 composite electrodes. The excellent connectivity of the synthesized SnO_2 nanofibers effects the fast charge transport in photoanode of DSSCs; the compact morphology of SnO_2/TiO_2 composites are responsible for the increased dye uploading, which is quantified using UV-Vis spectroscopy.

3.2. Experimental Methods

3.2.1. Preparation of SnO_2 nanofibers

The SnO_2 nanofibers were prepared by electrospinning and calcination from polyvinyl pyrrolidone/stannic chloride pentahydrate ($PVP/SnCl_4 \cdot 5H_2O$) precursors. Specifically, the electrospinning solution was prepared by adding $SnCl_4 \cdot 5H_2O$ into 10 wt% PVP in an ethanol/ dimethylformamide (DMF) mixed solvent (weight ratio 1:1). The weight ratio of $SnCl_4 \cdot 5H_2O$ to polymer intermediate (PVP) was fixed at 1:1. The solution was stirred by a magnetic bar at room temperature. Subsequently, electrospinning was carried out with this solution. The $PVP/SnCl_4 \cdot 5H_2O$ precursor was ejected from a stainless steel needle under a high voltage of 17 kV to form nonwoven fibrous mats on the collector. The flow rate was kept at 1.0 ml/h, and the needle-to-collector distance was fixed at 21 cm. The electrospun nanofiber mats were calcinated at 500 °C for 4 h with a heating rate of 0.5 °C/min. [144]

3.2.2. Microstructure characterization

The structural analysis of electrospun SnO_2 nanofibers was performed on a D8 Advance X-ray diffractometer (XRD, Bruker AXS, Germany) over the Bragg angles 2θ range from 10° to 80°. The schematic for the X-ray diffractometer is shown in Figure 3.1. The Cu-Kα radiation (λ = 1.5406 Å) was generated in the X-ray generator and had a scanning speed of 4° min^{-1}. The

X-rays were diffracted by the lattice planes of the sample and detected by a solid-state detector (SSD). The morphology of SnO_2 nanofibers was studied by using Hitachi S4800 field-emission scanning electron microscopy (SEM) and JEOL JEM-2100 transmission electron microscopy (TEM) with selected-area electron diffraction (SAED) at an accelerating voltage of 120 kV. For TEM measurements, precursor nanofibers were directly deposited on the copper grids during electrospinning, and SnO_2 nanofibers were dispersed in ethanol by ultrasound and then transferred onto copper grids.

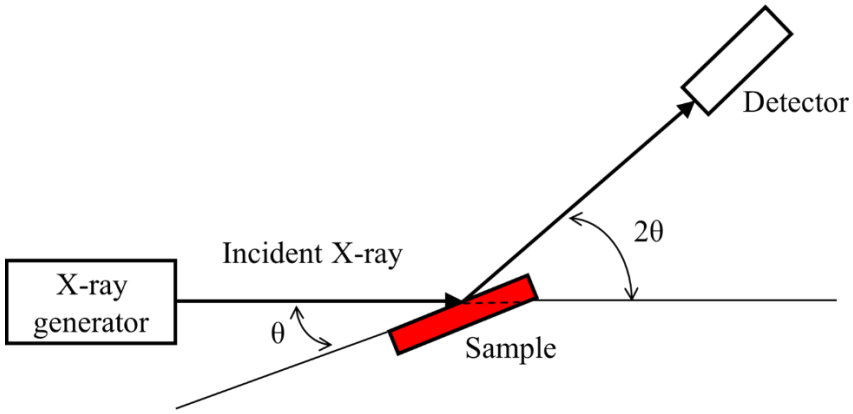

Figure 3.1. Schematic of X-ray diffractometer.

3.2.3. Fabrication of SnO_2/TiO_2 composite based DSSCs

The SnO_2 nanofibers were synthesized using above described procedures. The TiO_2 was purchased from Evonik Degussa known as "Aeroxide P25" nanopowder which has a composition of ~70% anatase and ~30% rutile. The TiO_2 phase transition from anatase to rutile occurs upon significant thermal activation between 700 - 1000 °C depending on the crystal size and the impurity content. To prepare SnO_2/TiO_2 composite based photoanodes, SnO_2 nanofibers and TiO_2 nanoparticles (P25, Degussa) were mixed at an optimized weight ratio (1:1) with ethyl cellulose, α -terpineol, and ethanol to form a paste through successive ultrasonication and stirring. Specifically, 125 mg SnO_2 and 125 mg TiO_2 were added to 4.9 ml ethanol and left for dispersion.

The solution was stirred by alternating between sonication and mechanically stirring at 1-hour intervals for a total of 4 hours. Subsequently, 125 mg ethyl cellulose as binder and 0.89 ml α-terpineol as solvent were added to the mixture, which was repeatedly first ultrasonicated and then stirred until all grains disappeared and the solution became homogeneous. The solution was heated in a vacuum oven at 80 °C to remove excess ethanol until it turned into a form of homogeneous slurry ready for doctor-blading.

All devices were fabricated using the same procedure adapted from [146]. A thin layer of the slurry was doctor-bladed onto fluorine doped tin oxide (FTO) glass substrate with an active area of 0.16 cm^2. An optimal thickness (8-9 μm) was confirmed by a Dektak profilometer [145]. This sample was annealed at 500 °C for 30 min to form a mesoporous film. On the top of the film, a scattering layer (Solaronix Ti-Nanoxide R/SP) was coated that enhanced light absorption of the mesoporous active layer. Then the sample was dipped in 40 mM $TiCl_4$ solution at 80 °C for 30 min, followed by sintering at 500 °C to form a TiO_2 blocking layer. Such layer passivates the 3D interpenetrated nanofiber/nanoparticle network and therefore can effectively improve the electron transport while prevent charge recombination. In this study, a thin blocking layer was coated on all the samples using the same methods in order to exclude its effects on the performance enhancement for different samples. The thickness of this blocking layer was typically tens of nm with roughness factors in the range of 2-3 [147].

The resulting photoanodes were immersed in dye solution containing 0.5 mM Ruthenizer 535-bisTBA dye (Dyesol N-719) in acetonitrile/t-butanol (volume ratio: 1:1) for 24 hours. In the final step, any excess dye molecules on the photoanode were rinsed in acetonitrile for several hours. Counter electrode was prepared by spin coating 40 nm Pt onto FTO glass substrates. Finally, the

photoanode and counter electrode were sandwiched and sealed with 60 µm thick plastic and injected with I^-/I_3^- electrolyte through reversed channels.

3.2.4. Dye desorption from photoanodes

NaOH solution (10 mM) in ethanol and DI water (volume ratio 1:1) was used to desorb dyes from SnO_2 nanofiber and SnO_2/TiO_2 composite. Each of the dye attached photoanodes was dipped in the 10 mM NaOH solution for 24 h at room temperature to desorb dye molecules. The dye molecules were peeled off from the photoanode into solution by neutralization reaction between acidic carboxylic group and basic solution [16]. The volume of each solution was kept as 2 mL for dye desorption. The UV-Vis absorption spectra of the dye solution were determined using an Agilent 8453 spectrophotometer. The schematic of the spectrophotometer is shown in Figure 3.2. This instrument has a deuterium-discharge lamp for the ultraviolet (UV) wavelength range and a tungsten lamp for the visible and short wave near-infrared (SWNIR) wavelength range. The lens was used to receive and collimate the light from the lamp. A narrow band of wavelengths of collimated light was separated and transmitted by the monochromator and then measured using detector and then amplified. The UV-Vis absorption spectra were displayed on a PC display using ChemStation software.

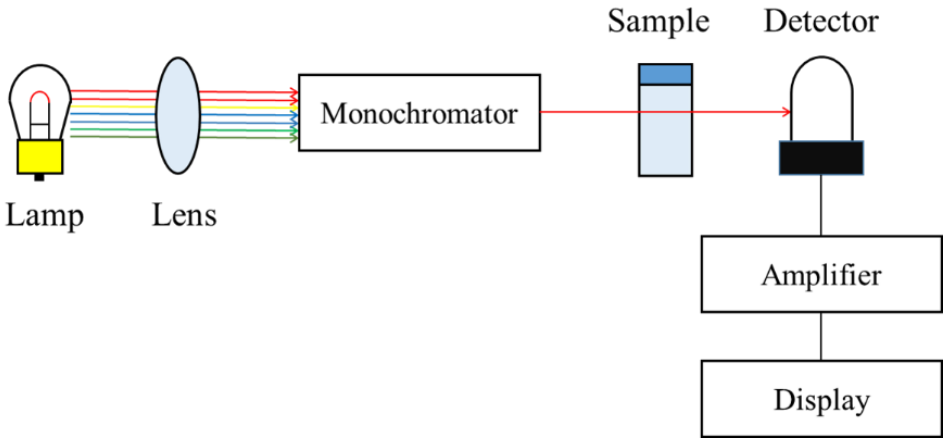

Figure 3.2. Schematic of UV-Vis spectrophotometer.

3.2.5. Current density and voltage characteristics

Current density and voltage (J-V) characteristics of the DSSCs were measured under simulated AM 1.5 sunlight at a light intensity of 100 mW/cm^2. Figure 3.3 shows the schematic of the J-V measurement system. A 300 Watt Xenon lamp (Newport 67005) equipped with KG-5 filter was used as light source to simulate the standard AM 1.5 sunlight. The light intensity was calibrated using a National Renewable Energy Laboratory (NREL) certificated Si reference cell and the spectral mismatch factor was estimated to be less than 1% [148]. Both the reference and test cells were ensured to be placed at the same spot under the solar simulator during measurement. The J-V characteristics of the DSSCs were measured using an Agilent 4155C semiconductor parameter analyzer to record the generated photocurrent upon the application of an external potential bias. The voltage was swept in the direction of short-circuit to open circuit. The J-V data were plotted to extract different photovoltaic parameters, including short-circuit current (J_{sc}), open-circuit voltage (V_{oc}), fill factor (FF), and power conversion efficiency (η).

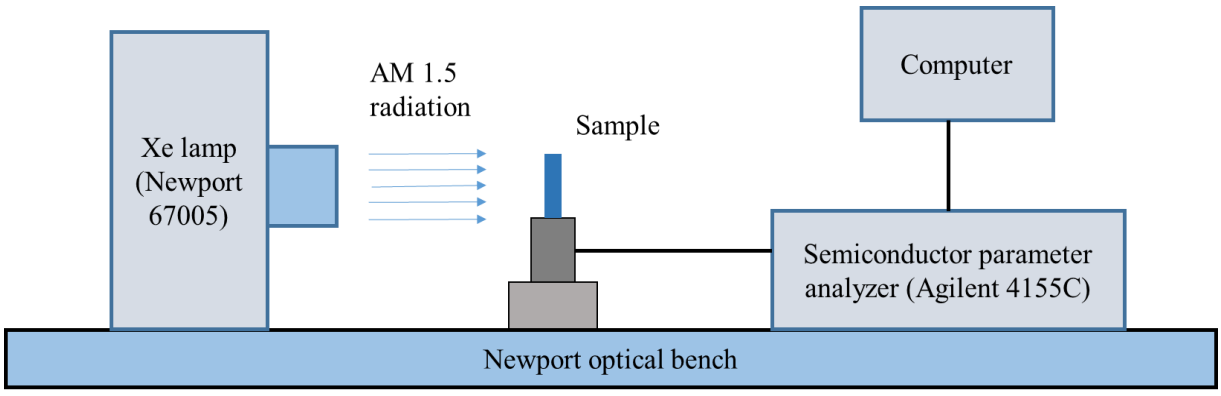

Figure 3.3. Schematic of a current density-voltage measurement system.

3.2.6. Electrochemical impedance spectroscopy

Electrochemical impedance spectroscopy (EIS) measurement was carried out using a computer-controlled Ametek VERSASTAT 3-200 potentiostat incorporated with a frequency

analysis module. A schematic diagram of the EIS experimental setup is shown in Figure 3.4. During the measurement, a reference electrode and a counter electrode probe from the VERSASTAT were connected to the photoanode, and the sensor and working electrode probes were connected to the counter electrode. The AC signal of amplitude 10 mV in the frequency range from 0.1 to 10^5 Hz at a certain DC bias voltage (open-circuit voltage) was used to test the DSSC sample in a dark environment. The Nyquist plot was displayed on the computer and further analyzed using EIS spectrum analyzer.

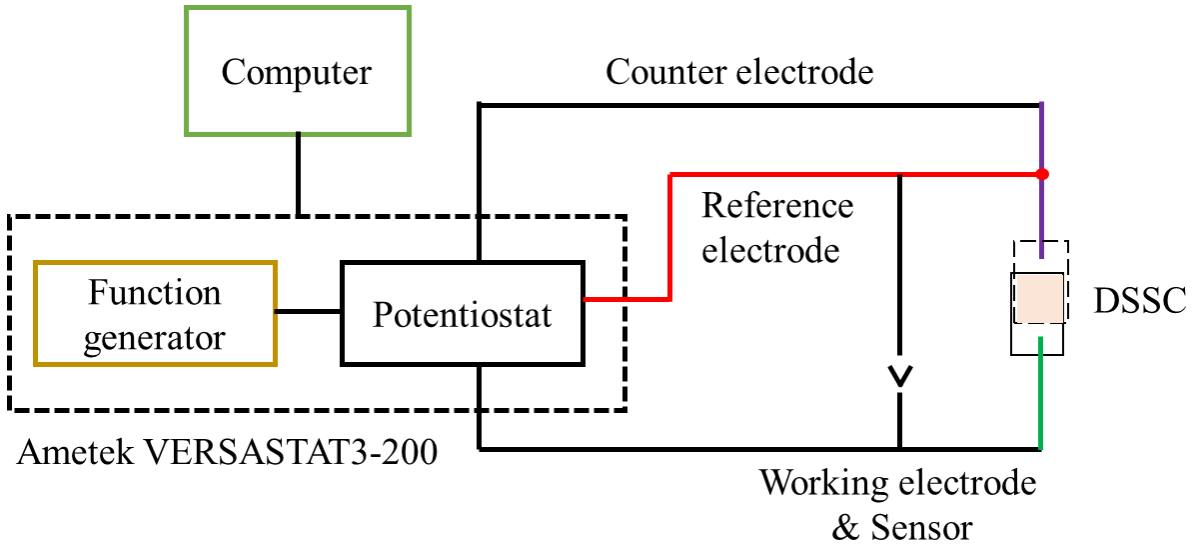

Figure 3.4. Functional diagram of EIS system. Modified from [149].

3.2.7. Measurements of transient photovoltage and photocurrent

The transient decays of photovoltage and photocurrent were measured using OBB's Model OL-4300 nitrogen laser, and the procedures followed the methods reported in the literature [150-152]. The setup for measuring the transient decay of photovoltage is shown in Figure 3.5(a). The DSSC was exposed to the white bias light from an array of light emitting diodes (LEDs) to generate a photovoltage. A red light pulse with pulse width of 300 μs and rise and fall of 300 ns was

generated from an LED controlled by a fast solid-state switch. The pulse produces a small increase in the photovoltage, and the decay of this photovoltage was recorded using an oscilloscope. The signal decay in this setup represents the electron recombination lifetime (τ_e). The transient photocurrents were measured at V_{oc} and I_{sc}. Figure 3.5(b) shows the setup for measurement at V_{oc}. In this setup, the V_{oc} of the DSSC under the white bias light was offset by a constant voltage that was exactly the same as V_{oc} while the polarity was in the opposite direction. A pulse of red LED resulted in current flow through the external load, and the current decay on a 50 Ω resistor was recorded with an oscilloscope. For the photocurrent decay at I_{sc}, the decay was recorded without the voltage offset from the power source. The perturbation signal was feeble enough and it was justifiable to express the photocurrent decay as a single exponential decay. Since the transport time was much faster than the recombination lifetime, the fitted decay time could precisely represent the electron transport time (τ_{trans}). Further, no substantial difference was noticed in lifetime between photocurrent decay measurement under V_{oc} or I_{sc}. Therefore, the τ_{trans} reported in this study was extracted from the photocurrent measurement under I_{sc} to ensure the simplicity of the setup along with a better signal to noise ratio.

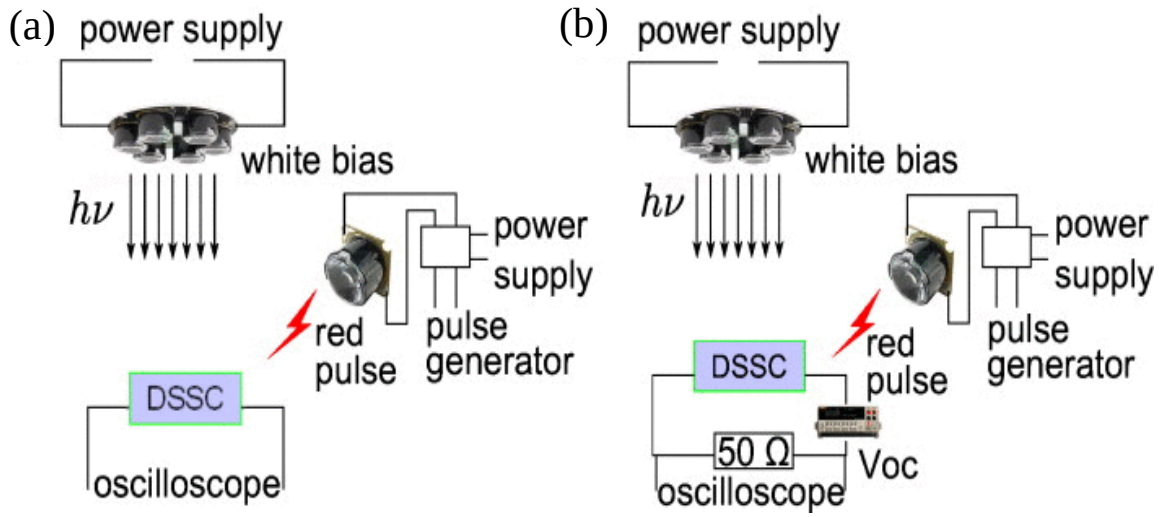

Figure 3.5. Experimental setup for transient (a) photovoltage and (b) photocurrent decay measurements [153].

3.3. Results and Discussion

3.3.1. Morphology and structure characterization

The XRD pattern shown in Figure 3.6(a) indicates a high purity of SnO_2 nanofibers annealed in air at 500 °C. Peaks with 2θ values of 26.48, 33.87, 37.91, 51.72, 54.85, and 57.97 were observed, which correspond to SnO_2 crystal planes of (110), (101), (200), (211), (220), and (002), respectively. No obvious impurity peaks (e.g., unreacted Sn metal and other tin oxides) were observed, indicating the high purity of the rutile SnO_2 nanofibers. These signature diffraction peaks indicate a tetragonal rutile structure of SnO_2 with lattice constants of $a, b = 4.74$ Å and $c = 3.18$ Å that agree well with documented values for the SnO_2 crystals (JCPDS card, No. 41-1445). Scherrer's equation was adopted to estimate the size of SnO_2 crystals in the form of powder. It is stated that the average crystallite size $D = 0.89\lambda/\beta \cos\theta$, where λ is the wavelength for the Cu-Kα (= 1.54056 Å), β is the line broadening at half the maximum intensity (FWHM) expressed in radian, and θ is Bragg's angle. The average crystallite size was calculated to be approximately 6 nm for SnO_2 nanofibers based on the (211) peak [154, 155].

The microstructure of the SnO_2 nanofibers was also examined using a high-resolution TEM image shown in Figure 3.6 (b). The TEM image clearly reveals a single-crystalline structure of SnO_2 that retains an intact and uniform fibrous morphology. A relatively uniform diameter of 200-300 nm was observed and there was no phase separation between PVP and Sn precursor at the boundary. In addition, The SnO_2 nanofiber has a smooth and compact surface without any porous structures, which might be due to the high molecule weight of PVP and high concentration of electrospinning solution [144].

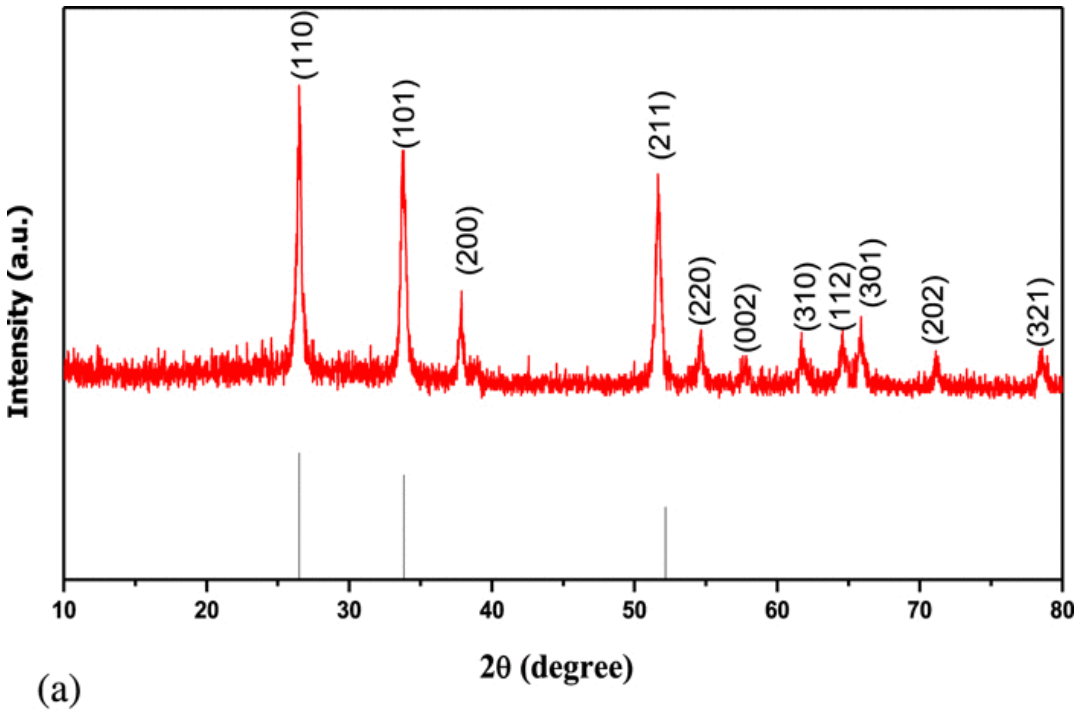

(a)

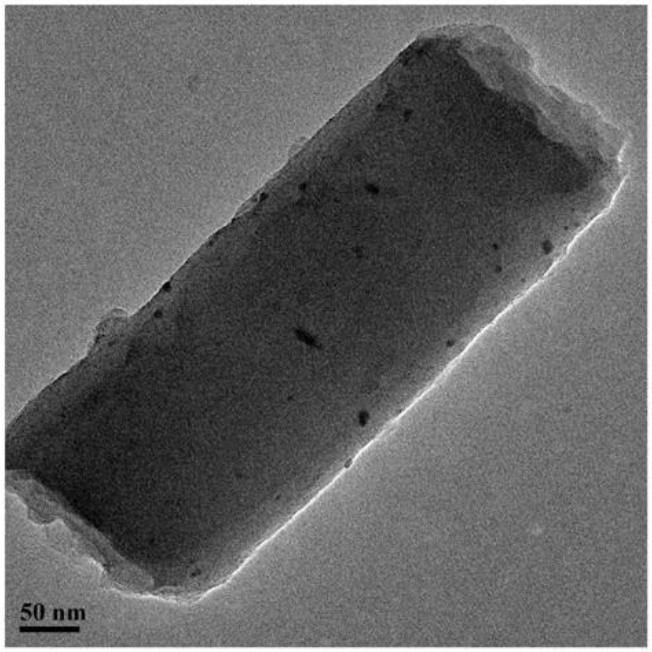

(b)

Figure 3.6. (a) X-ray powder diffraction pattern of SnO_2 nanofibers and (b) transmission electron microscopy image of a single SnO_2 nanofiber.

The PVP/$SnCl_4 \cdot 5H_2O$ precursor nanofibers were heat-treated at 500 °C. During heat treatment, PVP matrix was decomposed and $SnCl_4 \cdot 5H_2O$ precursor transformed to SnO_2 nanofibers. Figure 3.7(a) shows the scanning electron micrographs (SEM) of the as-spun PVP/$SnCl_4 \cdot 5H_2O$ precursor nanofibers. It can be seen that SnO_2 nanofibers have a smooth surface and exhibit fibrous morphology, good rigidity and are separated from each other. These nanofibers are continuous and form a self-supporting network with a relatively uniform diameter ranging between 200 and 300 nm and lengths of at least tens of microns. Due to weak adhesion between the original SnO_2 nanofiber sheets and FTO substrate, the nanofiber sheets were dispersed into short fiber fragments by ultrasonication. The short fibers were made into a paste based on the procedure described in Chapter 3.2.3. The paste was doctor-bladed onto FTO glass and annealed at 500 °C to form photoanode, which has the topology shown in Figure 3.7(b). As can be seen, the photoanode film comprising microscale agglomerates of short SnO_2 nanofibers exhibits a highly porous and rough surface morphology. This may be due to the fact that there exists a Sn precursor/SnO_2 concentration gradient which causes surface diffusion during the calcination process. Since the continuous SnO_2 nanofibers were truncated and crushed into a film of randomly oriented short fragments, a large amount of voids was formed within the photoanode as seen in Figure 3.7(b). These voids not only affected the connectivity of the nanofiber network, but also reduced the surface area of photoanode, which in turn led to a lower amount of dye uptake. To minimize the number of voids and increase the surface area, closely packed TiO_2 nanoparticles were introduced into SnO_2 nanofiber network to form a compact film morphology as shown in Figure 3.7(c). It can be seen that the P25 TiO_2 nanoparticles were infiltrated into the SnO_2 nanofibers which were shortened and broken through ultrasonication. In addition, the SEM image of the composite shows that there exists no interconnected nanofiber network.

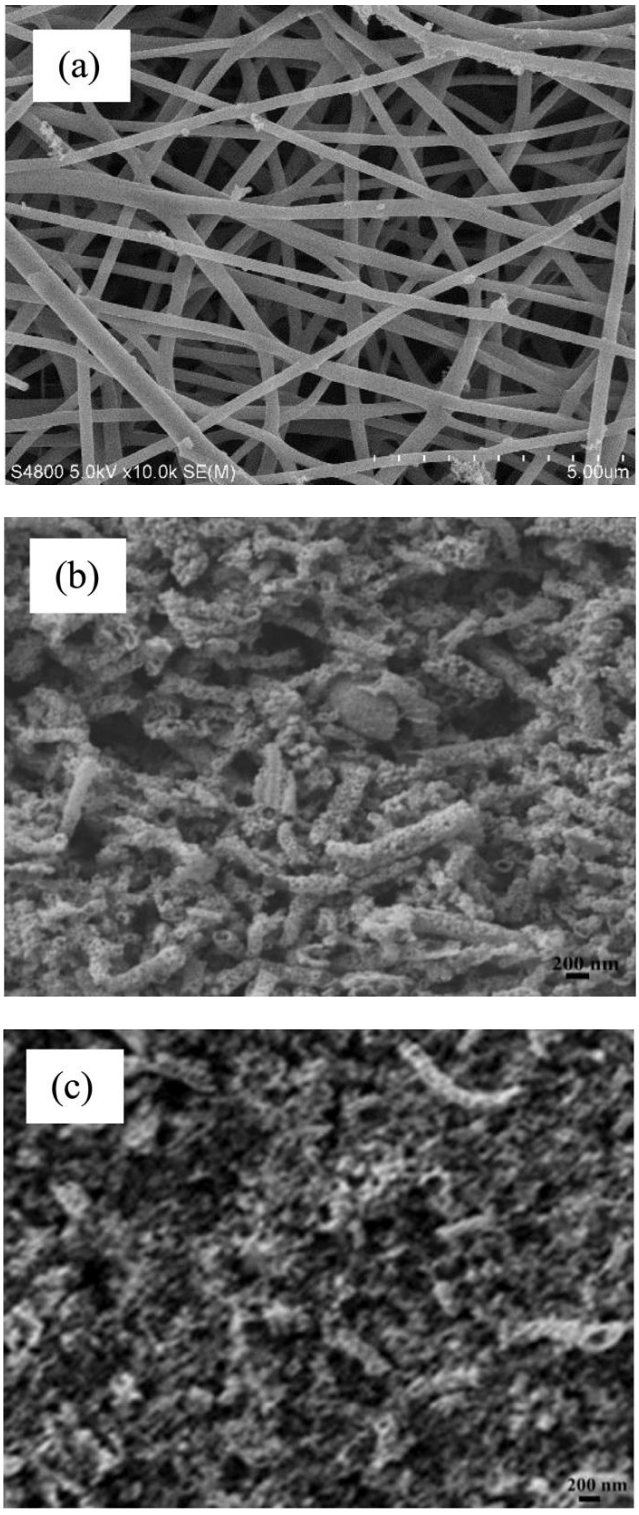

Figure 3.7. Scanning electron micrographs of (a) electrospun SnO_2 nanofiber network calcinated at 500 °C, (b) short SnO_2 nanofibers randomly packed on FTO glass substrate, and (c) SnO_2 nanofiber/TiO_2 nanoparticle composite (weight ratio: 1:1).

3.3.2. Photovoltaic performance of SnO_2 nanofiber based DSSCs

Three samples of each type of device were tested under AM 1.5 illumination at a light intensity of 100 mW/cm^2. Figure 3.8 shows the comparison of J-V characteristics of DSSCs based on the SnO_2 nanofiber and SnO_2/TiO_2 composite. The photovoltaic parameters are listed in Table 3.1. The SnO_2 nanofiber based device shows poor performance with an open-circuit voltage (V_{oc}) of 0.7 V, a short-circuit current density (J_{sc}) of 5.9 mAcm^{-2}, and an overall conversion efficiency (η) of 1.68%. A reasonably low open-circuit voltage (0.7 V) is consistent with the fact that the conduction band potential of SnO_2 nanofibers is 0.4 V more positive than that of nanocrystalline TiO_2 [80, 156, 157]. Additionally, the low current density can be mainly ascribed to insufficient dye attachment, which was confirmed by UV-Vis absorbance spectra shown in Figure 3.9(a). It can be seen that dye solution derived from the SnO_2 nanofiber photoanode has a lower absorbance, indicating a lower amount of dye molecules attached to the photoanodes in the DSSCs. A comparatively low fill factor (FF) of 0.41 was observed, which was caused by high charge resistance in the porous SnO_2 film due to randomly packed short fibrous morphology. For each device, charge diffusion length (L) was calculated based on time constant derived from transient photovoltage and photocurrent analysis, shown in Figure 3.10. A long diffusion length (62.42 μm) of SnO_2/TiO_2 composites indicates a small magnitude of recombination dynamics.

Table 3.1. Photovoltaic parameters of DSSCs based on SnO_2 nanofiber and SnO_2/TiO_2 composite photoanode.

Samples	V_{oc} (V)	J_{sc} (mAcm^{-2})	FF	η (%)	L (μm)
SnO_2 nanofiber	0.70±0.003	5.9±0.05	41±0.1	1.68±0.05	55.68±0.93
SnO_2/TiO_2 composite	0.79±0.04	10.1±0.07	57±0.3	4.54±0.1	62.42±1.25

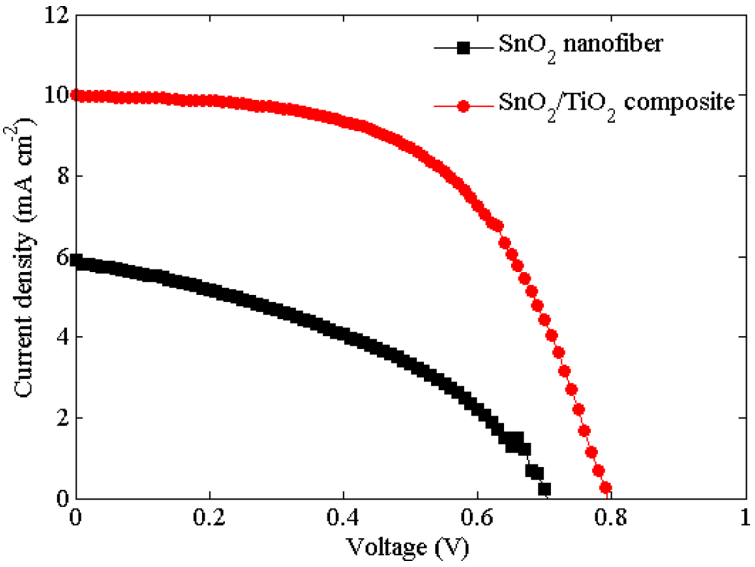

Figure 3.8. Comparison of current density versus voltage (J-V) curves of SnO_2 nanofiber, and SnO_2/TiO_2 composite based DSSCs.

In contrast, SnO_2/TiO_2 composite shows an over 2-fold improvement compared to SnO_2 nanofiber with a V_{oc} of 0.79 V, a J_{sc} of 10.1 $mAcm^{-2}$, a FF of 0.57, and an overall efficiency η of 4.54%. The increase in V_{oc} from 0.7 to 0.79 V can be attributed to the alleviated shift in SnO_2 conduction band edge by virtue of adding TiO_2 nanoparticles into SnO_2 nanofiber network. The improvement in short circuit current density is mainly due to the increase in dye attachment as shown in Figure 3.9(a). The enhanced fill factor is likely a result of low electron recombination rate due to the formation of TiO_2 blocking layer. The experimental results derived from transient and EIS analyses support that a thin TiO_2 blocking layer can effectively suppress electron recombination at the FTO/electrolyte interface [158].

3.3.3. UV-Vis absorbance spectrum of SnO_2 nanofiber based photoanode

The UV-Vis absorbance spectra of N719 dyes derived from SnO_2 nanofibers and their composites are shown in Figure 3.9(a). As can be seen, the N719 dye exhibits two absorption peaks at 360 and 510 nm, corresponding to metal-ligand charge transfer transitions [159]. It shows

at maximum absorption wavelength ($\lambda_{max} = 512\ nm$), the SnO_2/TiO_2 composite absorbed ~30% more dye molecules than the SnO_2 nanofibers, whereas the composite based DSSCs generated over 2-fold power conversion efficiency. Such significant improvement can be attributed to increased surface area and more compact morphology introduced by TiO_2 nanoparticles. It has been found that when the diameters of nanofibers increased to 200 nm or beyond, the light scattering becomes substantially stronger [80]. Since the diameters of the electrospun SnO_2 nanofibers were about 200-300 nm, these nanofibers were expected to induce strong light scattering and thereby significantly enhance the light harvesting. This prediction was supported by the transmittance spectra of SnO_2 nanofiber and SnO_2/TiO_2 composite based photoanodes, as shown in Figure 3.9(b). The SnO_2 nanofiber based cells showed a broad light absorption property from 400 nm to 800 nm with a minimum transmittance of 14% at green light (530 nm). This light harvesting capability can be attributed to multiple light scattering in large SnO_2 agglomerates scattered in the electrode. SnO_2/TiO_2 composite based photoanode has a higher transmittance compared to SnO_2 nanofiber photoanode.

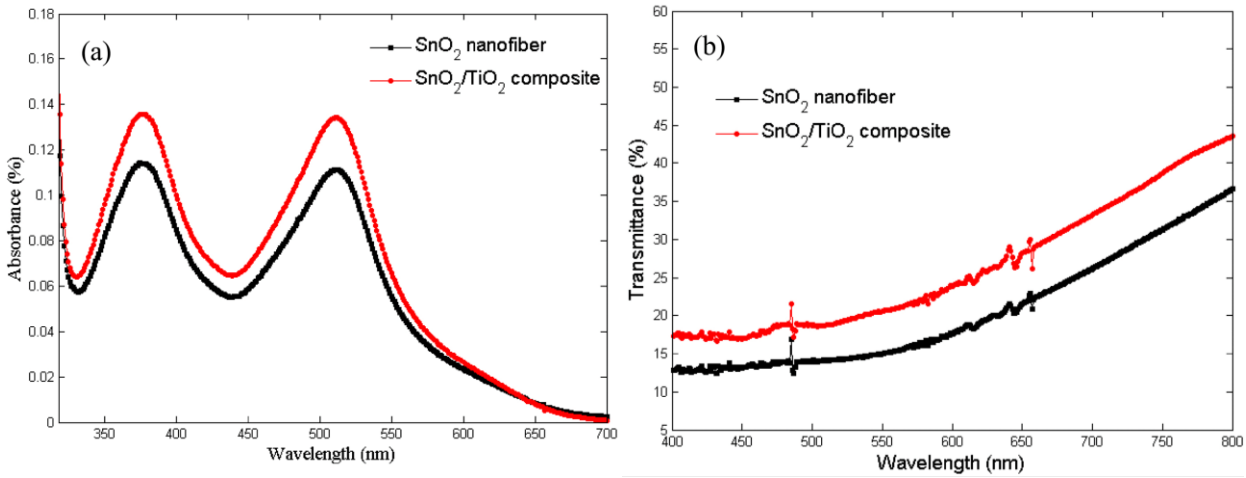

Figure 3.9. (a) UV-Vis absorbance spectra from the solutions of dyes that were desorbed from SnO_2 nanofiber and SnO_2/TiO_2 composite based photoanodes. (b) Transmittance spectra before dye soaking.

3.3.4. Photovoltage and photocurrent decay

Transient photovoltage is one of the major characterization techniques to analyze recombination dynamics of excess electrons in solar cells. Figure 3.10(a) shows the normalized transient photovoltage decay of SnO_2 nanofiber and SnO_2/TiO_2 composite. The decay of a small voltage perturbation is a single exponential function with time, which can be fitted in Origin® to derive the value of time constant (τ_e). The competition between recombination and charge transport determines the diffusion length of electrons, which measures the average distance that the electrons can travel in the photoanode without recombination. Diffusion length, L, is calculated using the equation:

$$L = \sqrt{D_n \tau_e} = \sqrt{\frac{w^2 \tau_e}{2.35 \tau_{trans}}} \tag{3.1}$$

where w is the thickness of photoanode, τ_e is the electron recombination lifetime, τ_{trans} is the electron transport lifetime, and D_n is the effective diffusion coefficient [153]. Electron recombination time of SnO_2/TiO_2 composite is comparable to SnO_2 nanofiber (21.8 ms); both have a long recombination time. The long transient photovoltage decay in the composite is resulted from slow recombination dynamics due to $TiCl_4$ post-treatment. It has been found that an energy barrier of approximately 300 mV created by TiO_2 layer prevents back charge transfer from SnO_2 to the electrolyte or dye [160]. It can be seen, in Figure 3.10(b), that the addition of TiO_2 nanoparticles in SnO_2 nanofibers reduces the decay time constant τ from 0.2 to 0.15 ms, which shows an improvement in charge transport and collection. A relatively slow charge collection in SnO_2 nanofiber based devices can be attributed to lower bulk electron mobility that is caused by boundaries and defects of SnO_2 nanofibers in the film.

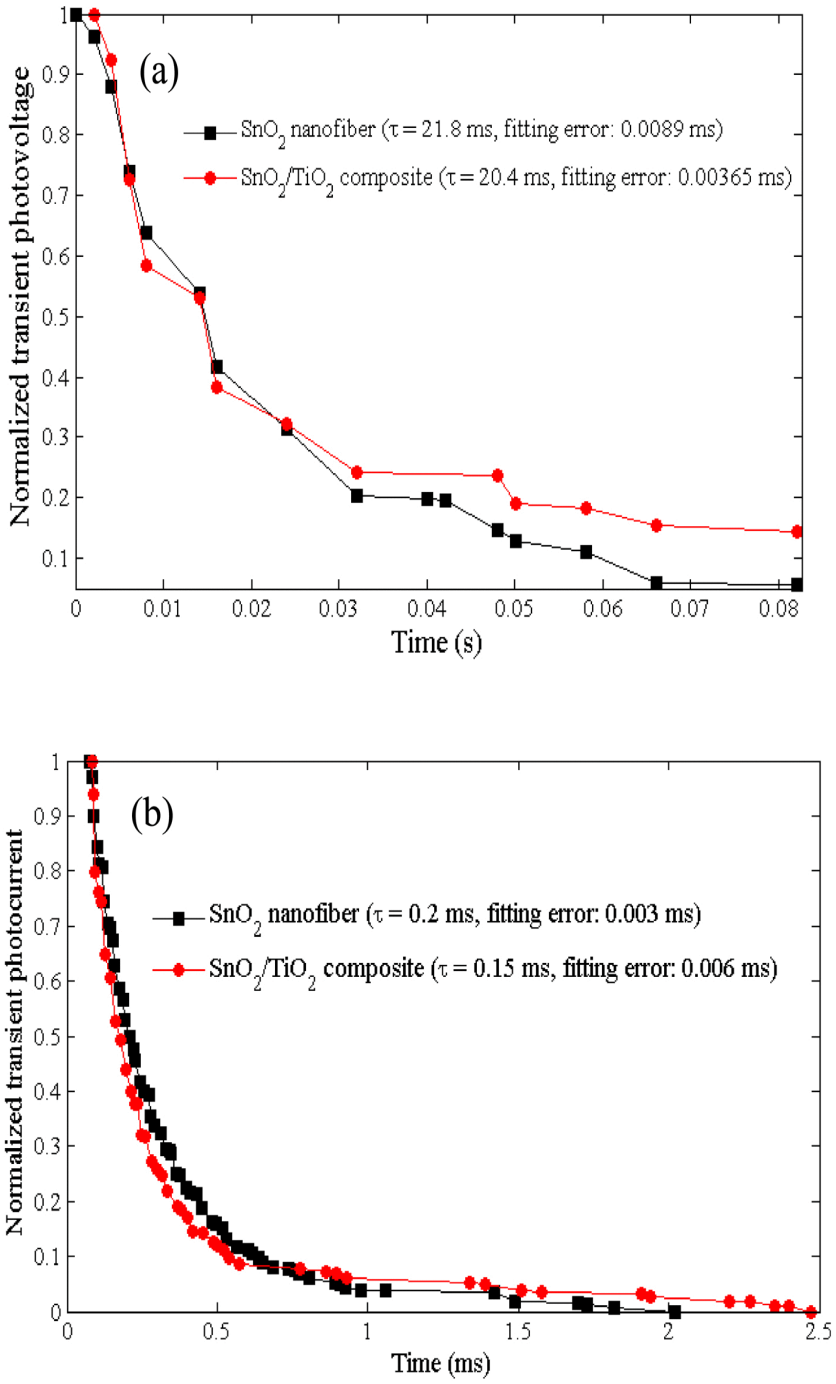

Figure 3.10. Normalized transient (a) photovoltage and (b) photocurrent decay of SnO_2 nanofiber and SnO_2/TiO_2 composite based DSSCs.

3.3.5. EIS characterization

Electrochemical impedance spectroscopy (EIS) analysis was carried out to further investigate the salient electronic and ionic processes occurring in the SnO_2 based DSSCs. This technique uses a very small amplitude of AC voltage, which exerts minimum perturbation on the device. Figure 3.11(a) shows impedance spectra of SnO_2 nanofiber and SnO_2/TiO_2 composite based DSSCs measured at forward bias (V_{oc}) in the dark. Two semicircles can be clearly observed in each spectrum: the left side (high-frequency region) represents the charge transfer at the electrolyte/counter electrode interface; the right side (intermediate-frequency region) represents the back charge transfer from the photoanode to electrolyte [161, 162]. The equivalent circuit used in analyzing the EIS spectra is presented in Figure 3.11(b). Each of the two interfaces was modeled by a parallel combination of a resistance and a capacitor. As shown in the figure, R_S represents the total series resistance of a device, R_{CT} is the charge transfer resistance at the electrolyte/counter electrode interface, and R_{CR} is the charge recombination resistance at the photoanode/electrolyte interface. The values of R_S, R_{CT}, and R_{CR} are extracted by fitting equivalent circuit and presented in Table 3.2. A large value of R_S (20.58 Ω) in SnO_2 nanofiber compared to SnO_2/TiO_2 composite (17.45 Ω) indicates a slower charge transport in SnO_2 due to a slow interparticle electron motion in the porous SnO_2 film [163]. This high total series resistance is in accordance with the low fill factor in SnO_2 nanofiber based devices. The R_{CT} values in all devices are consistent as the electrolyte and counter electrode were kept the same. A significantly large charge recombination resistance (303.7 Ω) in SnO_2 nanofibers was observed. This implies a slow recombination in the SnO_2 nanofibers, and a fast charge transport and collection in SnO_2 nanofiber based photoanode. All the experimental results reported in this chapter have been published in *AIP Advances* in 2015 [17].

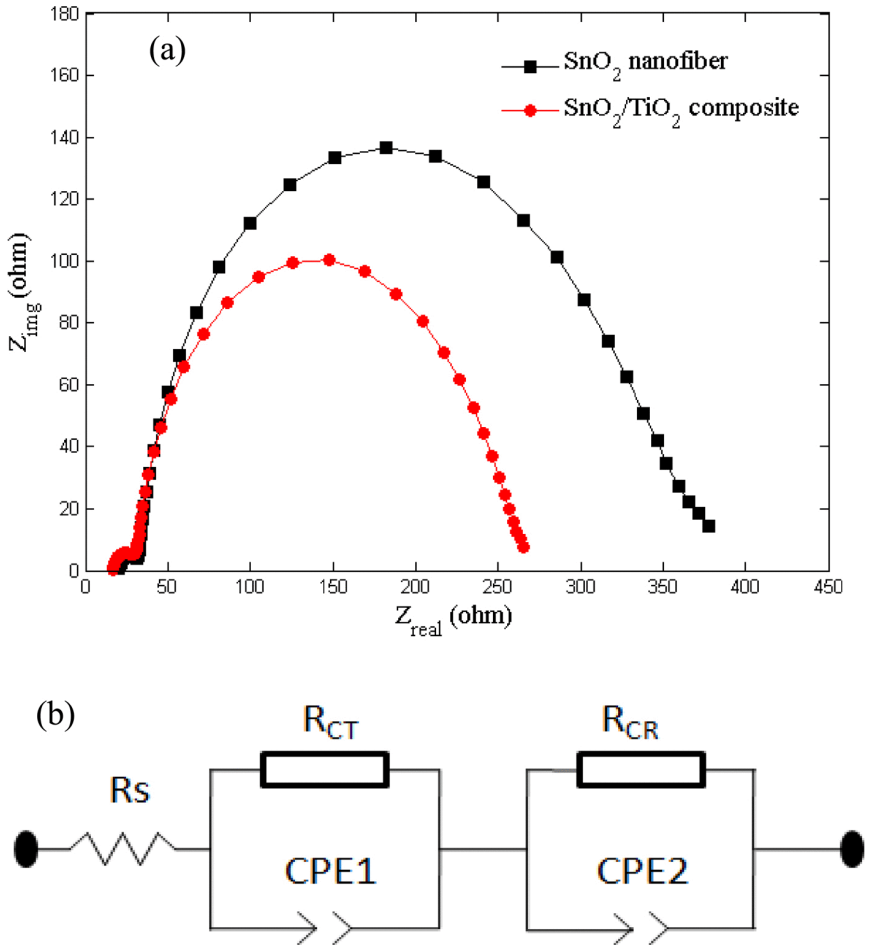

Figure 3.11. (a) Nyquist plots of SnO_2 nanofiber and SnO_2/TiO_2 composite based DSSCs in dark at a bias of V_{oc} from 0.1 Hz to 100 Hz with an amplitude of 10 mV, and (b) equivalent circuit model for a full cell.

Table 3.2. Fitted value of R_S, R_{CT}, and R_{CR} for SnO_2 nanofiber and TiO_2 nanoparticle based DSSCs.

Samples	R_S (Ω)	R_{CT} (Ω)	R_{CR} (Ω)
SnO_2 nanofiber	20.58	16.81	303.7
SnO_2/TiO_2 composite	17.45	13.54	217

3.4. Summary

In this study, electrospun SnO_2 nanofibers and their composites were fabricated and investigated for use as electrode material in dye-sensitized solar cells. The microstructure of SnO_2 nanofibers was characterized by XRD and TEM. The XRD pattern indicates a high purity of the single-crystalline rutile SnO_2 and TEM image reveals that SnO_2 nanofibers retain an intact and uniform fibrous morphology with the diameter of 200-300 nm. The UV-Vis spectra show that the photoanode made of SnO_2 nanofibers have broad light absorption from 400 nm to 800 nm with a minimum transmittance of 14% at green light (530 nm) and that SnO_2/TiO_2 composite can absorb ~30% more dye molecules than the SnO_2 nanofibers. Compared to SnO_2 nanofiber based DSSCs, the device made of SnO_2/TiO_2 composites showed an over 2-fold improvement with a V_{oc} of 0.79 V, a J_{sc} of 10.1 $mAcm^{-2}$, a FF of 0.57, and an overall efficiency of 4.54%. Such remarkable cell performance improvement can be attributed to a compact morphology of SnO_2/TiO_2 composites, a large surface area introduced by the TiO_2 nanoparticles, and a reduced interfacial charge recombination resulting from $TiCl_4$ treatment. In addition, experimental results obtained from transient photovoltage and photocurrent analysis show that SnO_2/TiO_2 composites possess a longer charge diffusion length (62.42 μm) compared to SnO_2 nanofibers (55.68 μm). The high diffusion length indicates efficient charge transport and collection processes, which is a result of the excellent connectivity between SnO_2 nanofibers and TiO_2 nanoparticles in the composites. It is also worth noting that a thin film (8-9 μm) photoanode would mitigate charge recombination and reduce series resistance, which is desirable in improving cell efficiency. These experimental results in this study have demonstrated that one-dimensional nanostructured SnO_2/TiO_2 composites have a great potential for solar cells application.

4. CHARACTERISTICS OF HOLLOW TIN OXIDE NANOFIBER AND TITANIUM DIOXIDE NANOPARTICLE COMPOSITE FOR DYE-SENSITIZED SOLAR CELLS

4.1. Introduction

As discussed in the previous chapter, one-dimensional (1D) SnO_2 nanofibers hold great potential as low-cost electrode materials for use in DSSCs due to their supreme light scattering capability, high electron mobility, and ease of fabrication. In light of these advantages, this chapter discusses the synthesis route and photovoltaic performance of 1D hollow SnO_2 nanofibers. These nanofibers were fabricated by the electrospinning techniques similar to that described in Chapter 3, except that the electrospun PVP/Sn precursor nanofibers were carbonized at an elevated temperature (600 °C). During the carbonization process, a hollow structure was formed because of the Kirkendall effect and surface diffusion. The resulting hollow SnO_2 nanofibers and their composites (SnO_2/TiO_2) were for the first time used as high-performance electrode material for DSSCs. The microstructure of the hollow SnO_2 nanofibers was investigated using SEM, TEM, and XRD, and the dye uploading capacities were measured using UV-Vis absorbance spectrum. The photovoltaic performance of SnO_2 nanofiber based DSSCs was evaluated based on the J-V characteristics and incident photon-to-electron conversion efficiency (IPCE). Additionally, the electron transport and recombination lifetimes were derived from transient photocurrent (TPC) as well as transient photovoltage (TPV) measurements. The above-mentioned microstructure and photovoltaic properties of hollow SnO_2 nanofibers are detailed in this chapter. The related mechanisms are also explored to correlate the photovoltaic performance of the hollow SnO_2 nanofibers to their unique microstructure.

4.2. Experimental Methods

4.2.1. Preparation of hollow SnO_2 nanofibers

The electrospinning solution was prepared by adding $SnCl_4 \cdot 5H_2O$ into 10 wt% polyvinyl pyrrolidone (PVP) in ethanol/DMF solvent mixture. The weight ratio of $SnCl_4 \cdot 5H_2O$ to polymer intermediate was fixed at 1:1. The solution was stirred by magnetic stirring at ambient temperature. Subsequently, electrospinning was carried out using this solution. The PVP/ $SnCl_4 \cdot 5H_2O$ precursor was ejected from a stainless steel needle under a high voltage of 17 kV, and formed nonwoven fibrous mats on the collector. The flow rate of the electrospinning solution has an influence on both the diameter and specific surface area of the nanofibers. In general, the diameter of nanofibers increases with an increase in flow rate. At high flow rates, significant variations in the thickness of nanofibers can be observed [164]. In order to obtain nanofibers with a uniform diameter, the flow rate was maintained at 1 ml/h, and the needle-to-collector distance was fixed at 21 cm. The electrospun nanofiber mats were calcinated in air at 600 °C for 4 h at a heating rate of 0.5 °C/min.

4.2.2. Preparation of porous SnO_2 nanofiber paste

Ethyl cellulose (100 mg) was mixed with 5 ml of ethanol using magnetic stirrer for 30 min. Then, 100 mg of grinded porous hollow SnO_2 nanofibers and 0.5 mL of α-terpineol were added to the solution. The resulting solution was ultrasonicated for 15 min and left for magnetic stirring for 3 hours. Subsequently, another magnetic stirring was performed on a hot plate at 75 °C until the paste obtained was suitable for doctor blading. Similarly, the paste of SnO_2/P25-TiO_2 was prepared by adding SnO_2 (50 mg) and P25-TiO_2 (50 mg) in the weight ratio 1:1 by following the above-mentioned procedures. It should be pointed out that commercially available P25-TiO_2 nanopowder has primary particle size of ~21 nm.

4.2.3. Fabrication and characterization of DSSCs

4.2.3.1. Preparation of photoanodes

Substrate preparation was undertaken under ambient conditions. First, the TEC8 FTO-coated glasses (~8 Ω/sq sheet resistivity, purchased from Hartford Co.) were cleaned with a 2% solution of anionic detergent (Sodium dodecyl sulfate, 99% purity) diluted in deionized water. Next, the glass substrates were rinsed with deionized water, acetone and ethanol, before being dried with clean nitrogen gas. An acidic solution of titanium isopropoxide in ethanol was coated onto the clean substrates through two consecutive spin-coating steps at 4,000 rpm and 3,000 rpm for 40 s and 20 s, respectively. The substrate was then dried on a hot plate at 115 °C for 15 min and sintered at 475 °C for 30 min to form a compact n-type of TiO_2 layer. Finally, ~6.5-7 µm thick SnO_2 layer was doctor bladed on an FTO-glass substrate, followed by deposition of ~4 µm thick light scattering layer (Solaronix Ti-Nanoxide R/SP) and treatment in 0.2 M $TiCl_4$ aqueous solution (optimum concentration) at 80 °C for 30 min. After each step, the sample was dried at 115 °C for 15 min and then sintered at 475 °C for 30 min to remove organic components. The resulting film was then immersed in dye solution containing 0.3 mM Ruthenizer 535-bisTBA dye (N-719) in acetonitrile/t-butanol at volume ratio of 1:1 for 30 h at room temperature. Lastly, the photoanode was kept in acetonitrile for 3 h to remove any excess dye. In addition, the reference photoanode was prepared using ~14 µm thick nanocrystalline TiO_2 (Solaronix Ti-Nanoxide HT/SP) as the active layer, which has been optimized to achieve the highest power conversion efficiencies. The thickness of the nanocrystalline TiO_2 layer was separately measured after sintering without scattering layers by using a surface profiler.

4.2.3.2. Assembly of the DSSCs

Platinum (Pt) precursor solution (0.02 M $H_2PtCl_6 \cdot 5H_2O$ in anhydrous ethanol) was spin-coated on an FTO-glass substrate at 2,000 rpm for 20 s. The substrate was then heated at 400 °C for 15 min in the oven to obtain a counter electrode (CE). An electrolyte containing 0.03 M I_2, 0.60 M 1-butyl-3-methylimidazolium (BMII), 0.10 M guanidine thiocyanate, and 0.50 M tert-butylpyridine in acetonitrile and valeronitrile (85:15, volume ratio) was then injected into the cells through the reserved channel. The procedure was complete after the channel was sealed by hot glue. Thus, the fabricated DSSCs had a resulting active area of 0.125 cm^2.

4.2.3.3. Dye desorption from photoanode

To measure the amount of attached dye onto the photoanode, dye molecules on each photoanode were desorbed into 2 mL of 10 mM NaOH solution at room temperature for 24 h. The NaOH solution was prepared by dissolving NaOH in the mixture of ethanol and water at 1:1 ratio by volume. Then, UV-Vis absorption spectroscopy was performed to measure the amount of dyes desorbed from different photoanodes using Beer-Lambert equation,

$$C_{dye} = \frac{A}{\epsilon(\lambda)\, l} \tag{4.1}$$

where A is the light absorbance, $\epsilon(\lambda)$ is the molar extinction coefficient of N719 dye, C_{dye} is the absorbed dye concentration on the photoanode, and l is the path-length of the sample. As shown in Eq. (4.1), given the same molar extinction coefficient and sample path-length, the concentration of dye molecules is proportional to the light absorbance.

4.2.3.4. Device characterization

The J-V characteristics of the DSSCs were tested under AM 1.5 illumination at a light intensity of 100 mW/cm^2. For this measurement, a Xenon arc lamp with AM 1.5 filter was used as light source. Electrochemical impedance spectroscopy (EIS) was conducted using a PC-

controlled Ametek VERSASTAT 3-200 potentiostat with a frequency analysis module. The AC signal of amplitude 10 mV in the frequency range from 0.1 to 10^5 Hz was applied at a certain DC bias voltage (open-circuit voltage) under dark conditions.

4.2.3.5. External Quantum Efficiency Measurements

External quantum efficiency (EQE), also commonly referred as incident photon-to-current efficiency (IPCE), indicates the ratio between the number of collected charge carriers and the numbers of photons incident on solar cells. It is a measure of how efficiently the solar cells convert the incident light into electricity at a given wavelength. The schematic diagram of the EQE/IPCE measurement system is presented in Figure 4.1. The main components of the system include the light source, monochromator, trans-impedance amplifier, software and related electronics.

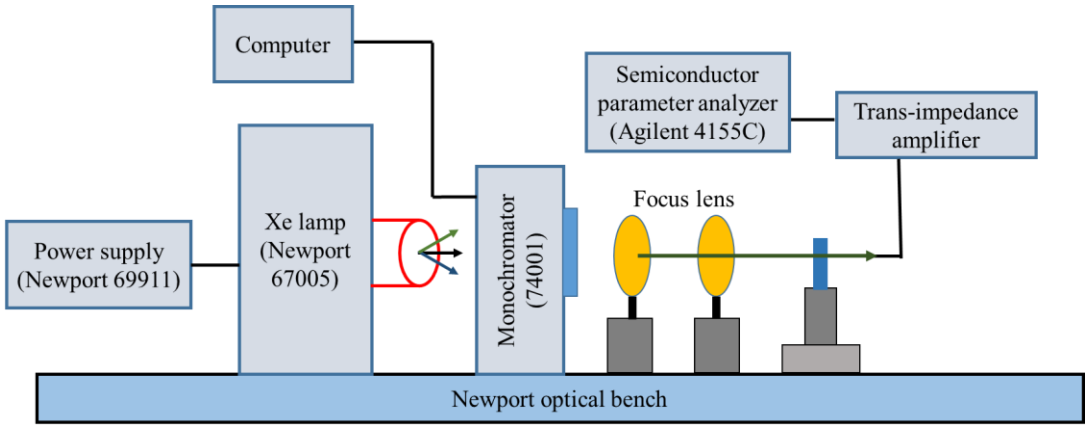

Figure 4.1. Schematic of EQE/IPCE measurement system.

When in operation, the simulated sunlight was first generated from the Xe lamp (300-Watt, Newport 67005), and then focused on a Si-based reference cell (S1133, Hamamatsu) through a monochromator and two focusing lenses. The monochromator (Oriel Monochromator 74001) controlled by a PC was programed to transmit the light at a specific wavelength, ranging from 350 to 800 nm at an interval of 5 nm. Finally, the trans-impedance amplifier was used to convert the

photocurrent to the voltages (V_{ref}), which was in turn recorded using semiconductor parameter analyzer (Agilent 4155C). In the measurement, the reference cell was replaced with the DSSC samples, and the output voltage of DSSCs (V_{sample}) at each wavelength was recorded. The EQE relationship between the reference cell (EQE_{ref}) and the tested DSSC samples (EQE_{sample}) is described as:

$$EQE_{sample} = \frac{V_{sample} \times EQE_{ref}}{V_{ref}} \tag{4.2}$$

Furthermore, the precise value of J_{sc} can be calculated by integrating the product of IPCE and incident photon flux (Φ_0) over the spectral distribution, expressed as:

$$J_{sc} = e \int IPCE(\lambda)\Phi_0(\lambda)\big(1 - r(\lambda)\big)d\lambda \tag{4.3}$$

where 'e' is the elementary charge and $r(\lambda)$ is the incident light loss. The above equation suggests that the J_{sc} can be enhanced with an increase in IPCE value, which can be realized through utilizing panchromatic dyes which have strong light absorption over the whole solar spectrum.

4.3. Results and Discussion

4.3.1. Morphology and structure characterization

Figure 4.2 shows SEM image of the SnO_2 nanofibers calcinated at 600 °C. It can be seen that these nanofibers have a hollow structure and dense shells, comprising numerous nanograins with a particle size of approximately 17 nm. Besides the particle size, the hollow SnO_2 nanofibers have a relatively uniform diameter ranging from 100 to 150 nm, which is reflected in the TEM image (Figure 4.3). From the figure, it can be clearly seen that there exist numerous grain boundaries on the shell of hollow nanofibers. The formation of the hollow nanofibers with nanograins on the shell can be attributed to the Kirkendall effect and surface diffusion during the calcination process at elevated temperature. Figure 4.4 shows the powder XRD patterns from a

prepared sample of hollow SnO_2 nanofibers. This sample exhibits sharp diffraction peaks which can be indexed to tetragonal rutile phase of SnO_2 (JCPDS card no 41-1445). Noticeably, there exists no impurity peaks in XRD pattern, indicating high purity of the rutile phase.

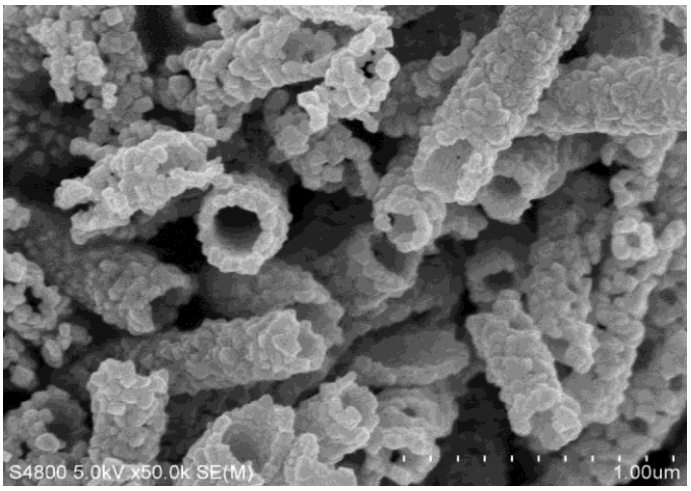

Figure 4.2. SEM image of hollow SnO_2 nanofibers.

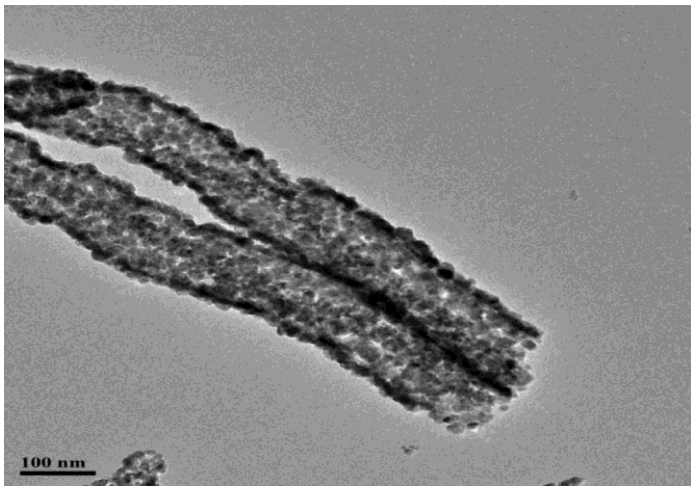

Figure 4.3. TEM image of hollow SnO_2 nanofibers.

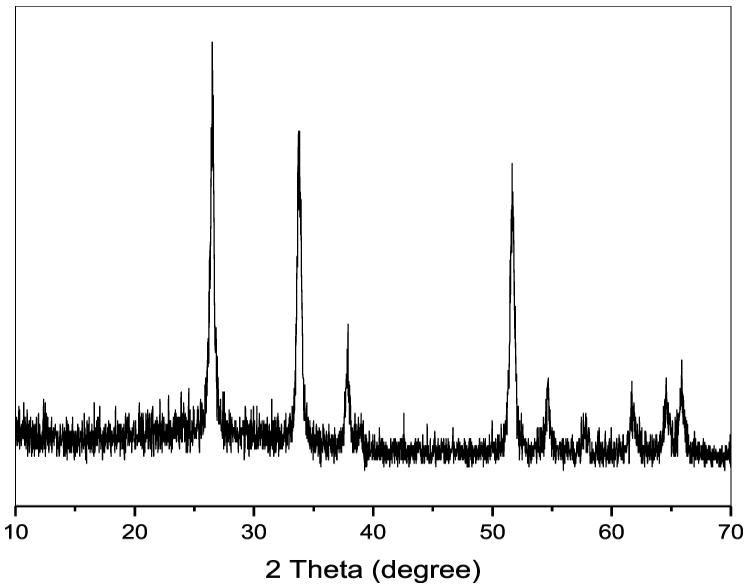

Figure 4.4. XRD patterns of hollow SnO_2 nanofibers.

4.3.2. Photovoltaic performance of hollow SnO_2 nanofiber based DSSCs

Figure 4.5(a) shows the current density versus voltage (J-V) curves of $TiCl_4$ treated SnO_2 nanofiber, SnO_2/P25-TiO_2, and nanocrystalline TiO_2 based DSSCs under AM 1.5 illumination with a light intensity of 100 mW/cm^2. As listed in Table 4.1, the power conversion efficiencies (η) of SnO_2 nanofiber, SnO_2/P25-TiO_2, and nanocrystalline TiO_2 based DSSCs are 4.06%, 5.72%, and 7.12%, respectively. It should be pointed out that addition of P25-TiO_2 to SnO_2 nanofibers resulted in an increase in the J_{sc} from 10.75 to 11.97 mA/cm^2 as well as FF improved from 0.50 to 0.60. Similarly, a marginal increase in V_{oc} was noticed from 0.75 to 0.8 V. Note that both types of DSSCs (SnO_2 and SnO_2/P25-TiO_2) were post-treated with $TiCl_4$ to form a recombination barrier layer which resulted in higher values of V_{oc}. The nanocrystalline TiO_2 based control device had J_{sc}, V_{oc}, and FF of 12.78 mA/cm^2, 0.79 V, and 0.71, respectively. For each device, charge diffusion length was calculated based on Equation 3.1, in which time constants were derived from TPC and TPV analyses as shown in Figure 4.7. A long diffusion length (52.70 μm) of nanocrystalline TiO_2 indicates electrons are less prone to recombination losses and therefore have a long lifetime.

Figure 4.5(b) presents the incident photon-to-current conversion efficiency (IPCE) spectral action responses of these DSSCs. It can be seen as the wavelength increases from 440-500 nm, the IPCE steadily rises. This rise in IPCE can be attributed to the increased light absorption of N719 dye within the same range of wavelength as shown in Figure 4.6. The IPCE increases up to the maximum value at the wavelength of 525 nm, corresponding to the maximum absorbance of the N719 dye. For a further increase in wavelength, the IPCE drops sharply and follows the same trend as the N719 absorption curves (Figure 4.6). Additionally, the nanocrystalline TiO_2 based devices have a marginally higher maximum IPCE value of 68% compared to $TiCl_4$ treated SnO_2 nanofibers (62%) and SnO_2/P25-TiO_2 (63%). Although SnO_2 and their composite based DSSCs have relatively lower IPCE values, given the thin device structure, they are proved to possess a remarkable light absorption capability.

Table 4.1. Comparison of performance parameters of $TiCl_4$ treated SnO_2 nanofiber, SnO_2/P25-TiO_2, and nanocrystalline TiO_2 based DSSCs.

Device	Thickness (μm)	V_{oc} (V)	J_{sc} $mAcm^{-2}$	FF	η (%)	L (μm)
SnO_2 nanofiber	~ 6.5-7	0.75	-10.75	0.50	4.06	15.67±0.58
SnO_2/P25-TiO_2	~ 6.5-7	0.80	-11.97	0.60	5.72	19.98±0.74
Nanocrystalline TiO_2	14	0.79	-12.78	0.71	7.12	52.70±1.82

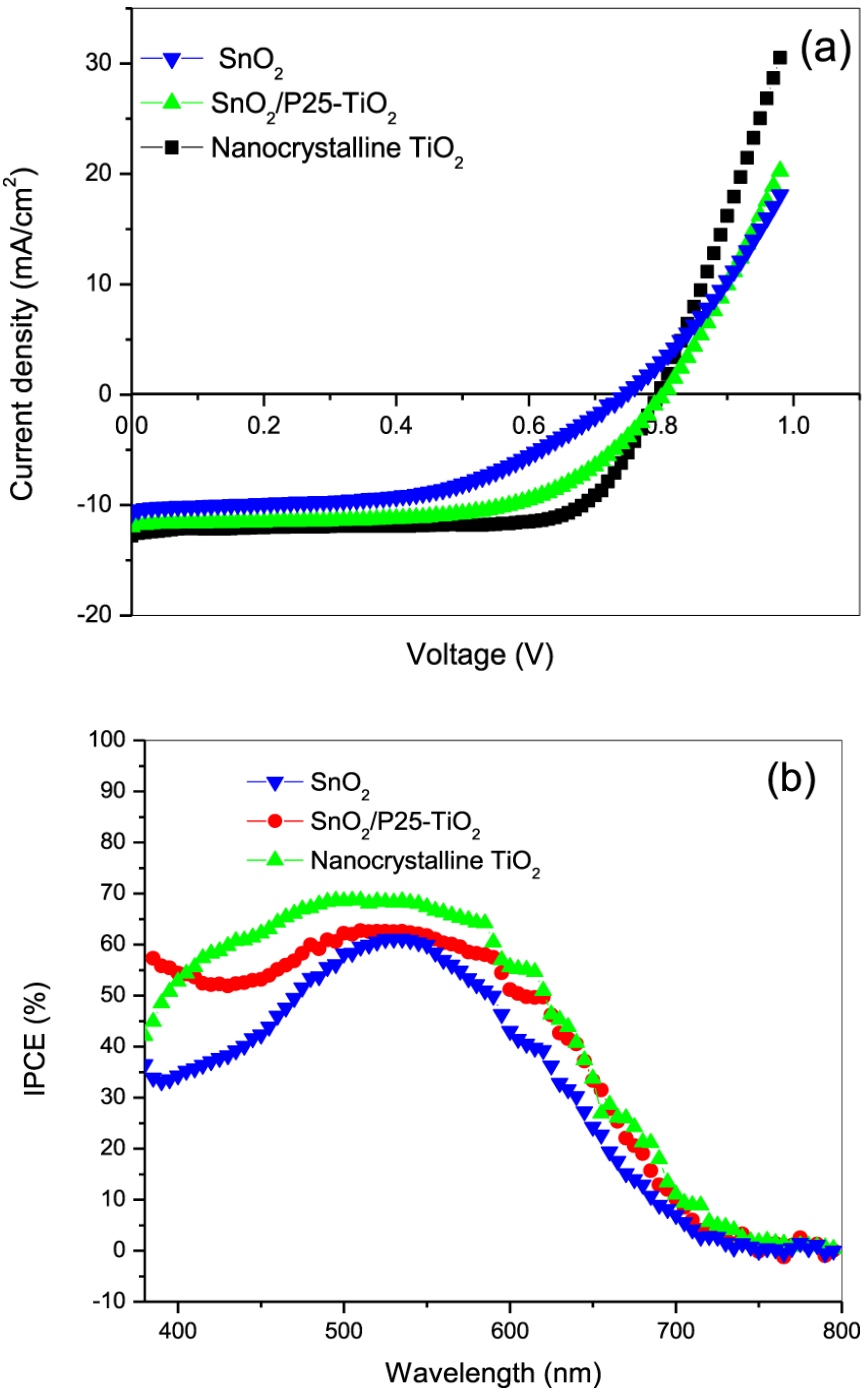

Figure 4.5. (a) Current density-voltage (J-V) curves of DSSCs made from $TiCl_4$ treated SnO_2 nanofibers, SnO_2/P25-TiO_2, and nanocrystalline TiO_2 under AM 1.5 illumination at the light intensity of 100 mW/cm^2. (b) IPCE spectral action responses of the DSSCs based on $TiCl_4$ treated SnO_2 nanofiber, SnO_2/P25-TiO_2, and nanocrystalline TiO_2 photoanodes.

4.3.3. UV-Vis absorbance spectrum of hollow SnO_2 nanofiber based photoanode

Figure 4.6 shows the UV-Vis normalized absorbance spectra from the solutions of N719 dyes that were desorbed from $TiCl_4$ treated SnO_2 nanofiber, SnO_2/P25-TiO_2, and nanocrystalline TiO_2 photoanodes. Among three samples, nanocrystalline TiO_2 has the highest light absorption over the whole visible spectrum. This observation is in an agreement with the fact that the light absorbance (A) is proportional to the dye uptake (C_{dye}) as described in Equation 4.1. Hence, the highest absorbance of nanocrystalline TiO_2 is resulted from the high specific surface area of ~100 m^2/g, compared to SnO_2 nanofibers (35.8 m^2/g). The SnO_2/P25-TiO_2 composite has a higher light absorption compared to SnO_2 nanofibers, which may be due to the increase in surface area because of the addition of P25-TiO_2 into the network of SnO_2 nanofibers.

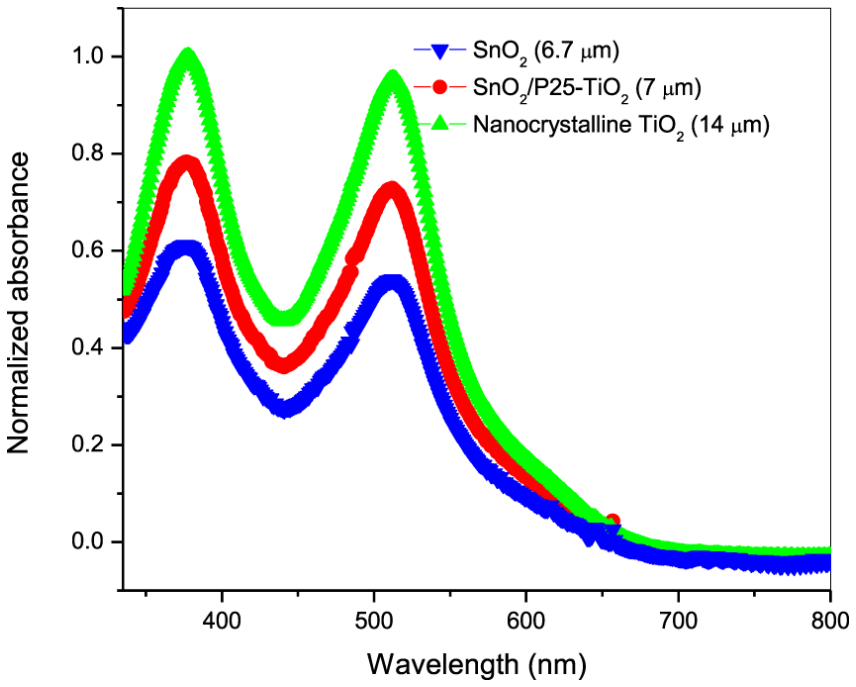

Figure 4.6. UV-Vis normalized absorbance spectra from the solutions of N719 dyes that were desorbed from $TiCl_4$ treated SnO_2 nanofiber, SnO_2/P25-TiO_2, and nanocrystalline TiO_2 photoanodes used in the DSSCs.

4.3.4. Photovoltage and photocurrent decay

To understand the improvement in FF after addition of P25-TiO_2 in SnO_2 nanofibers, the charge transport in the bulk of the photoanode films was studied using TPC measurement. Figure 4.7(a) shows the normalized TPC decay of $TiCl_4$ treated SnO_2 nanofiber, SnO_2/P25-TiO_2, and nanocrystalline TiO_2 based DSSCs. The electron transport lifetime (τ) obtained from these exponentially decaying curves were 4.4 ms for SnO_2 and 1.31 ms for SnO_2/P25-TiO_2. This shows that the bulk of SnO_2/P25-TiO_2 offers less resistance to the electron flow within the film. The reason for faster charge transport time in P25-TiO_2 incorporated SnO_2 may be due to the presence of TiO_2 nanoparticles between the gaps of nanofibers resulting in a smooth flow of electrons in the bulk. The above-mentioned electron transport lifetime in SnO_2 and SnO_2/P25-TiO_2 justifies the higher value of FF in SnO_2/P25-TiO_2 (0.60) as compared to SnO_2 (0.50). Moreover, the charge transport lifetime in nanocrystalline TiO_2 based DSSCs was found to be lowest (0.58 ms), suggesting the lowest bulk resistance in TiO_2 film. This lowest bulk resistance is reflected in the highest attainable FF (0.71) as compared to SnO_2 and SnO_2/P25-TiO_2 based DSSCs.

The normalized TPV decay of $TiCl_4$ treated SnO_2 nanofiber, SnO_2/P25-TiO_2, and nanocrystalline TiO_2 based DSSCs are shown in Figure 4.7(b). The electron recombination lifetime of SnO_2 nanofiber, SnO_2/P25-TiO_2, and nanocrystalline TiO_2 based DSSCs were found to be 55.77, 26.97, and 18 ms, respectively. Based on the measured electron recombination and transport lifetime, the diffusion length was found to be 15.67, 19.98, and 52.70 μm for SnO_2 nanofiber, SnO_2/P25-TiO_2, and nanocrystalline TiO_2-based DSSCs, respectively. The highest diffusion length observed in nanocrystalline TiO_2-based DSSCs indicates that the electron recombination process is much slower as compared to electron transport in the TiO_2 photoanodes, which justifies the high values of V_{oc} above 0.75 V (Table 4.1). Yet, the low diffusion length in

both SnO_2 nanofibers (15.67 μm) and SnO_2/P25-TiO_2 composite (19.98 μm), may lead to a low attainable V_{oc} in SnO_2 nanofiber based DSSCs. It should be pointed out, for each of these devices, an energy barrier of ~300 meV was created by $TiCl_4$ post-treatment, which could effectively prevent electron transfer from the active layer back to the electrolyte.

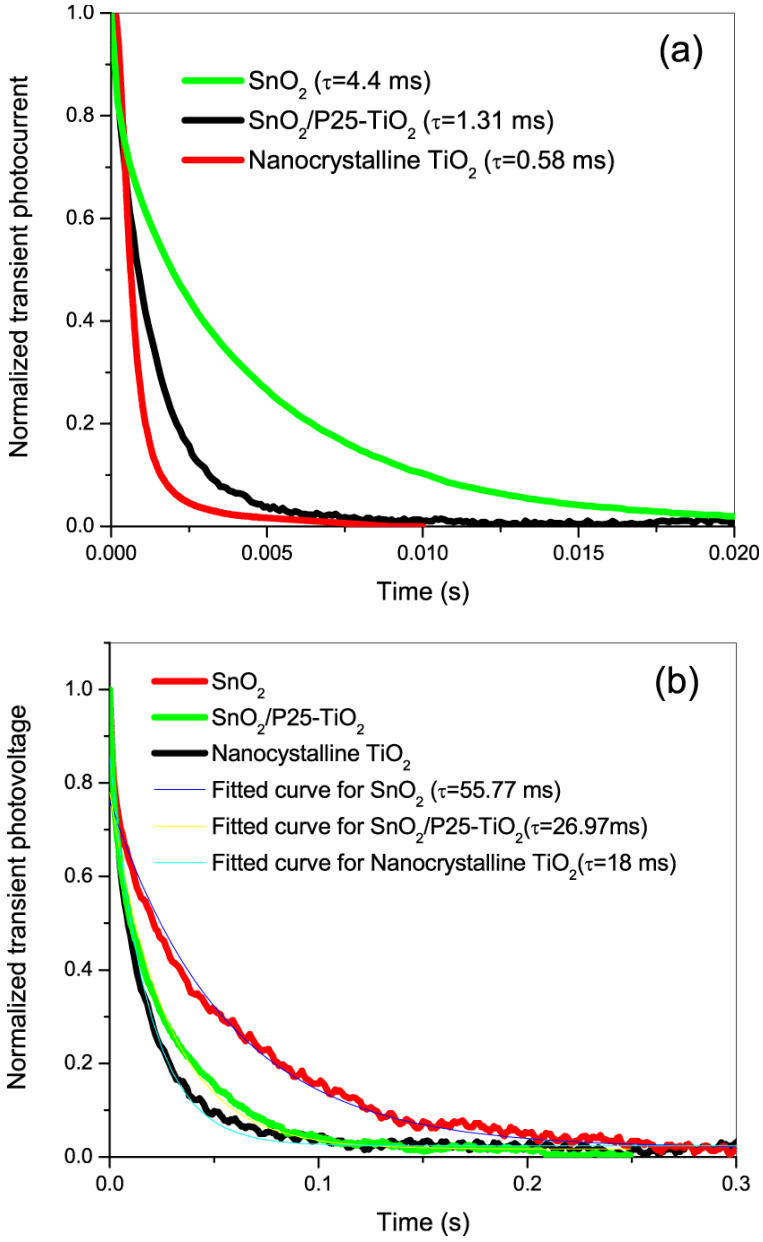

Figure 4.7. Normalized transient (a) photocurrent and (b) photovoltage decay of $TiCl_4$ treated SnO_2 nanofiber, SnO_2/P25-TiO_2, and nanocrystalline TiO_2 based DSSCs.

4.3.5. EIS characterization

EIS analysis was performed to examine the interfacial charge transfer. Figure 4.8(a) shows the Nyquist plots of a complete cell using $TiCl_4$ treated SnO_2 nanofibers, SnO_2/P25-TiO_2, and nanocrystalline TiO_2 as photoanodes. Using a small AC signal model, any interface can be represented by a resistance and a capacitor in parallel combination. Figure 4.8(b) shows the equivalent circuit diagram used to fit the impedance spectra. The equivalent circuit was fitted to extract the parameters from two semicircles observed at high-frequency region and intermediate-frequency region. R_S represents the series resistance of the electrodes, R_{CT} represents the charge transfer resistance at the electrolyte/CE interface, and R_{CR} represents the back charge transfer from photoanode to electrolyte [165]. The high-frequency arc represents the interfacial charge transfer at electrolyte/Pt interface and the intermediate-frequency arc represents the back charge transfer from photoanode to I_3^-/I^- electrolyte. The low-frequency arc represents the finite Warburg impedance of triiodide in electrolyte [165]. Since the I_3^-/I^- electrolyte was used in all devices, the arcs representing the finite Warburg impedance of triiodide in electrolyte were almost identical.

Fitted parameters obtained from the Nyquist plots (first two arcs) are summarized in Table 4.2. Since Pt is used as CE in all three different cells and the electrolyte is the same, the R_{CT} is found to be almost equal1 (12-13 Ω). The charge recombination resistances (R_{CR}) in SnO_2 nanofibers, SnO_2/P25-TiO_2, and nanocrystalline TiO_2 were found to be 188.4, 163.4, and 121 Ω, respectively. In general, it is considered that the higher the recombination resistance, the greater the V_{oc}. Based on this fact, SnO_2 nanofibers are expected to have the highest V_{oc}. However, the longer charge transport time (TPC analysis) may increase the probability of recombination, which would have a negative impact on V_{oc}. All the experimental results reported in this chapter have been published in *IEEE Transactions on Electron Devices* in 2015 [18].

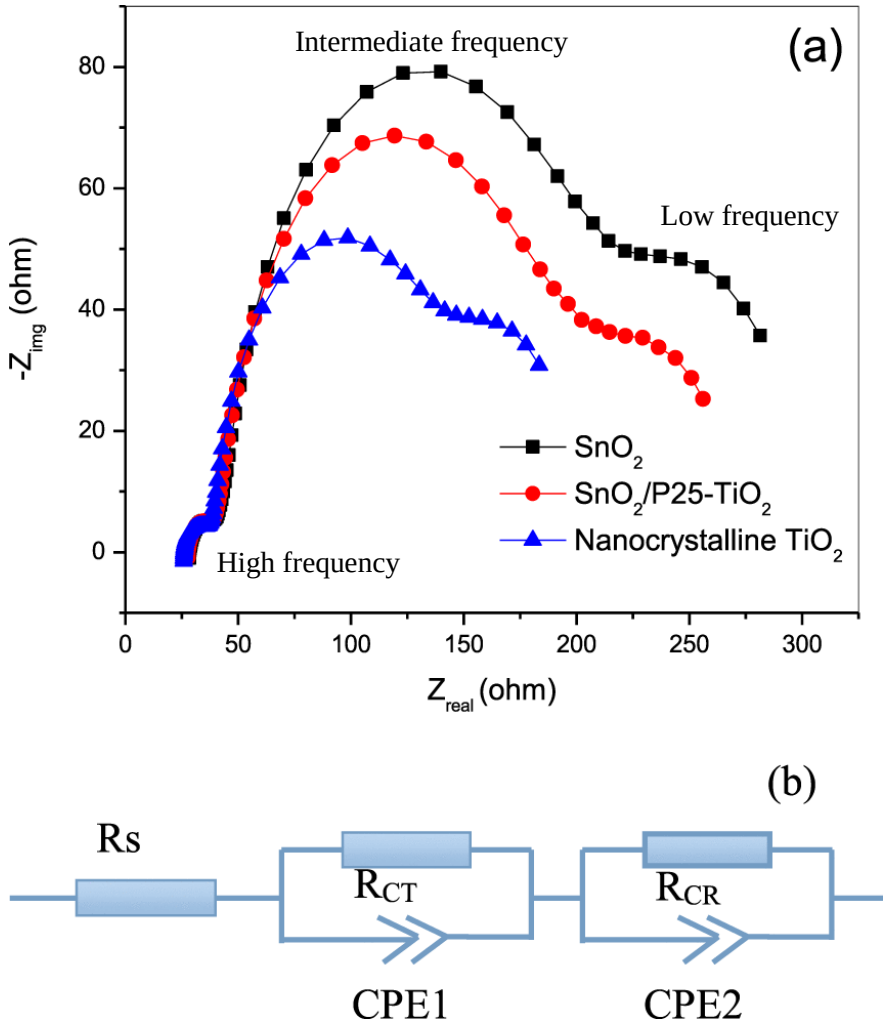

Figure 4.8. (a) Nyquist plots of $TiCl_4$ treated SnO_2 nanofiber, SnO_2/P25-TiO_2, and nanocrystalline TiO_2 based DSSCs measured at a DC bias voltage (V_{oc}) under dark conditions and from 0.1 Hz to 100 KHz with an amplitude of 10 mV. (b) Equivalent circuit of a full DSSC for EIS measurement. R_S: series resistance at the electrodes. CPE: constant phase element. R_{CT}: charge transfer resistance at electrolyte/CE interface. R_{CR}: charge recombination resistance at anode/electrolyte interface.

Table 4.2. Fitted parameters extracted from Nyquist plots of $TiCl_4$ treated SnO_2 nanofiber, SnO_2/P25-TiO_2, and nanocrystalline TiO_2 based DSSCs.

Device	R_S (Ω)	R_{CT} (Ω)	R_{CR} (Ω)
SnO_2 nanofiber	28.43	13.25	188.4
SnO_2/P25-TiO_2	27.85	12.4	163.4
Nanocrystalline TiO_2	25.99	12.05	121

4.4. Summary

In this study, hollow SnO_2 nanofibers and their composites (SnO_2/P25-TiO_2) were fabricated and investigated for use as a perspective electrode material in dye-sensitized solar cells. The microstructure of the SnO_2 nanofibers was investigated using SEM, TEM, and XRD. The SEM and TEM images show that the SnO_2 nanofibers have a hollow structure with dense shells and are comprised of numerous nanograins with a particle size of approximately 17 nm. The formation of the hollow nanofibers with nanograins on the shell can be attributed to the Kirkendall effect and surface diffusion during the calcination process at elevated temperature (600 °C). The XRD patterns indicate a high purity of SnO_2 nanofibers in a tetragonal rutile crystal structure. It is found that incorporation of TiO_2 nanoparticles into hollow SnO_2 nanofibers could enhance the power conversion efficiency (η) from 4.06% to 5.72% under a light intensity of 100 mW/cm^2. This enhancement of efficiency is a result of the increase in current density (J_{sc}) and the improvement in fill factor (FF). The increase in J_{sc} can be mainly attributed to the higher dye loading as confirmed by both UV-Vis absorption spectra and IPCE spectra, while the improvement in FF is due to the faster charge transport as evidenced by the electron lifetimes derived from TPC and TPV analyses. In addition, hollow SnO_2 nanofibers with half the thickness (~6.5-7 μm) of nanocrystalline TiO_2 (~14 μm) have been demonstrated as an efficient novel photoanode for DSSCs. This could be a new guidance for the development of inexpensive DSSCs with a thinner film of photoanode and an increased amount of dye via the incorporation of TiO_2 nanoparticles.

5. ACTIVATED GRAPHENE NANOPLATELETS AS A COST-EFFECTIVE COUNTER ELECTRODE FOR DYE-SENSITIZED SOLAR CELLS

5.1. Introduction

Similar to SnO_2 nanofibers, activated graphene nanoplatelets (aGNPs) are also inexpensive and possess desired properties such as high transparency, good electrochemical activity, and superior conductivity. Therefore, aGNPs can potentially be used as a low-cost, effective electrode material to replace expensive conventional Pt electrode. In the past, both activated carbon and GNPs have been popularly used as porous counter electrode (CE) materials in DSSCs. In this study, a new method has been attempted by activating GNPs. The new aGNPs were prepared based on the recently reported hydrothermal method [166]. The process included treating graphene nanoplatelets in potassium hydroxide (KOH) solution, followed by a chemical activation process. This chapter presents the details of aGNP preparation, structural characterization, and its electrochemical performance. The resulting aGNP nanoplatelets were used as a substitute for Pt electrode. The electrochemical performance of aGNP based CEs was characterized using cyclic voltammetry (CV) and electrochemical impedance spectroscopy (EIS). In general, the CV curves exhibit a high redox peak current, indicating a large electrode surface area and an excellent reversibility of the redox reactions. The electrochemical parameters derived from EIS show that aGNP based CEs have a low charge transfer resistance of 1.56 Ωcm^2, which is comparable to the literature reported values for Pt (0.5-1.8 Ωcm^2). This fact ensures that, aGNPs exhibit a fast charge transfer at the interface between electrolyte and counter electrode. The above-mentioned electrochemical performances are related to the unique microstructure of aGNP nanoplatelets. The

morphology and structure of aGNP electrodes were investigated using SEM, XRD, and Raman spectrometry. The porous morphology of aGNP films aids an increase in surface area of counter electrodes, and the presence of hydroxyl groups serves as additional active sites, which contributes to an enhanced electrocatalytic activity.

5.2. Experimental Methods

5.2.1. Preparation of activated graphene nanoplatelets

Graphene nanoplatelets (GNPs) purchased from Strem Chemicals, Inc. (MA, USA), were utilized for our study. These GNPs consisted of short stacks of platelet-shaped graphene sheets with an average thickness (5-10 nm) and width (25 μm). As per the procedure reported by Zhu et al. [166], graphene nanoplatelets were activated with KOH solution. The nanoplatelets (400 mg) were initially dispersed in 20 ml KOH (7 M) aqueous solution, which was soaked for 24 h under static ambient conditions. The mixture was dried and then annealed at 800 °C in a nitrogen atmosphere for 1 h. After cooling down to the ambient temperature, the product was repeatedly washed with de-ionized (DI) water until its pH became neutral. Finally, the resulting product was dried and was ready to be used.

5.2.2. Microstructure characterization

The morphology of the final product was studied via field emission scanning electron microscopy (FESEM, JSM-7401F). The chemical composition of aGNP was analyzed using a Renishaw RM2000 Raman spectrometer with 514.5 nm wavelength argon laser beam. The sampling spot diameter was 5 μm in diameter, and the integration time was 30 s. Powder XRD pattern was acquired on a Shimadzu XRD-6000 diffractometer (40 kV, 30 mA) at 6 deg per min from 10° to 70°.

The porous structure of aGNP samples was characterized using a Quadrasorb SI analyzer. First, the GNP and aGNP samples were degassed at 423 K for 10 h in vacuum, and nitrogen adsorption/desorption isotherms were obtained at 77 K. These measured isotherms were utilized to determine surface areas of each sample based on the BET method. The pore size distribution was derived from on desorption branch using the BJH method. The total pore volume (V_{total}) of each sample were also quantified using the generated isotherms reflecting the adsorption/desorption of nitrogen at a relative pressure (P/P_o) of 0.985. Additionally, the micropore surface area (S_{micro}) and pore volume (V_{micro}) were calculated using the quenched-solid density function theory (QSDFT).

5.2.3. Fabrication of aGNP based counter electrodes

The activated graphene nanoplatelets (10 mg) were added to 4 ml ethanol, followed by 30 min sonication. The resulting suspension was spray coated onto a cleaned FTO-glass substrate. The coated substrate was then annealed at 400 °C for 30 min in air. It should be noted that the thickness of the aGNP films is an important factor that influences the electrical conductivity and electrocatalytic activity of counter electrodes. The coating thickness can be controlled by adjusting the spraying duration, and in this study the thickness was in a range between 20 and 70 µm. For comparison, a Pt reference counter electrode with a thickness of ~40 nm was prepared by spin coating a Pt precursor solution (0.02 M $H_2PtCl_6 \cdot 6H_20$ in anhydrous ethanol) at 3,000 rpm for 20 s, and was then annealed at 400 °C for 15 min in air.

5.2.4. Device characterization

The prepared aGNP based CEs were assembled with standard TiO_2 photoanodes into DSSCs following the same procedure detailed in Section 4.2.3. The current density-voltage characteristics of fabricated DSSCs were obtained for an active area of 0.125 cm^2 (unmasked)

under an AM 1.5 illumination with an intensity of 91.5 mW/cm^2. The "active area" refers to an area of the printed dye-sensitized TiO_2 layer. A solar light simulator (Newport 67005) with an AM 1.5 filter was used to simulate sunlight, and an NREL certificated reference cell was used to calibrate the light source. Cyclic voltammetry (CV) measurements were performed using a Pt wire as the counter electrode, an Ag/AgCl as the reference electrode, and an aGNP or Pt coated FTO as the working electrode at a potential scan rate of 50 mVs^{-1}. Supporting electrolyte was prepared using acetonitrile solution containing 10 mM LiI and 0.5 mM I_2 as well as 0.1 M tetra-n-butylammonium tetrafluoroborate.

Electrochemical impedance spectroscopy (EIS) measurements were performed by using Ametek VERSASTAT3-200 Potentiostat incorporated with a frequency response analyzer (FRA). The AC signal was set to be 10 mV in the frequency range from 0.1 to 100 KHz. A DC bias voltage of 0.8 V (~V_{oc}) was applied under dark conditions. This experiment was carried out using a symmetrical dummy cell which had two identical CEs with a thin layer of electrolyte solution (δ) as shown in Figure 5.1. This symmetrical structure was designed to eliminate the influence of TiO_2 photoanode, and hence simplified the interpretation of experimental data.

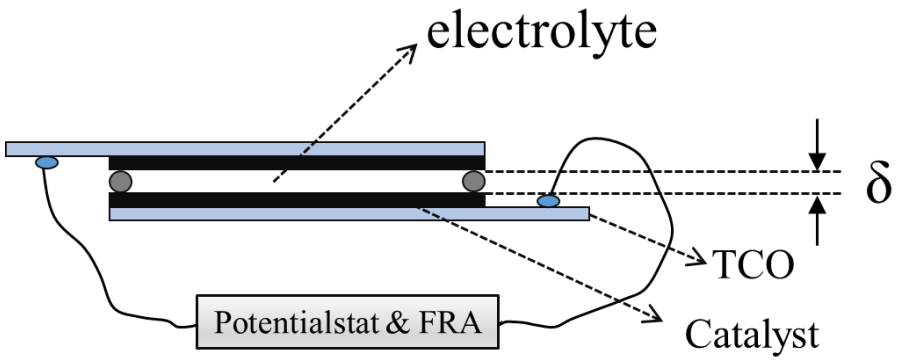

Figure 5.1. Schematic of a symmetrical dummy cell.

5.3. Results and Discussion

5.3.1. Morphology and structure characterization

As aforementioned, Zhu et al. [166] previously used KOH activation to increase the porosity in nanostructured graphene materials[166][166][166][165][164][163][162]. The mechanism of KOH activation proceeds as $6KOH + C \leftrightarrow 2K + 3H_2 + 2K_2CO_3$, followed by decomposition of K_2CO_3 and/or reaction of $K/K_2CO_3/CO_2$ with carbon [167]. Figure 5.2 shows different microstructures of pristine GNPs and KOH-activated GNPs. The dark region in Figure 5.2(a) indicates that the pristine GNPs comprise a layer-stacked compact structure, reflecting a significant degree of aggregation. The formation of layer-stacked microstructure is mainly due to the strong π-π interaction between graphene nanoplatelets. Comparatively, after activating GNPs with KOH solution, the nanoplatelets become warped. Hence, as shown in Figure 5.2(b), the bright zones (white regions) indicate an increase in the surface edge of aGNPs. This is because during activation, the gaseous products (e.g. CO_2) created voids and pores between GNP nanoplatelets. Hence, the aGNP film has a rough and porous morphology, which includes both micro- and mesopores.

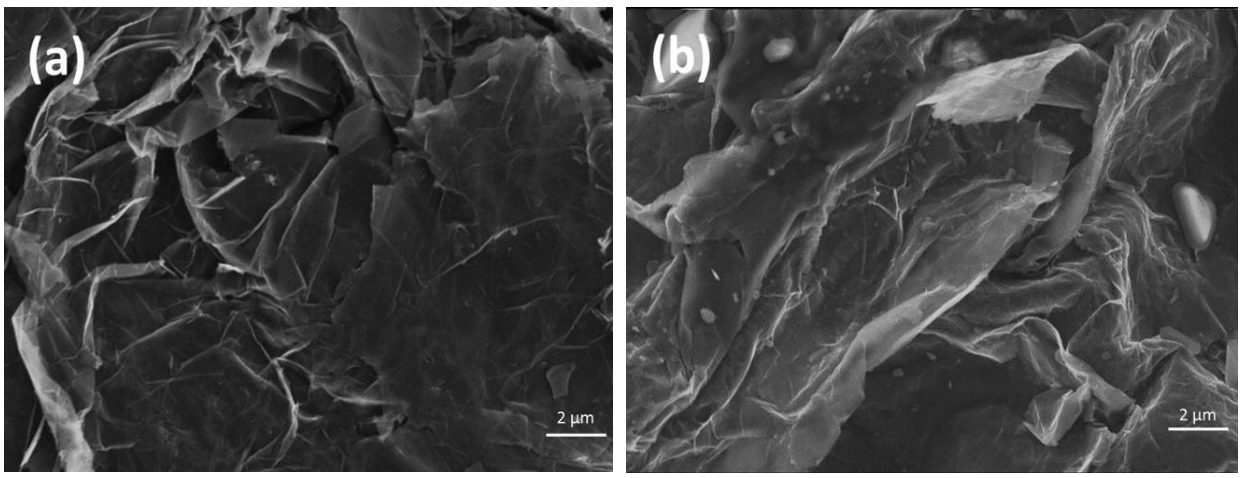

Figure 5.2. FESEM images of the pristine GNPs and activated GNPs.

Nitrogen adsorption was used to analyze the pore structures of the pristine and activated GNPs. As shown in Figure 5.3(a), the nitrogen adsorption-desorption isotherms of these two samples exhibit similar type-IV curves with a clear H3-type hysteresis loop. Capillary condensation in a wide range of relative pressure (0.7-1.0) indicates the existence of mesopores [168]. Similarly, the steep increase of nitrogen uptake at low relative pressure reflects the formation of micropores [169]. Based on adsorption branch of isotherm, the pore size distribution shown in Figure 5.3(b) was calculated using quenched solid density functional theory (QSDFT). The calculated results show that there exist nanopores with an average size of ~3 nm in the activated GNP sample. The specific surface area and pore volume of samples are summarized in Table 5.1. The pristine GNPs possess a BET surface area of 24 m^2/g and a total pore volume of 0.034 cm^3/g, whereas the activated GNPs possess an increased BET surface area of 91 m^2/g and a total pore volume of 0.19 cm^3/g. The significant increase in both surface area and pore volume proves KOH an effective chemical activating agent for graphene materials. It should be pointed out that the BET surface areas of these two samples are significantly lower than the theoretical limit of graphene (2630 m^2/g). Such low specific areas might be caused by the stacked layers and incomplete exfoliation of thin nanoplatelets.

Table 5.1. Porosity parameters of the GNPs and aGNPs.

Samples	S_{BET}[a] (m^2/g)	S_{micro}[b] (m^2/g)	V_{total}[c] (cm^3/g)	V_{micro}[d] (cm^3/g)
GNP	24	3.3	0.034	0.003
aGNP	91	32	0.19	0.03

[a]BET specific surface area. [b]Micropore (<2 nm) surface area calculated by DFT method.
[c]Total pore volume at $P/P_0 = 0.995$. [d]Micropore (< 2 nm) volume calculated by DFT method

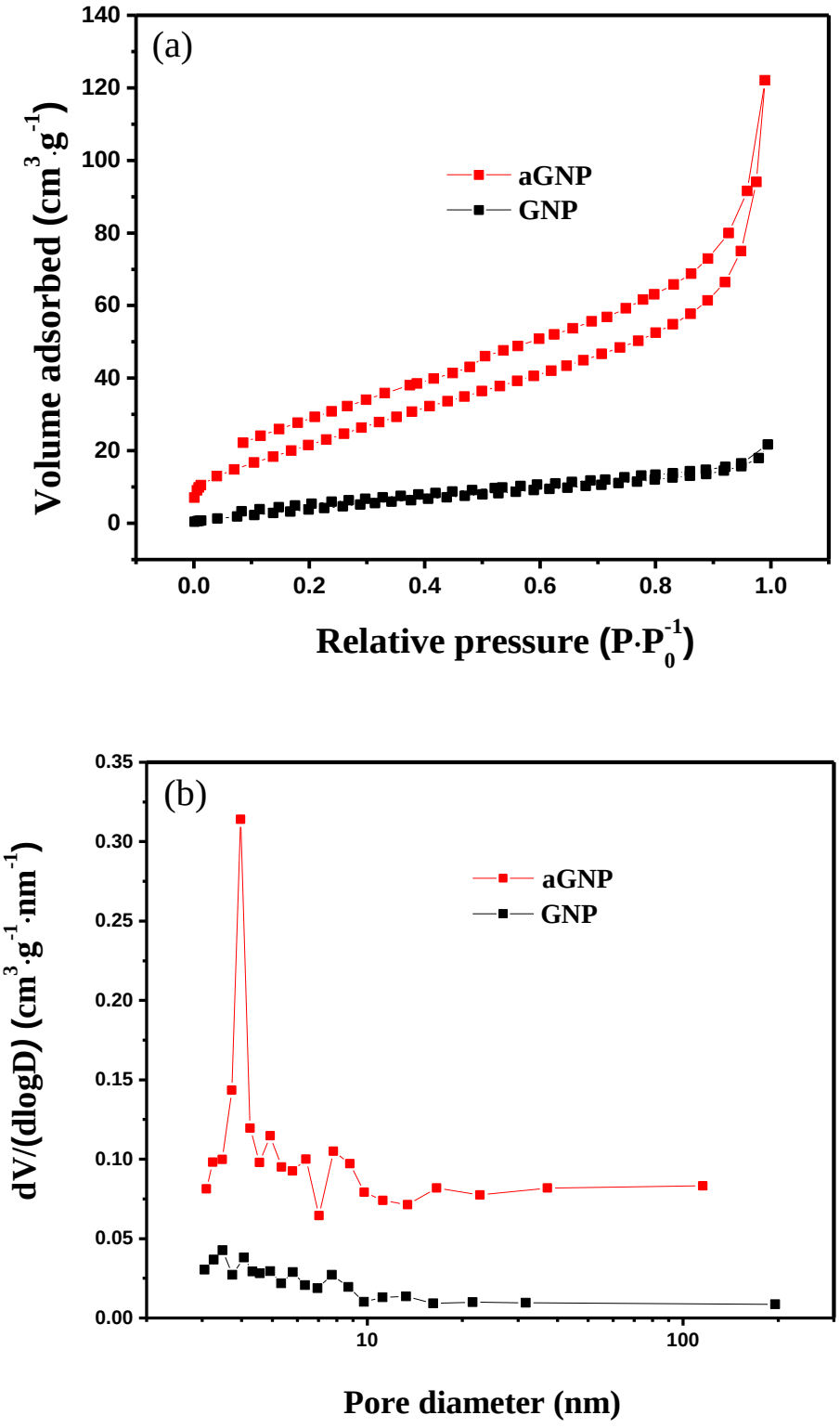

Figure 5.3. (a) Nitrogen adsorption-desorption isotherms; (b) the Barrett-Joyner-Halenda (BJH) pore size distributions of the GNPs and aGNPs.

Figure 5.4(a) shows the XRD patterns for both GNPs and aGNPs samples. It can be clearly seen that the both samples exhibit an intense diffraction peak centered at 26.5°. The sharp diffraction peak of GNP sample corresponds to the (0 0 2) hexagonal graphite plane composed of well-ordered graphene with an interlayer spacing of 3.35 Å [170]. As can been seen, there exist no obvious impurity peaks (e.g., graphite and graphite oxide), indicating a high purity of the graphene nanoplatelets. The sharp peak centered at 26.5° becomes broad after KOH activation. This broad peak of aGNP sample can be attributed to the transition from the stacked platelet configuration to a disordered microstructure, which further contributes to a substantial increase in both porosity and surface area. In addition, a diffraction peak observed at 12-13° suggests the formation of graphene oxide during the activation, and the other two peaks at 30° and 33° correspond to the existence of K_2CO_3 residue [171].

Raman spectroscopy is yet another effective tool to investigate the structural variations that occur in graphene materials. Figure 5.4(b) shows the Raman spectra of both GNPs and aGNPs samples. Characteristic peaks observed at G (1580 cm^{-1}) and 2D (2690 cm^{-1}) correspond to the two-dimensional planar structure of graphene materials. The D band at ~1325 cm^{-1} formed in aGNP sample confirms that KOH activation successfully converts the stacked layers of GNPs to a more disordered microstructure. Moreover, the aGNP sample shows a relatively strong D-band at 3250 cm^{-1}, which indicates the existence of hydroxyl groups in the aGNPs [172].

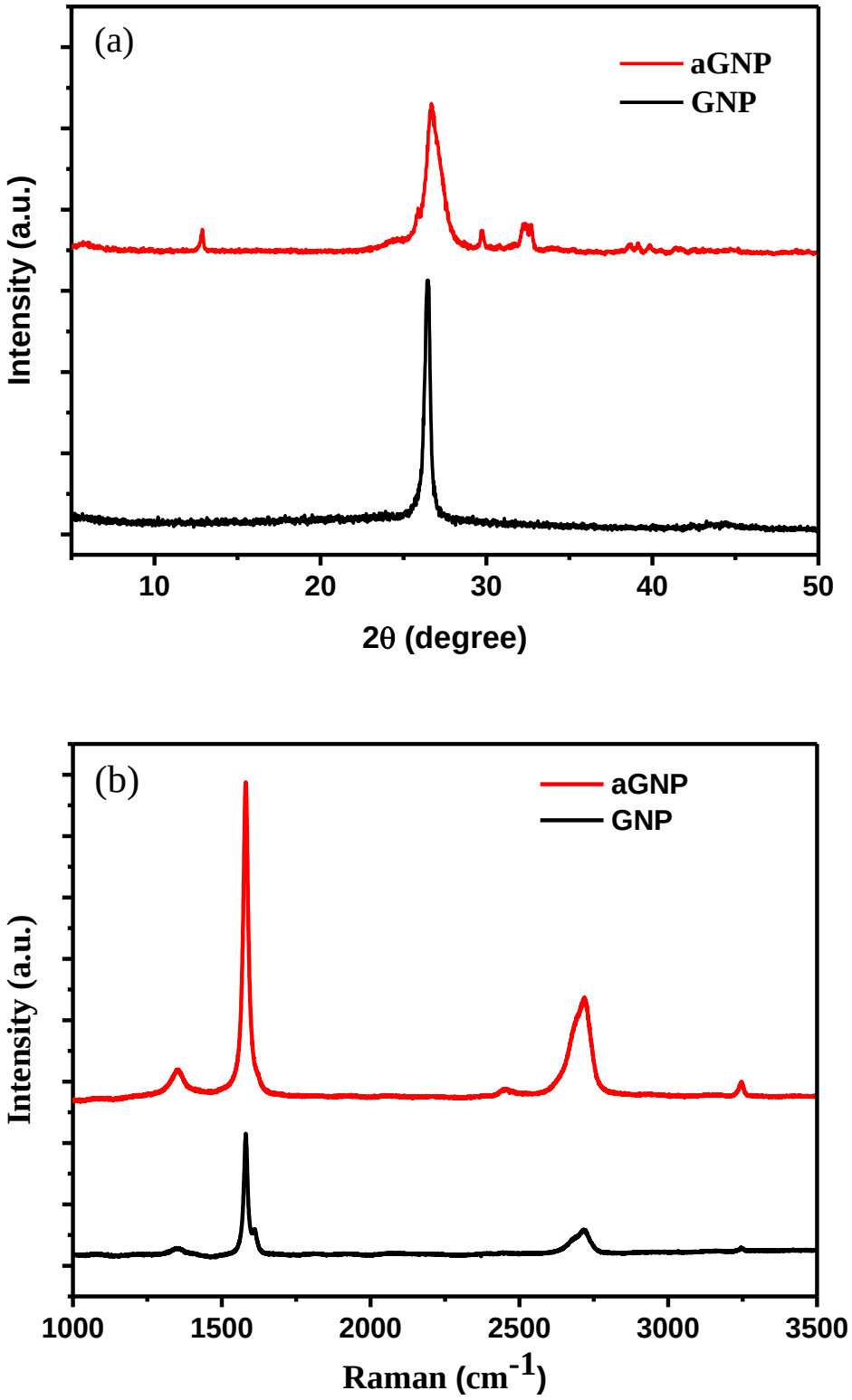

Figure 5.4. (a) XRD patterns for GNPs and aGNPs; (b) Raman spectra of GNPs and aGNPs.

5.3.2. Photovoltaic performance of aGNP based DSSC

The performance of DSSCs was measured under standard AM 1.5 simulated sunlight at an intensity of 91.5 $mWcm^{-2}$. Figure 5.5(a) presents J-V characteristics of DSSCs using aGNP and Pt based counter electrodes. The aGNP CEs with a thickness of 70 μm achieved an overall light-to-electric energy conversion efficiency of 7.7%, which is comparable to Pt (8.1%). The photovoltaic parameters of aGNPs and Pt based devices are listed in Table 5.2. The aGNP based DSSCs outperformed the Pt counterpart particularly in terms of short-circuit current density. This is an obvious impact due to the efficient contact between electrolyte and aGNP electrode. Such remarkably high short-circuit current observed in this study may be partly attributed to the unmasked testing conditions [173]. Snaith [174] reported that unmasked cells could result in an efficiency overestimation of a factor around 1.5.

The slope of J-V curves, shown in Figure 5.5(a), indirectly correlates with the fill factor. The aGNP based DSSCs have lower FF values compared to platinum based devices. This might be due to the higher series resistance (2.68 Ω) in an aGNP device compared to the Pt (2.39 Ω). In addition, the film thickness influences the fill factor as well. As the film thickness decreases, both J_{sc} and FF decrease. For example, aGNP sample with 18.67 μm thick could attain a maximum J_{sc} of 13.50 mA/cm^2. This may be due to the fact that the thin counter electrode could not provide sufficient catalytic activity to efficiently restore iodide (I^-) from triiodide (I_3^-). Hence, the photoinduced electrons tend to recombine with I_3^- and consequently form dark current, which lowers both J_{sc} and V_{oc}, and also is reflected in the increased electron recombination rate. The adversary effect of increased recombination rate on J_{sc} and V_{oc} has been quantified in our previous publication [15].

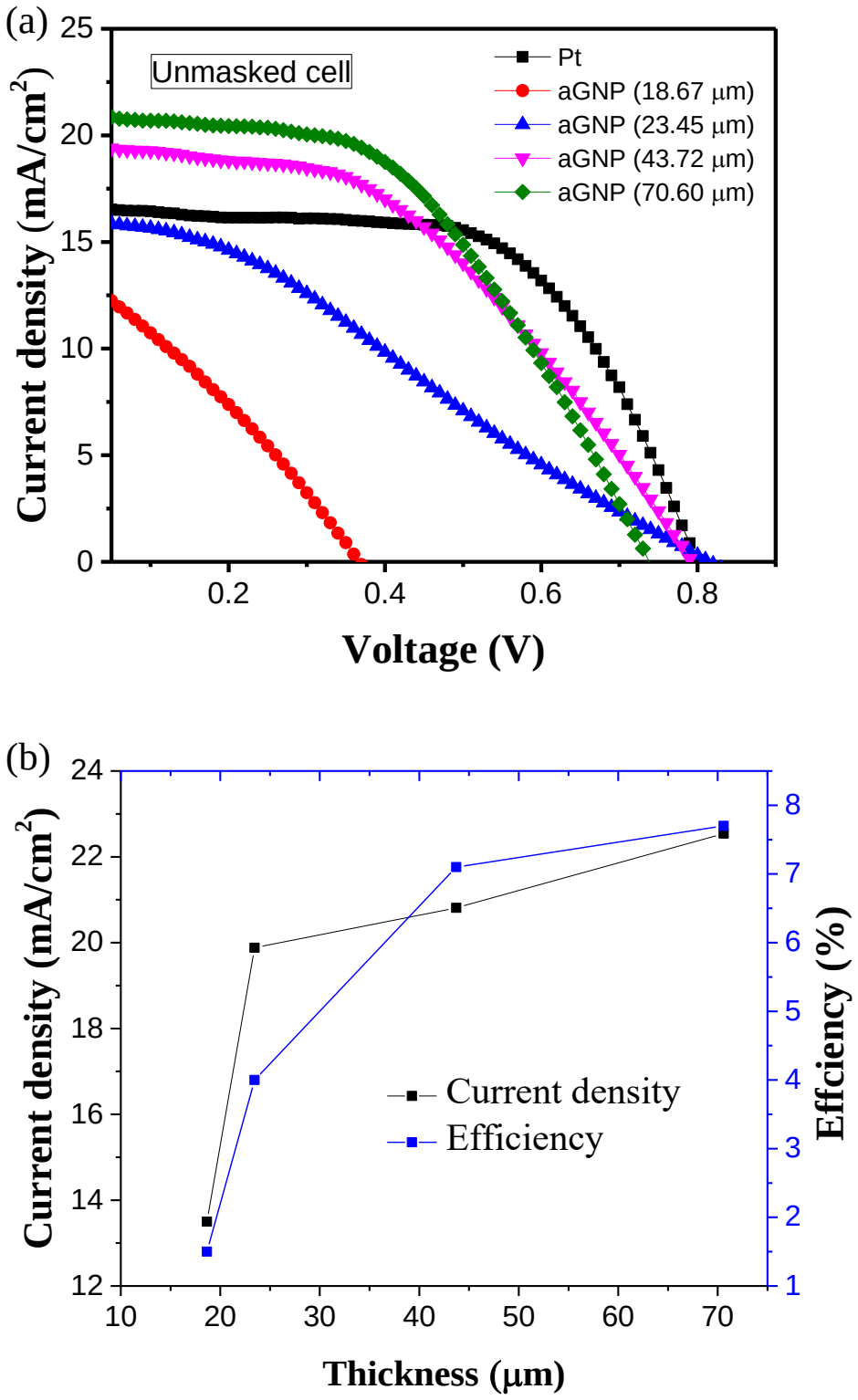

Figure 5.5. (a) Current density-voltage (J-V) characteristics of aGNP and Pt based DSSCs; (b) influence of different aGNP thickness on the overall device efficiency and photocurrent density.

Table 5.2. Comparison of photovoltaic parameters from aGNP and Pt based DSSC devices.

Counter electrode	Thickness (μm)	J_{sc} ($mAcm^{-2}$)	V_{oc} (V)	FF	η (%)
aGNP	18.67	13.50	0.37	0.30	1.5
aGNP	23.45	19.88	0.82	0.24	4.0
aGNP	43.72	20.81	0.79	0.43	7.1
aGNP	70.60	22.54	0.73	0.47	7.7
Pt	NA	17.28	0.8	0.59	8.1

As mentioned earlier, the performance of DSSC is sensitive to the electrode thickness which influences both diffusion resistance and electrochemical activity. In general, as the thickness increases, the surface area (pore formation) increases, which is conducive to electrochemical activity. However, the increase in thickness also leads to higher diffusion resistance. The effect of thickness on device efficiency and photocurrent density is shown in Figure 5.5(b). It can be seen that at a low thickness (18.67 μm), the device has very low efficiency (η) of 1.5% (J_{sc} = 13.50 mA/cm^2; V_{oc} = 0.4 V), which indicates poor electrochemical activity of the counter electrode. When the electrode thickness increases within a range of 20-40 μm, both η and J_{sc} sharply increase. This can be attributed to the increased surface area and micropores, indicating that the electrochemical activity is the dominant factor that dictates the device performance. When the thickness is above 50 μm, η as well as J_{sc} increases only marginally due to the fact that the increased diffusion resistance dominates compared to a marginal increase in the electrochemical activity. For the given study at the thickness of 70.6 μm, the device reaches a maximum efficiency of 7.7% and J_{sc} of 22.54 mA/cm^2. Further increase in thickness does not

improve the device performance because of the increased diffusion resistance, which reflects a reduction in both J_{sc} and FF. The V_{oc} also tends to drop at large thickness due to the depletion of I_3^- ions [13].

5.3.3. Electrochemical characterization

Cyclic voltammetry (CV) is a commonly used tool for studying the electrochemical reaction mechanisms. Figure 5.6 shows CV curves of aGNP and Pt based electrodes. As can been seen, there are two pairs of redox peaks: A_{ox} and A_{red} peaks correspond to the oxidative and reductive reaction of I_2/I_3^- couple, while B_{ox} and B_{red} correspond to the oxidative and reductive reaction of I^-/I_3^- couple. The B_{ox} and B_{red} are of particular importance because the chemical reaction occurs on the counter electrode is the reduction of I_3^- to I^- ($I_3^- + 2e^- \rightarrow 3I^-$). The peak current density and peak potential separation are two major factors that reflect the electrocatalytic properties of the counter electrodes. It can be seen that oxidation and reduction current densities of aGNPs steadily increase as thickness increases. When the thickness is beyond 40 μm, the reduction current of aGNP electrodes becomes comparable to Pt and the oxidation current increases to a larger value. The increased the sample thickness enlarged the surface area, which in turn enhanced the peak currents. This phenomenon is in line with the theory that for reversible electrochemical reactions the peak current is proportional to the electrode surface area [149]. The higher peak currents also demonstrate a faster reduction of triiodide ions by the aGNP counter electrode, which might be due to the high concentration of defects brought by the larger surface area [175].

In addition to the peak current densities, the potential separation of the redox peaks is another important factor that characterizes the electrocatalytic activity of a counter electrode. The electrochemical redox reaction rate is negatively correlated with the peak to peak separation (E_{pp})

[92]. The aGNP and Pt electrodes have comparable E_{pp} values of 50 and 40 mV, respectively. The close value of E_{pp} is an evidence that the aGNP based counter electrode has comparable catalytic activity toward the redox reaction. Therefore, the aGNP nanoplatelets are justifiable as a potential candidate for replacing Pt nanoparticles as catalytic CE materials in DSSCs.

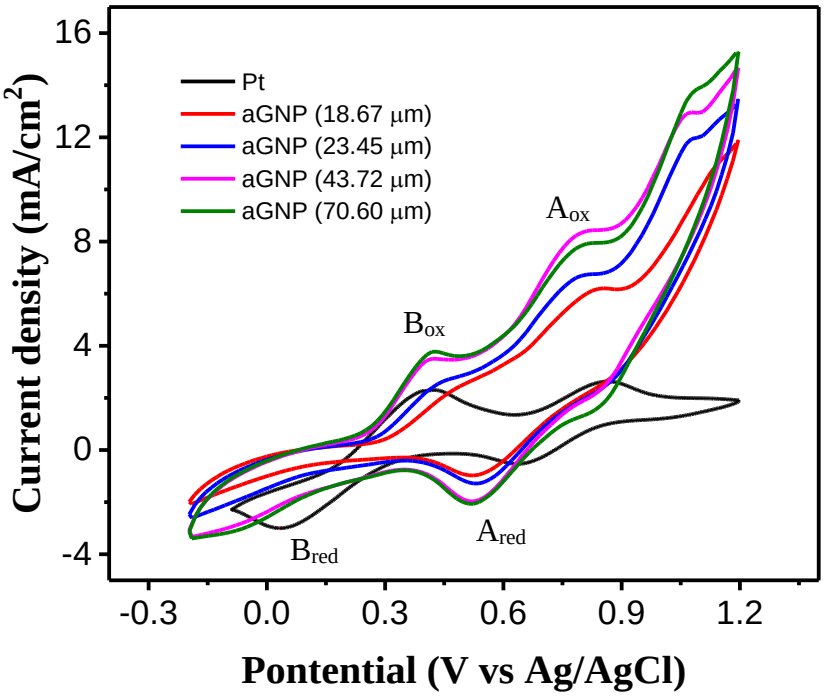

Figure 5.6. Cyclic voltammograms of Pt and aGNP counter electrodes at a scan rate of 50 mV/s in an acetonitrile solution containing 10 mM LiI, 0.5 mM I_2, and 0.1 M tetra-n-butylammonium tetrafluoroborate.

The electrocatalytic performance of the aGNP counter electrodes was further evaluated by electrochemical impedance spectroscopy (EIS). To eliminate the influence of photoanode, symmetrical dummy cells were made with two identical aGNP or Pt based electrodes. Figure 5.7(a) presents the Nyquist plots of electrochemical impedance spectra measured from aGNP and Pt-dummy cells. Z' and Z" are the real and imaginary parts of the impedance, respectively. An equivalent circuit has also been applied to interpret the measured data as shown in Figure 5.7(b), where R_S is the ohmic series resistance, R_{ct} is the charge transfer resistance of the electrode-

electrolyte interface, Z_w is the Nernst diffusion impedance, and CPE is the constant phase element describing deviation from the ideal capacitance due to the electrode roughness [176]. The R_s has two components: one is sheet resistance of two electrodes; the other is the bulk resistance of electrolyte solution. The value of R_s can be determined from the onset of the first semicircle. In addition, the R_{ct} characterizes electron transfer dynamics from electrode to electrolyte solution, and β is a frequency-independent parameter of the CPE.

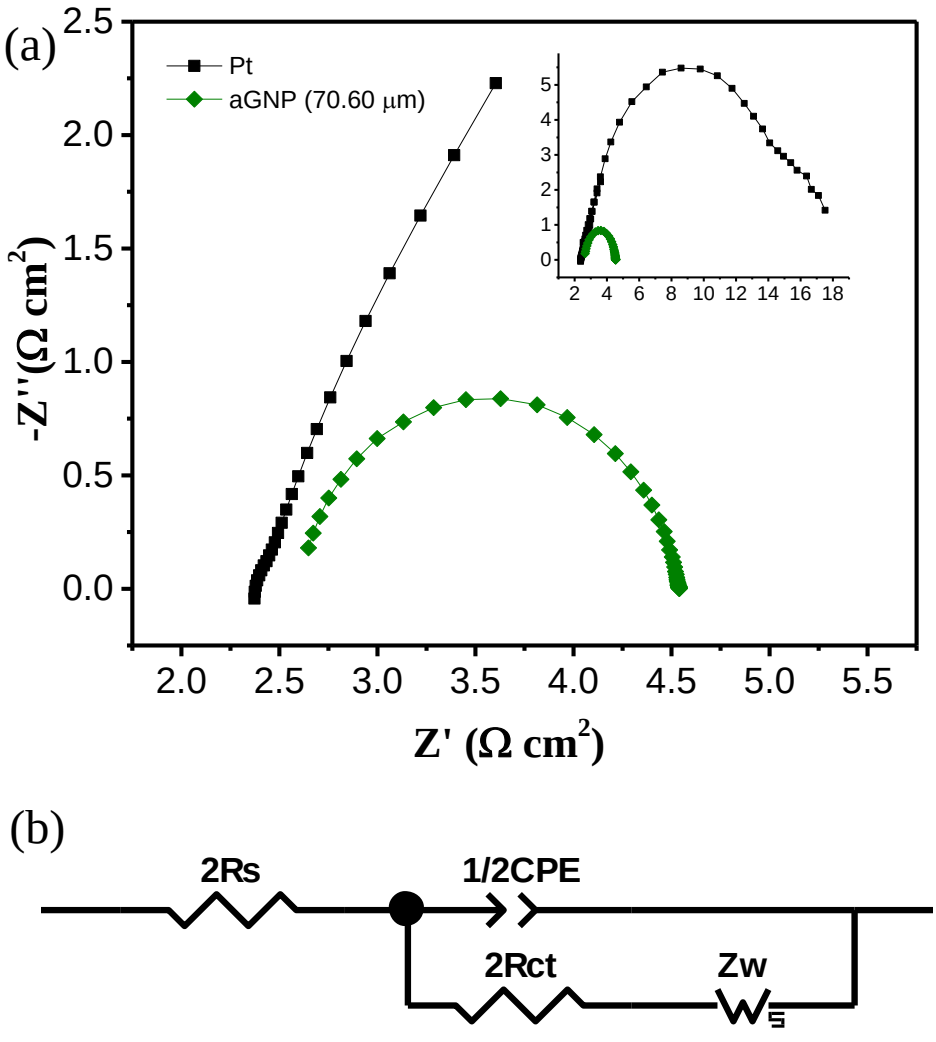

Figure 5.7. (a) Impedance spectra of symmetrical dummy cells from 100 kHz to 0.1 Hz, and (b) equivalent circuit of device cells for fitting impedance spectra.

The electrochemical parameters extracted from the Nyquist plots are listed in Table 5.3. The aGNP electrode has R_s value of 2.68 Ωcm^2, close to Pt (2.39 Ωcm^2), indicating a high intrinsic conductivity of aGNP nanoplatelets. Although the R_{ct} of the aGNP electrode (1.56 Ωcm^2) is marginally higher than Pt (0.55 Ωcm^2), it is comparable to a typical value of Pt (0.5-1.8 Ωcm^2) reported in the literature [177]. The reasonably low R_{ct} of the aGNP electrode indicates a fast charge transfer process occurring at the interface of electrolyte and counter electrode, which in turn contributes to a higher peak current density as observed in CV results. The high electrocatalytic activity of aGNP can be attributed to the increased surface area due to the formation of meso- and nanopores in the activation process. Since the CPE parameter (β) is related to the electrode roughness, a higher β value of aGNPs (0.95) implies that the electrocatalytic activity is correlated with the surface area of counter electrodes.

Table 5.3. Electrochemical parameters of studied aGNP and Pt in symmetrical dummy cells.

Electrode	R_s (Ω cm^2)	R_{ct} (Ω cm^2)	C (F $s^{\beta-1}$ cm^{-2})	β
aGNP	2.68	1.56	8.2×10^{-6}	0.95
Pt	2.39	0.55	6.1×10^{-5}	0.71

In theory, the attainable current density of DSSCs depends on the exchange current density (j_0) at electrodes, which reflects the intrinsic rate of electron transfer at the electrolyte-CE interface. There exists a quantitative relationship between j_0 and R_{ct} as given in [178]:

$$j_0 = \frac{RT}{nFR_{ct}} \tag{5.1}$$

where R is the gas constant, T - operating temperature, n - the number of electrons, and F - the Faraday constant. Figure 5.8 shows the relationship between exchange current density and charge transfer resistance. As can be seen, at room temperature (300 K), for a DSSC to attain j_0 value above 20 mA/cm^2, R_{ct} must be less than 1.5 Ωcm^2. Also, it should be noted that, for any given R_{ct}, higher the operating temperature, higher is the current output. This clearly indicates that the interfacial charge transport resistance is reduced at high temperatures, which partly explains the positive temperature coefficient observed in dye-sensitized solar cells [179]. All the experimental results reported in this chapter have been published in *Journal of Applied Physics* in 2016 [19].

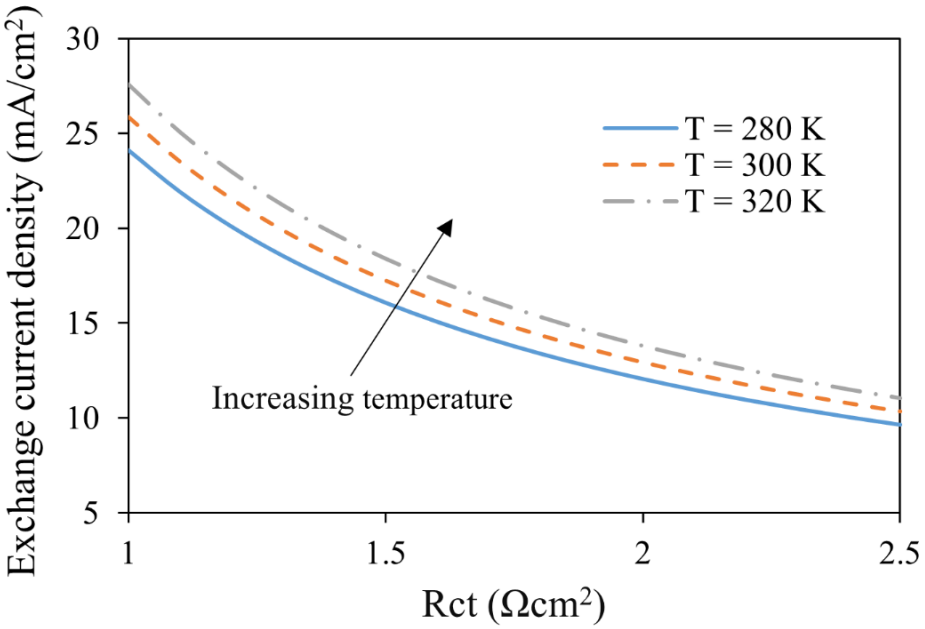

Figure 5.8. The dependence of exchange current density on charge transfer resistance (R_{ct}) at various temperature conditions.

5.4. Summary

This chapter presents a facile route to produce activated graphene nanoplatelets (aGNP) for use as cost-effective counter electrode materials in dye-sensitized solar cells. The microstructure of the prepared aGNPs was investigated using SEM and XRD. The SEM images show that aGNP film has a more curled, rough, and porous morphology, and XRD patterns confirm that the aGNP sample consists of high-purity graphene nanoplatelets, which exist in a disordered microstructure. The aGNP counter electrode with a thickness of 70 μm achieved an overall light-to-electric energy conversion efficiency of 7.7%, which is close to Pt counter electrode (8.1%). Further increase in thickness may not improve the efficiency due to reduced conductivity.

It is noteworthy that the aGNP based DSSCs outperform the Pt counterpart particularly in terms of short-circuit current density. Such remarkable J_{sc} can be attributed to the existence of hydroxyl groups, the increased surface area, and fast charge transport at electrolyte and CE interface. The Raman spectra show that KOH activation agent successfully introduces hydroxyl groups into graphene nanoplatelets, which provide additional active sites to increase the electrocatalytic activity of the aGNP CEs. Upon the KOH activation, the specific surface area of graphene nanoplatelets increases from 24 to 91 m^2/g, and the total pore volume increases from 0.034 cm^3/g to 0.19 cm^3/g. Such increase in both surface area and pore volume is due to the formation of a disordered microstructure as well as crumpled and curved morphology, which in turn contributes to the electrochemical performance of aGNP based CEs. In addition, experimental results obtained from EIS analysis indicates a fast charge transfer at the electrolyte/CE interface, which is desirable in improving cell efficiency. These above-mentioned experimental results suggest that the low-cost aGNP materials are a promising alternative to the conventional Pt electrode in DSSCs.

6. MODELING OF INTERFACIAL AND BULK CHARGE TRANSFER IN DYE-SENSITIZED SOLAR CELLS

6.1. Introduction

In the previous chapters, two types of cost-effective electrode materials have been tested for use as photoanodes and counter electrodes in DSSCs. Although these materials show great potential to outperform their conventional counterparts, it is challenging to fine-tune each of them and identify ideal conditions to optimize the overall performance in assembled devices. Hence, in this chapter, a first-principles mathematical model has been proposed to systematically analyze each of the cell components and their combinations, and it further predicts the power output characteristics of DSSCs under steady state operating conditions. In the proposed model, Butler-Volmer equation and Schottky barrier model were integrated with our previously developed electrical model [15] to evaluate the voltage losses at counter electrode/electrolyte and TiO_2/TCO interfaces, respectively. Experimental data acquired from typical DSSCs tested in our laboratory have been used to validate the theoretical fitted J-V characteristics of the presented model. This model fitted the experimental J-V curve more accurately at high voltages (0.65-0.8 V), compared to the simple diffusion model [180]. Parametric studies were conducted to analyze the effect of material characteristics and the operating parameters on the performance of DSSCs. Simulated results show that a "lower-limit" of shunt resistance (10^3 Ωcm^2) is necessary to guarantee a maximized efficiency. The model predicts a linear relationship between open circuit voltage (V_{oc}) and photoanode temperature (T) with a slope of -1 mV/°C, which is close to the experimental data reported in literature. Additionally, it is observed that a small value of overpotential (2.2 mV) occurs at the short-circuit condition (J_{sc} = 10.5 mA/cm^2), which is in close agreement with Volmer-

Butler equation. This observation suggests that, compared to the maximum attainable voltage (700 mV), the overpotential values are small and can be neglected for platinum catalyst based DSSCs.

6.2. Mathematical Model

The DSSC system is composed of two conducting electrodes and an electrolyte solution containing a redox couple (I^-/I_3^-). The electrodes are constructed on glass substrates and are coated with a transparent conducting oxide (TCO) layer. The working electrode (anode) consists of a dye-sensitized titanium dioxide (TiO_2) layer deposited on the TCO glass substrate; and the counter electrode is made of catalyst materials such as platinum to promote the reduction of the oxidized redox couple in the electrolyte. When exposed to sunlight, the dye sensitizers get excited and thereby generate electrons, which in turn get directly injected into the conduction band of the mesoporous oxide film (TiO_2). These electrons are transported to the anode and are utilized at external load before being collected by the electrolyte at counter electrode to complete the cycle. In this study, the DSSC cell has been modeled as a one-dimensional, homogeneous medium consisting nano-porous semiconductor TiO_2, dye, and redox electrolyte, which are intermingled with each other as shown in Figure 6.1. The continuity and transport equations are applied to all mobile charge carriers including electrons, iodide/triiodide ions, and cations. Assuming steady state operation conditions, the electrical characteristics of DSSC are predicted in terms of the transport features of electrons in TiO_2 semiconductor, I^-/I_3^- redox couple in the electrolyte solution, and the neutralizing counter cations.

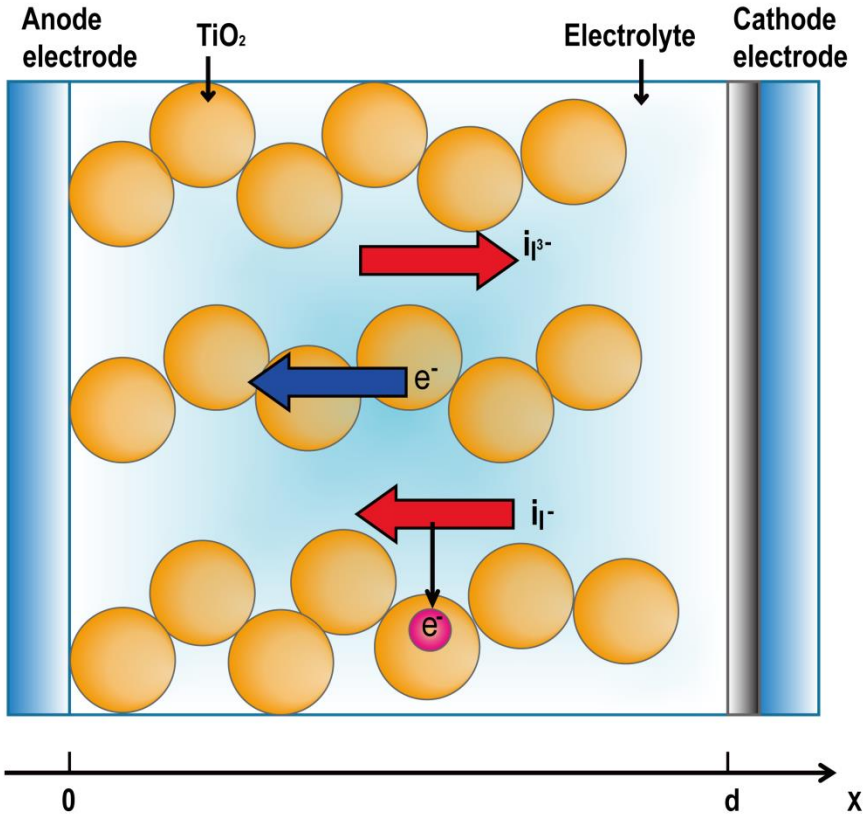

Figure 6.1. Schematic model for dye-sensitized solar cells [15].

6.2.1. Equations of continuity

The relaxation dynamics of photoinduced electrons in Ruthenium dye-sensitized TiO_2 solar cell is schematically shown in Figure 6.2. The forward process 1, 2, and 3 denote (i) electron excitation in the dye molecule, (ii) photogenerated electron injection into the conduction band (CB), and (iii) dye regeneration, respectively. In addition to the forward electron transfer and transport processes, the model also illustrates several competing electron loss pathways, including (a) excited dye molecules fall to ground state, (b) recombination of injected electrons with oxidized dye molecule S^+, and (c) recombination of injected electrons with I_3^-.

$$S + hv \rightarrow S^* \tag{6.1}$$

$$S^* \rightarrow S^+ + e_{CB}^- \quad (6.2)$$

$$2S^+ + 3I^- \rightarrow 2S + I_3^- \quad (6.3)$$

$$S^* \rightarrow S \quad (6.a)$$

$$S^+ + e_{CB}^- \rightarrow S^* \quad (6.b)$$

$$I_3^- + 2e_{CB}^- \rightarrow 3I^- \quad (6.c)$$

where S is the dye sensitizer; S^* is the electronically excited dye sensitizer; S^+ is the oxidized dye sensitizer; and I_3^-/I^- is the redox couple.

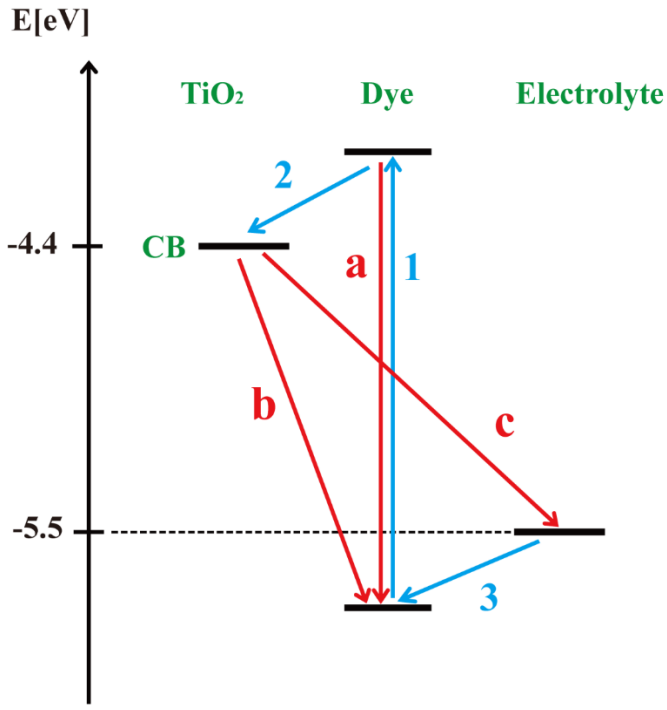

Figure 6.2. Kinetics of the $RuL_2(NCS)_2$ dye-sensitized TiO_2 solar cell with I^-/I_3^- redox mediator [15].

Previous experimental studies had shown that injection of an electron from dye molecule into TiO_2 conduction band occurred in the femtosecond time range which was much faster than the electron recombination with I_3^-. The characteristic time scales of the processes 1, 2, and 3 were

roughly estimated to be ~10^{-15} s, ~10^{-12} s, and ~10^{-8} s, respectively. These processes are fast enough that they are considered to be instantaneous processes that occur after photoexcitation. Therefore, in this study a perfect electron injection is assumed [181] and the electron generation rate $G_e(x)$ is expressed as:

$$G_e(x) = \int \Phi(\lambda)\alpha(\lambda)e^{-\alpha(\lambda)x}d\lambda \tag{6.4}$$

where $\Phi(\lambda)$ is power flux obtained from standard solar radiation AM1.5 spectrum, reduced by reflectance and absorptance of TCO glass by 11% ; $\alpha(\lambda)$ is the light absorption coefficient of the sensitizing dye at wavelength λ; and x is the coordinate along the direction of cell thickness as shown in Figure 6.1. It is assumed that the illumination enters the cell from the front side ($x = 0$). Ruthenium complex $RuL_2(NCS)_2$, also known as N719 dye, is used as light-absorbing dye sensitizer and the light absorption coefficient $\alpha(\lambda)$ is defined as

$$\alpha(\lambda) = \frac{\epsilon(\lambda)C_{dye}}{\log_{10} e} \tag{6.5}$$

In the above equation, $\epsilon(\lambda)$ refers to the molar extinction coefficient of sensitizing dye, and C_{dye} represents the absorbed dye concentration in the cell. C_{dye} is determined by the roughness factor of TiO_2 semiconductor, which can be calculated by:

$$C_{dye} = \frac{\sigma \times R_f}{d} \tag{6.6}$$

where σ represents the concentration of dye adsorbed on an ideal (virtual) flat surface of TiO_2 as a monolayer and the value is estimated to be $1.3\times10^{-10}\ mol/cm^2$ [182, 183].

Compared with forward processes, the backward processes are much slower. As shown in Figure 6.2, the relaxation of excited dye (path-a) and electron recombination in TiO_2 with dye (path-b) are only at the time scale of ~10^{-9} s and ~10^{-6} s, respectively. Therefore, both

recombination paths have been neglected. However, the electron recombination with I_3^- (path-c) has a high recombination rate of ~10^4 s^{-1} and hence this loss mechanism has been accounted in this model. When exposed to illumination, under stationary state the relaxation rate R_e of the conduction band electrons can be expressed as [184],

$$R_e = k_e \left\{ n_e \sqrt{\frac{n_{I_3^-}}{n_{I^-}}} - \bar{n}_e \sqrt{\frac{\bar{n}_{I_3^-}}{\bar{n}_{I^-}^3}} n_{I^-} \right\} \tag{6.7}$$

where k_e is the electron relaxation rate constant, n_e and $\bar{n}_e$ denote electron concentration under illumination and in equilibrium, respectively. While n_{I^-} and $n_{I_3^-}$ represent the iodide and triiodide concentration under illumination, the $\bar{n}_{I^-}$ and $\bar{n}_{I_3^-}$ represent the concentrations without any illumination (under equilibrium conditions). Under operating conditions, the second term on the right-hand side of Eq. (6.7) can be neglected because the electron concentration $\bar{n}_e$ is much lower compared to n_e. However, it becomes important when J-V dark curves have to be calculated under dark conditions.

Similar continuity equations have been formulated for electrons, iodide/triiodide ions, and cations. However, according to redox reaction at the front and back electrode, the generation of two electrons is always linked to the generation of one triiodide ion and the loss of three iodide ions. Thus, the continuity equation for current density for each species can be expressed as,

$$\frac{1}{e_0}\frac{dj_e}{dx} = R_e - G_e \tag{6.8}$$

$$\frac{1}{e_0}\frac{dj_{I^-}}{dx} = \frac{3}{2}G_e - \frac{3}{2}R_e = -\frac{3}{2e_0}\frac{dj_e}{dx} \tag{6.9}$$

$$\frac{1}{e_0}\frac{dj_{I_3^-}}{dx} = \frac{1}{2}R_e - \frac{1}{2}G_e = \frac{1}{2e_0}\frac{dj_e}{dx} \tag{6.10}$$

$$\frac{1}{e_0}\frac{dj_c}{dx} = 0 \tag{6.11}$$

where 'e_0' is the elementary charge; j_e, j_{I^-}, $j_{I_3^-}$, and j_c denote electron, iodide, triiodide and cation current densities, respectively. The cation current density is nullified, since the cations are not involved in any chemical reactions.

6.2.2. Transport equations

The movement of all four charged species can be described with transport equations. The current density j_e, j_{I^-}, $j_{I_3^-}$, j_c and electron density n_e satisfy the transport Eqs. (6.12)-(6.15) where D_e, D_{I^-}, $D_{I_3^-}$, and D_c represent the diffusion coefficients, while μ_e, μ_{I^-}, $\mu_{I_3^-}$, and μ_c represent the mobility of the individual charged species.

$$\frac{1}{e_0}j_e = D_e\frac{dn_e}{dx} + \mu_e n_e E \tag{6.12}$$

$$\frac{1}{e_0}j_{I^-} = D_{I^-}\frac{dn_{I^-}}{dx} + \mu_{I^-} n_{I^-} E \tag{6.13}$$

$$\frac{1}{e_0}j_{I_3^-} = D_{I_3^-}\frac{dn_{I_3^-}}{dx} + \mu_{I_3^-} n_{I_3^-} \tag{6.14}$$

$$\frac{1}{e_0}j_c = -D_c\frac{dn_c}{dx} + \mu_c n_c E \tag{6.15}$$

Relationship between the diffusion coefficient and mobility of the same charged species could be described using Einstein relation,

$$D = \frac{kT}{e_0}\mu \tag{6.16}$$

where k denotes the Boltzmann constant, and T represents absolute temperature. In Eqs. (6.12)-(6.15), the first and second terms on the right-hand side refer to the contributions associated with the diffusion due to the concentration gradient and the drift due to the electric field, respectively. The electric field E built in the cell can be characterized using Poisson's equation:

$$\frac{dE}{dx} = \frac{e_0}{\epsilon\epsilon_0}\left[n_c(x) - n_e(x) - n_{I^-}(x) - n_{I_3^-}(x)\right] \tag{6.17}$$

It is essential to have appropriate boundary conditions while solving the above listed set of six coupled non-linear differential equations (one continuity equation, four transport equations, and Poisson's equation) along with six independent variables (effective electric field, a current density of free electrons, and the concentration of all four charged species).

6.2.3. Boundary conditions

According to the law of conservation of the mass, the concentration of the cations and the number of the iodine nuclei are assumed to be constant, which yields the following three integral boundaries:

$$\int_0^d n_c\, dx = \int_0^d n_c^0\, dx = n_c^0 \cdot d \tag{6.18}$$

$$\int_0^d (n_{I_3^-} + \frac{1}{3} n_{I^-})\, dx = (n_{I_3^-}^0 + \frac{1}{3} n_{I^-}^0) \cdot d \tag{6.19}$$

$$\int_0^d (\frac{1}{2} n_e + \frac{1}{3} n_{I^-})\, dx = (\frac{1}{2} n_e^0 + \frac{1}{3} n_{I^-}^0) \cdot d \tag{6.20}$$

Because of the charge neutrality conditions, equilibrium concentration will satisfy the following equation.

$$\int_0^d \left(n_e + n_{I^-} + n_{I_3^-}\right) dx = (\, n_e^0 + n_{I^-}^0 + n_{I_3^-}^0) \cdot d = n_c^0 \cdot d \tag{6.21}$$

It is noted that the initial concentration of iodide and triiodide have to be multiplied by the porosity (p) to obtain $n_{I^-}^0$ and $n_{I_3^-}^0$ in the pseudo-homogeneous medium. As TCO substrate is a highly doped semiconductor or metal, its contact with TiO_2 is assumed to be ohmic, and hence no surface charge exists. Therefore,

$$E(0) = 0 \tag{6.22}$$

Also, since the movement of all the charged species is limited to the inner cell, the following conditions will be valid:

$$j_c(0) = j_{I^-}(0) = j_{I_3^-}(0) = j_e(d) = 0 \tag{6.23}$$

$$j_e(0) = j_g \tag{6.24}$$

where j_g is net current density. Current density at counter electrode ($x = d$) equals to net current density and can be expressed as:

$$j_g = j_0 \left\{ \sqrt{\frac{n_{I_3^-}(d) n_{I^-}^{OC}(d)}{n_{I_3^-}^{OC}(d) n_{I^-}(d)}} e^{(1-\beta)\frac{e_0}{kT}U_{Pt}} - \frac{n_{I^-}(d)}{n_{I^-}^{OC}(d)} e^{-\beta\frac{e_0}{kT}U_{Pt}} \right\} \tag{6.25}$$

where j_0 is the exchange current density at counter electrode, β is the symmetry parameter, $n_{I^-}^{OC}$ is the concentration of iodide in open circuit, $n_{I_3^-}^{OC}$ is the concentration of triiodide in open circuit, and U_{pt} is the overpotential. The overpotential depends on the catalytic activity of counter electrode and is needed to drive the reaction at certain current density. It can be defined as a deviation of redox energy E_{Redox} in operation from equilibrium E_{Redox}^{OC} in open-circuit conditions

$$U_{Pt} = \frac{1}{e_0}(E_{Redox} - E_{Redox}^{OC}) \tag{6.26}$$

The E_{Redox}^{OC} is given by Nernst's equation,

$$E_{Redox}^{OC} = E_{Redox}^{0\prime} - \frac{kT}{2} ln\left(\frac{n_{I_3^-}^{OC}(d)/n^{St}}{(n_{I^-}^{OC}(d)/n^{St})^3}\right) \tag{6.27}$$

where $E_{Redox}^{0\prime}$ indicates the formal potential which is approximated by the standard redox potential E_{Redox}^{0}, and the standard concentration n^{St} of "1 mol/l" is used as the reference concentration.

The internal voltage U_{int} shown in the equivalent electrical circuit (Figure 6.3) is determined by the redox potential E_{Redox}, quasi-Fermi level $E_F^n(0)$, as well as the voltage loss (U_l) at the TiO_2/TCO interface.

$$U_{int} = \frac{1}{e_0}[E_F^n(0) - E_{Redox}] - U_l \tag{6.28}$$

The Fermi-level $E_F^n(0)$ depends on the electron concentration $n_e(0)$ in TiO_2 conduction band. The quantitative relationship is depicted using the following equation:

$$E_F^n(0) = E_{CB} + kTln\left(\frac{n_e(0)}{N_{CB}}\right) \tag{6.29}$$

where E_{CB} reflects the energy level of the conduction band edge and N_{CB} relates to the effective density of states in the TiO_2 conduction band which can be expressed as

$$N_{CB} = 2\left(\frac{2\pi m_e^* kT}{h^2}\right)^{\frac{3}{2}} \tag{6.30}$$

where m_e^* represents effective electron mass, and "h" is the Planck's constant.

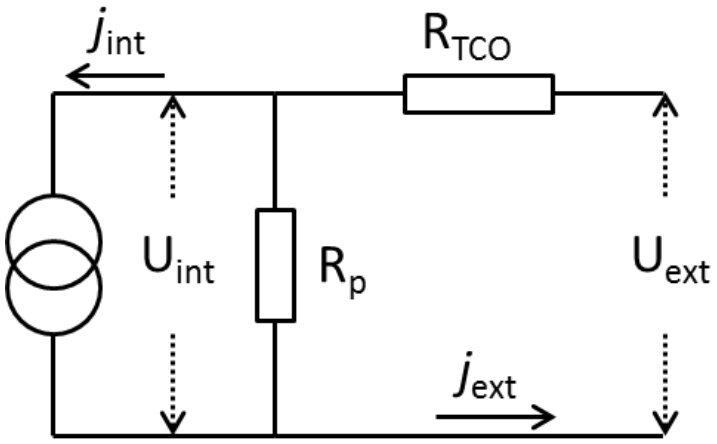

Figure 6.3. Equivalent circuit used to model the DSSC.

6.2.4. Schottky barrier effect

As shown in the Eq. (6.28), the voltage loss "U_l" at TiO_2/TCO interface plays a role in determining the actual internal voltage (U_{int}). The U_l can be evaluated using Schottky barrier model [25], in which TCO substrate is considered as a metal due to its high electrical conductivity.

Since TiO_2 material is an n-type semiconductor and TCO being highly conductive, the TiO_2/TCO contact can be treated as an n-type semiconductor with metal contact. Therefore, the voltage loss (U_l) depends on both Schottky barrier height (SBH) and current density (j_g) at the TiO_2/TCO interface. The quantitative relationship between SBH and current density is derived based on the thermionic-emission theory:

$$j_g = A^* T^2 \exp(-\frac{\phi_b}{kT})(\exp\left(\frac{qU_l}{kT}\right) - 1) \tag{6.31}$$

and

$$A^* = \frac{4\pi m^* q k^2}{h^3} \tag{6.32}$$

where h is the Planck constant equivalent to $6.626\times10^{-34}\ m^2 kg\ s^{-1}$, m^* is effective electron mass equal to 5.6 times the electron mass m_e [185], A^* is the Richardson constant of TiO_2 equal to $6.71\times10^6\ Am^{-2}K^{-2}$, and ϕ_b is the Schottky barrier height. The voltage loss can be expressed as a function of photocurrent:

$$U_l = \frac{kT}{q}\ln(1 + \frac{j_g}{A^* T^2 \exp(-\frac{\phi_b}{kT})}) \tag{6.33}$$

6.2.5. Equivalent circuit

An equivalent circuit as shown in Figure 6.3 is constructed to include other factors such as sheet resistance (R_{TCO}), shunt resistance (R_p), and external resistance (R_{ext}). R_{TCO} is the series resistance due to the TCO layers, and R_p represents the shunt resistance due to internal leakages in the cell. The external resistance, R_{ext}, indicates the electrical load. The internal current is determined by the current density at $x = 0$ and the cell area (A):

$$I_{int} = Aj_e(0) \tag{6.34}$$

Based on the equivalent circuit, the external current I_{ext} is obtained based on Kirchhoff's laws:

$$I_{ext} = \frac{R_p}{R_{ext} + R_{TCO} + R_p} A j_e(0) \tag{6.35}$$

The internal voltage equals the voltage drop across the TCO and the external resistance.

$$U_{int} = (R_{TCO} + R_{ext}) I_{ext} = \frac{(R_{TCO} + R_{ext}) R_p}{R_{ext} + R_{TCO} + R_p} A j_e(0) \tag{6.36}$$

Combining Eq. (6.26)-(6.29) and (6.36), an explicit expression of U_{pt} can be obtained. Substituting U_{pt} into the current-overpotential equation (6.25), along with boundary condition Eq. (6.24), yields a combined boundary condition at $x = 0$ and $x = d$.

$$f(n_{I^-}(d), n_{I_3^-}(d), n_e(0), j_e(0); R_{ext}) = 0 \tag{6.37}$$

By varying R_{ext}, complete J-V curves can be obtained. It should be noted that the above listed boundary condition, combining values of variables at both points $x = 0$ and $x = d$, are numerically unfavorable. However, this problem can be resolved by adding additional trivial differential equations with appropriate local boundary conditions [20]. Due to the Poisson's equation, the ODEs are extremely stiff and hence more grid points need to be meshed particularly on the boundaries. A relaxation method can solve the ODEs efficiently with 150 grid points for each variable. The flow chart of the simulation program is shown in Figure 6.4. The calculation begins from open-circuit condition ($R_{ext} \rightarrow \infty$) using equilibrium values as an initial input estimate. The initial values are compared to a solution calculated by the relaxation method to calculate/check the relative error. If the error is greater than a specified tolerance, the solution replaces initial values and the procedure is repeated. Once the error is less than the tolerance, the solution is recorded and used as an initial estimate for a reduced R_{ext}. The above described procedure is carried out for each R_{ext} value until R_{ext} reaches zero (short-circuit condition).

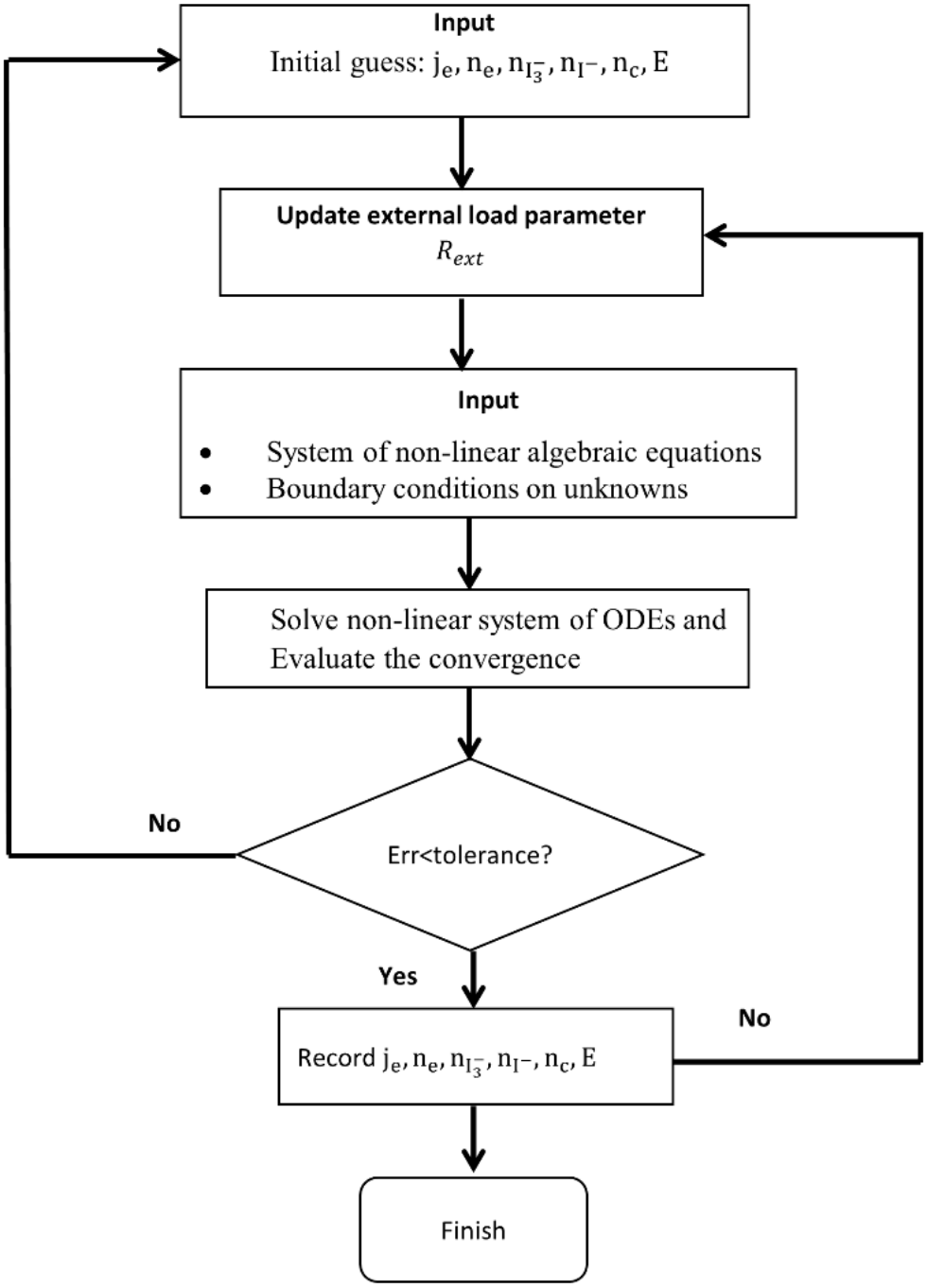

Figure 6.4. Flow chart of relaxation method iteration procedure.

The non-dimensionalization is a useful tool to facilitate numerical solution of the governing equations. It minimizes the direct dependence on the constants by using ratio of constants. Additionally, the non-dimensionalized numerical equations can be solved in much less time, and is also less prone to instability. The ordinary differential equations (ODEs) in this model can be non-dimensionalized using the following dimensionless variables:

$$n_e^* = \frac{n_e}{\overline{n_e}},\ n_{I^-}^* = \frac{n_{I^-}}{\overline{n_{I^-}}},\ n_{I_3^-}^* = \frac{n_{I_3^-}}{\overline{n_{I_3^-}}},\ n_c^* = \frac{n_c}{\overline{n_c}},\ x^* = \frac{x}{L} \tag{6.38}$$

For the sake of brevity, the dimensionless model equations are not given here.

6.3. Results and Discussion

The numerical model developed in the previous section has been applied to predict experimental results and assess the effect of key parameters on the performance of dye-sensitized solar cells. In general, the cell performance can be expressed in terms of overall device efficiency and maximum power output.

6.3.1. Model validation

In order to validate the proposed numerical model, simulation of typical dye-sensitized solar cells has been carried out to fit the experimental measurements. The values of the basic input parameters used in the simulation are listed in Table 6.1 and the fitting parameters are listed in the caption of Figure 6.5. The DSSCs were fabricated using TiO_2 photoanode, Pt-coated counter electrode, and I^-/I_3^- electrolyte. The thickness of the active layer is 10 μm and the active area is 0.125 cm^2. A detailed description of the fabrication procedure used in this study has been published by the authors [186]. The DSSCs were tested at Advanced Photovoltaic Center, South Dakota State University. The overall device efficiency was measured to be 7.6% under standard 1 Sun illumination conditions. It can be seen from Figure 6.5 that the DSSC behaves like a near

constant current source for low values of voltage (under 0.5 V) and the current is close to short-circuit current J_{sc}. When the voltage increases, the current begins to decrease exponentially and reaches zero at open-circuit voltage (V_{oc}). The trend in photocurrent density has been captured through our simulation, and the J-V plot generated by the proposed model agrees reasonably well with the experimental data. However, there appears to be a minor discrepancy at the maximum power point, which might be due to the overestimated fill factor (FF) value. This overestimation reflects the additional internal resistance caused by the electrolyte layer [184] which has not been accounted in the proposed model.

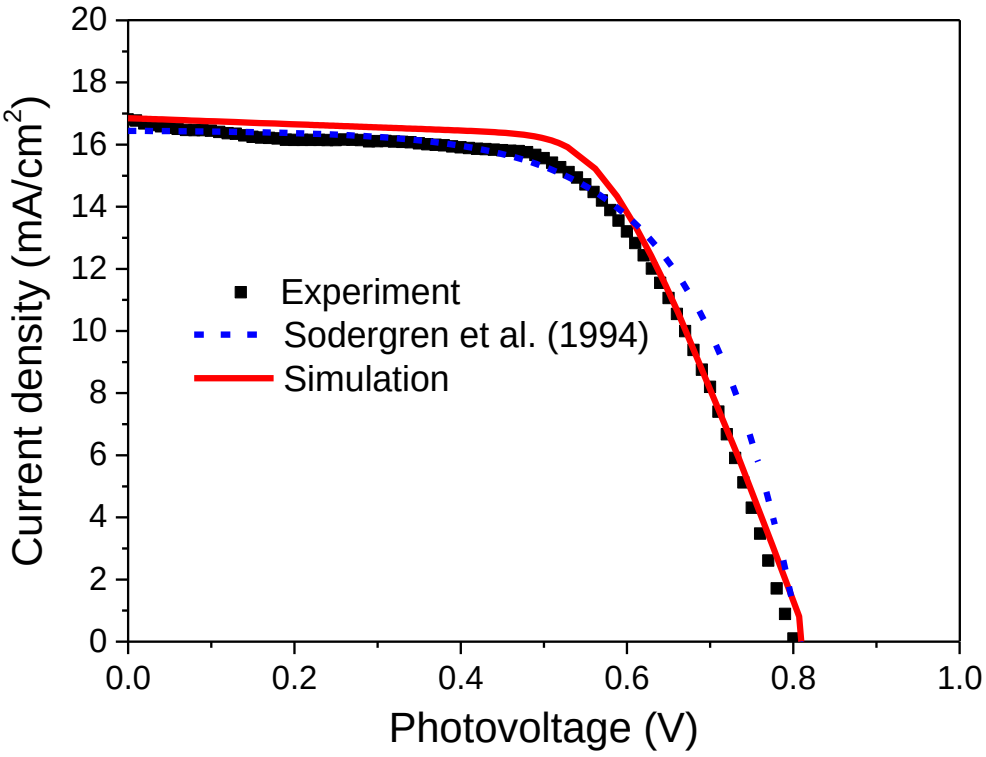

Figure 6.5. Validation of the present numerical model with the experimental results. The fit parameters of the calculated curve are: R_p = 1 kΩ, R_{TCO} = 12 Ω, k_e = 100 s^{-1}, dye concentration = 10×C_{dye}; other parameters as in Table 6.1. The fit parameters of simple diffusion model are: τ = 100 ms; other parameters same as in [180].

Table 6.1. Base case parameters used for simulation of dye-sensitized solar cells.

Symbol	Value	Note
k_e	$10^4\ s^{-1}$	Electron relaxation rate constant
μ_e	$0.3\ cm^2/Vs$	Electron mobility
D_{I^-}	$8.5\times10^{-6}\ cm^2/s$	Iodide diffusion constant
$D_{I_3^-}$	$8.5\times10^{-6}\ cm^2/s$	Triiodide diffusion constant
C_{I^-}	$0.45\ M$	Initial concentration of iodide
$C_{I_3^-}$	$0.05\ M$	Initial concentration of triiodide
m_e^*	$5.6\ m_e$	Effective mass of electron
ϵ	50	Relative dielectric constant
$E_{CB} - E_{Redox}^0$	$0.93\ eV$	Difference of conduction band and standard electrolyte redox energy
d	$10\ \mu m$	Thickness of inner cell
A	$1\ cm^2$	Cell area
p	0.5	Porosity of TiO_2 semiconductor
R_f	1000	Roughness factor of TiO_2 semiconductor
T	$298\ K$	Temperature
A^*	$6.71\times10^6\ Am^{-2}K^{-2}$	Richardson constant
ϕ_b	$0.5\ eV$	Schottky barrier height
σ	$1.3\times10^{-10}\ mol/cm^2$	Concentration of dye adsorbed on an idea (virtual) flat surface of TiO_2 as a monolayer

Apart from the model being validated using experimental data, it was also compared with the simple diffusion model developed by Sodergren et al. [180]. The simple diffusion model is widely adopted because it provides an analytical solution in terms of J-V characteristics, which in turn facilitates the study of the cell parameters such as thickness, diffusion coefficient, and electron lifetime [25, 187]. It can be seen in Figure 6.5 that the simple diffusion model marginally overpredicts the current output at high voltages. This may be due to the fact that the said model does not include an equivalent circuit and therefore the effects of series resistance R_{TCO} and shunt resistance R_p (representing internal leakage) have not been considered. Studies have shown that both R_{TCO} and R_p are critical in dictating the photovoltaic performance of DSSCs [188], and hence it is essential to take into account of those variables to accurately predict the J-V characteristics. In practice, increasing the shunt resistance and decreasing the series resistance could lead to a higher FF value, thus resulting in greater efficiency and pushing the power output of the DSSC closer toward its theoretical maximum.

6.3.2. Effect of series resistance

The DSSC performance is a function of design parameters as well as operating parameters and material properties. In order to study the effect of important parameters, other parameters that affect system performance have been specified as listed in Table 6.1. The proposed model was utilized to investigate the effect of sheet resistance R_{TCO} of transparent conductive oxide (TCO) layer on the glass substrate. The simulated results show that DSSC performance is sensitive to the sheet resistance. Sheet resistance of TCO plays a major role contributing to the series resistance which in turn has a strong influence on the filling factor of the J-V curve and maximum power output. As shown in Figure 6.6 that, the "squareness" of the J-V curve decreases with an increase in the R_{TCO} from 0 to 14 Ω/sq which reflects a low fill factor. This reduced fill factor, in fact, has

a negative impact on the power output. For instance, at the given open-circuit voltage and short-circuit current, the maximum power output decreases proportionally with the fill factor as shown in Figure 6.7. However, it should be noted that even a minimal reduction in R_{TCO} could remarkably improve power output as well as the device efficiency. The reduction of R_{TCO} is not easy to achieve in actual experiments. In practice, indium tin oxide (ITO, In_2O_3:Sn) film exhibits an excellent low sheet resistance (ca. 6 Ω/sq) along with an ideal transparency (> 80%); however, its low resistance property could deteriorate drastically during the high temperature calcination process (DSSCs fabrication). As an alternative, fluoride-doped tin oxide (SnO_2:F, FTO) with a similar structure and comparable sheet resistance has been widely used due to its capability of withstanding high calcination temperatures. It is critical to develop low-resistivity TCO substrate for large-scale DSSCs, since the high resistivity of substrates will not only affect the power output but also lead to a lower optimal width in the DSSC module [61].

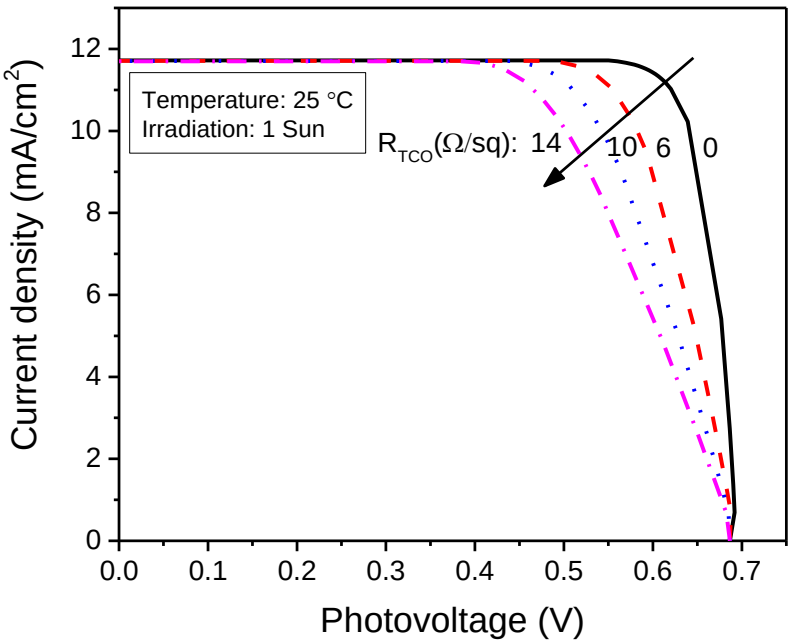

Figure 6.6. The effect of the sheet resistance R_{TCO} on the J-V characteristics of the modeled DSSC.

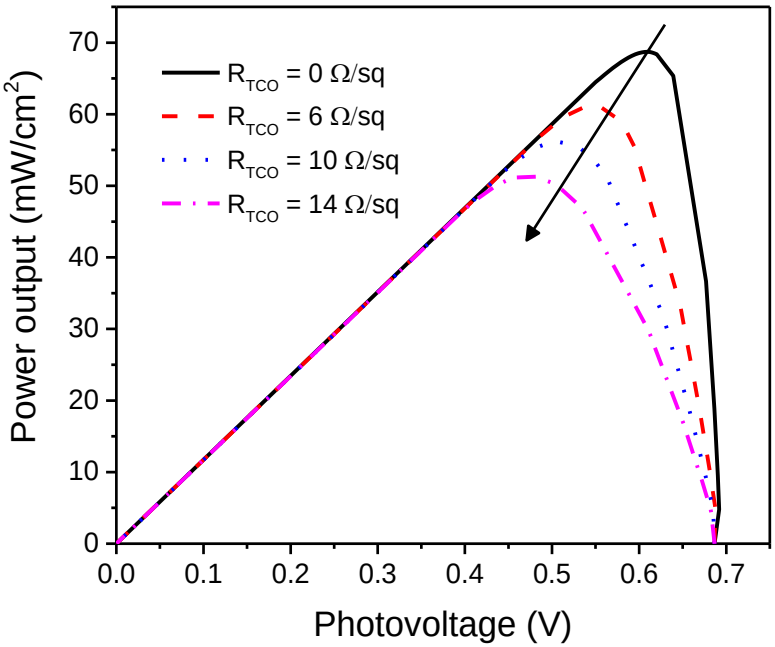

Figure 6.7. The effect of the sheet resistance R_{TCO} on the power-voltage characteristics of the modeled DSSC.

6.3.3. Effect of shunt resistance

Yet another important parameter that influences the cell performance is the shunt resistance (R_p). In conventional pn-junction solar cells, the shunt resistance represents the leakage across the pn-junction around the edge of the cell and the presence of crystal defects and/or impurities in the junction region. Similarly, in DSSC, a shunt resistance is added to an equivalent circuit to describe the back-electron transfer across the TiO_2/dye/electrolyte junction which generally occurs in the dye-free regions of the electrodes [189]. The effects of shunt resistance on the J-V characteristics are plotted in Figure 6.8. The J-V characteristics are obtained by varying R_p value from 0.1 to 10 kΩ. As expected, for any given junction voltage, the lower the shunt resistance, the lower the current density is. This is because, as the shunt resistance decreases, the current leakage increases. It can also be seen in Figure 6.8, that as the shunt resistance decreases, the voltage-controlled portion of the J-V curve begins to sag towards the origin at low R_p, resulting in a significant decrease in the short-circuit current and a marginal reduction in V_{oc}. Note when the shunt resistance value becomes very low ($R_p < 0.1$ kΩ), a significant reduction in both J_{sc} and V_{oc} are realized. This is because at low R_p the electron recombination rate becomes high between TiO_2 electrode and electrolyte. For any given DSSC, this "lower-limit" of R_p could be quantified by evaluating the slope of the J-V curve at short-circuit current point. Typically, it is recommended to design a DSSC towards maximum efficiency, i.e., to ensure that R_p value is close to the order of 10^3 Ωcm^2 (under ideal conditions). Research has shown that a high shunt resistance (R_p) can be achieved through TCO surface passivation [190].

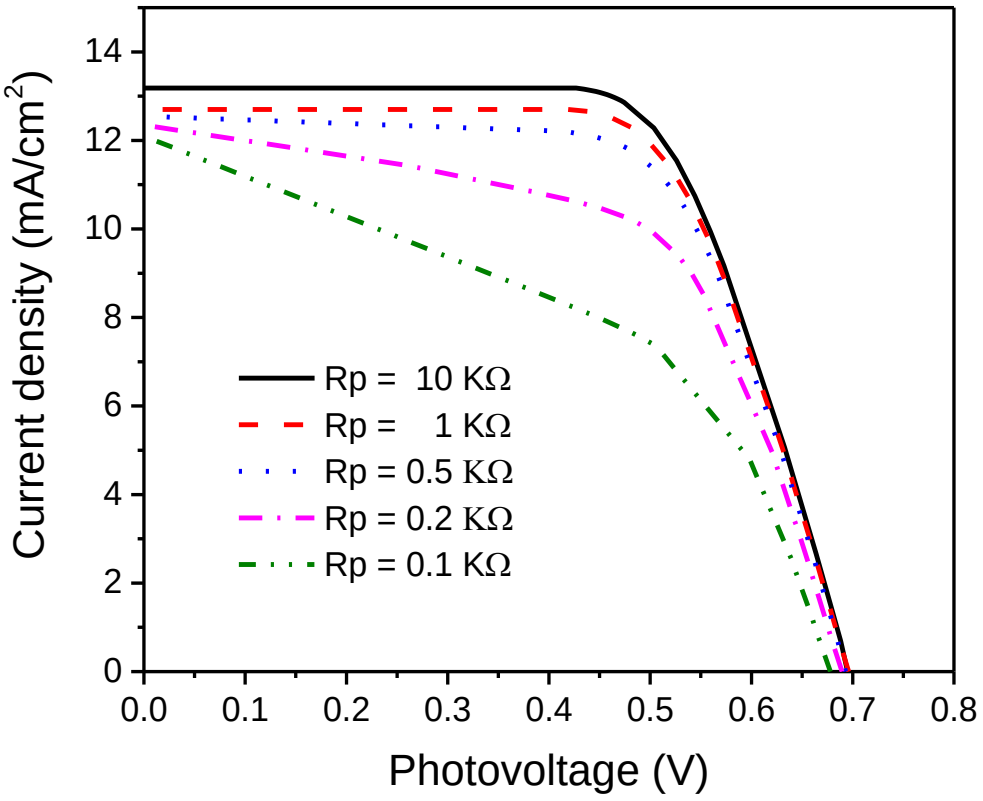

Figure 6.8. The effect of the shunt resistance R_p on the J-V characteristics of the modeled DSSC.

6.3.4. Effect of operating temperature

Apart from shunt resistance, photoanode temperature (T) also has an impact on the attainable open-circuit voltage (V_{oc}). The dependence of the open-circuit voltage on photoanode temperature is shown in Figure 6.9. It can be seen that as the photoanode temperature increases from 10 to 60 °C, open-circuit voltage decreases from 700 to 650 mV. This can be attributed to two factors: the change in electron density (n_e) and the shift in TiO_2 conduction band edge. As shown in Eq. (6.28), the electron density (n_e) has a strong influence on the quasi-Fermi level of TiO_2 (E_F), which in turn determines the maximum attainable open-circuit voltage in theory ($E_F - E_{Redox}$). As seen in Figure 6.9, there exists a linear relationship between V_{oc} and T with a

slope of -1 mV/°C, which is in agreement with the literature reported experimental data (ca. -2.5 mV/°C) [191, 192]. Compared with the experimental data, the predicted slope is gentler due to the fact that the proposed model has not accounted of the shift in TiO_2 conduction band edge potential. Previous study has shown that V_{oc} dependence on photoanode temperature can be attributed to a shift of TiO_2 conduction band edge (E_{cb}) [192]. This shift is caused by differences in the surface electric field between the TiO_2 and the electrolyte, which is influenced by a number of factors such as electrolyte composition, surface properties of TiO_2, and temperature changes [193]. It should be noted that the presence of a Schottky barrier was reported at the FTO/TiO_2 interface; however, V_{oc} is independent of the Schottky barrier height [185].

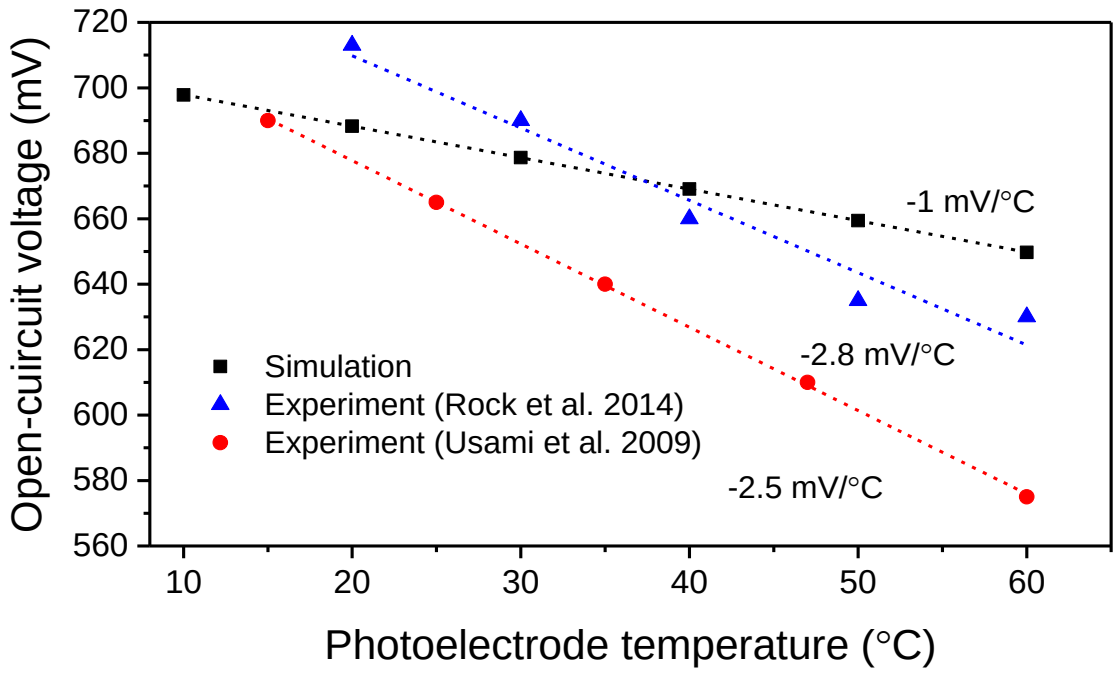

Figure 6.9. Open-circuit voltage vs photoelectrode temperature for DSSCs measured under AM 1.5 illumination. The lines are linear fits to the data. [191, 192]

6.3.5. Effect of E_{cb} - E_{redox}

As mentioned above, the maximum attainable open-circuit voltage V_{oc} generated in DSSCs can be determined by E_{cb} - E_{redox}. In this study, it was calculated to be 0.7 V under standard test conditions. Since E_F is dependent on E_{cb}, one effective way to obtain a higher V_{oc} is to increase the energy difference between conduction band edge (E_{cb}) and redox potential (E_{redox}). In the base case simulation, the value of E_{cb} - E_{redox} was assumed to be constant; however, in actual practice it could vary due to the band edge shift. Influence of energy difference E_{cb} - E_{redox} on J-V characteristics is plotted in Figure 6.10. It could be seen that for the given short-circuit current (J_{sc}) and fill factor (FF), as E_{cb} - E_{redox} increases from 0.9 to 1.1 eV, there occurs an increase in V_{oc} of similar magnitude from 0.66 to 0.86 V. Hence, it could be interpreted that the E_{cb} - E_{redox} has a dominant effect on the open-circuit voltage compared to the electron density (n_e). Figure 6.11 confirms that V_{oc} and E_{cb} - E_{redox} have a linear relationship where as E_{cb} - E_{redox} difference increases (0.9 to 1.1 eV), the maximum power output linearly increases from 5.8 to 8.2 mW/cm^2. This is due to the fact that, at given J_{sc} and FF, the maximum power output (P_{max}) increases proportionally with V_{oc} ($P_{max} = V_{oc} \times J_{sc} \times FF$). Therefore, it is critical to design DSSCs with a higher value of E_{cb} - E_{redox} to improve cell performance in terms of both open-circuit voltage and maximum power output. For given conduction band edge (E_{cb}), a higher E_{cb} - E_{redox} can be achieved through using alternative redox couples such as Co(II)/Co(III) [70] and $Fe(CN)_6^{3-/4-}$ [194] complexes, which have higher values of redox potential (E_{redox}). Recent research has proven that, by tuning the redox potential to match the oxidation potential of the sensitizer, the energy loss can be minimized in the dye regeneration step which paves the way to attain a high V_{oc} approaching ~1 V [195].

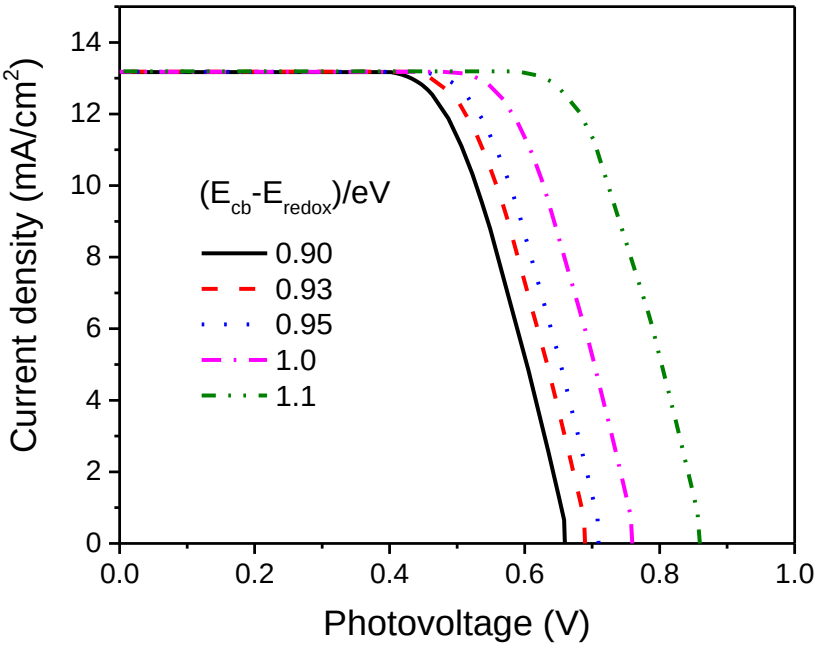

Figure 6.10. The effect of the energy difference (E_{cb} - E_{redox}) on the J-V characteristics of the modeled DSSC.

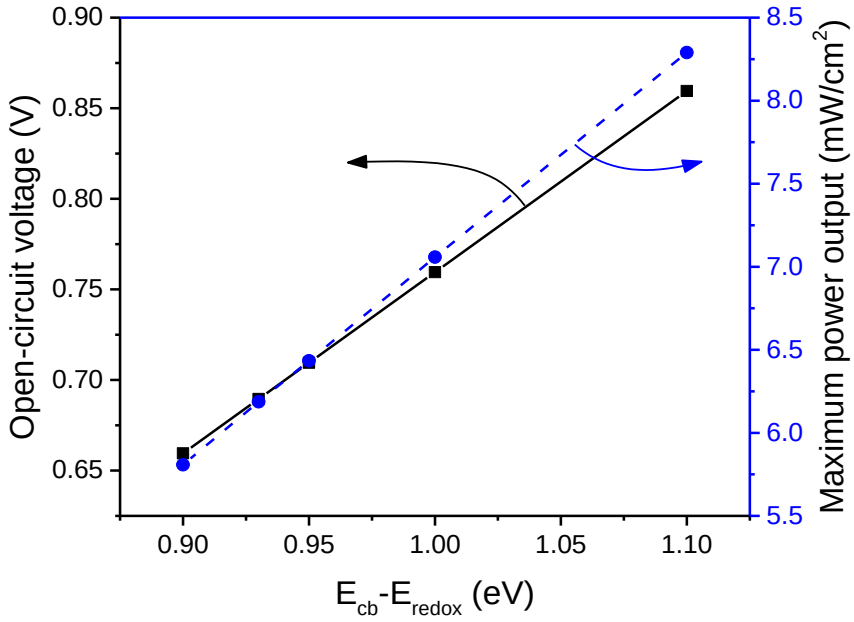

Figure 6.11. The effect of the energy difference (E_{cb} - E_{redox}) on the open-circuit voltage and maximum power output of the modeled DSSC.

6.3.6. Effect of overpotential

Yet another way to maximize the power output is to minimize the interfacial voltage losses. One of the main mechanisms that dictate the voltage loss is the overpotential that exists at the interface of electrolyte and counter electrode. The interfacial overpotential has two components: (i) diffusion overpotential and (ii) charge-transfer overpotential. Diffusion overpotential is generated due to diffusion limitations that occur in the electrolyte, while charge-transfer overpotential results from the fact that electrons have to pass through a solid-liquid phase boundary (Helmholtz layer). Both of these overpotentials are taken into account in the proposed model based on a generalized current-overpotential approach [Eq. (6.25)], where the variation in surface concentrations are no longer negligible.

The dependence of overpotential on the photocurrent density is plotted in Figure 6.12. As shown, the photocurrent influences the overpotential linearly. That is, as the photocurrent density increases from zero to the J_{sc} = 10.5 mA/cm^2, there is an increase in the overpotential to 2.2 mV. The simulated results are in close agreement with the Butler-Volmer equation in which variation of redox couple concentration is negligible, which results in the low values of the overpotential. Hence, with an assumption that redox couple $n_{I_3^-}$ and n_{I^-} do not deviate much from open-circuit conditions, the concentrations of ion species can be approximated with their equilibrium values ($n_{I_3^-} = n_{I_3^-}^{OC}$ and $n_{I^-} = n_{I^-}^{OC}$) which simplifies the Eq. (6.25) to the following Butler-Volmer equation.

$$j_g = j_0 \left[e^{(1-\beta)\frac{e_0}{kT}U_{Pt}} - e^{-\beta\frac{e_0}{kT}U_{Pt}} \right] \tag{6.39}$$

For small overpotentials ($\left|U_{pt}\right| \ll \frac{kT}{e_0}$), the Bulter-Volmer equation can be linearized.

$$j_g = j_0 \left[\frac{e_0 U_{pt}}{kT} + \frac{1-2\beta}{2} \left(\frac{e_0 U_{pt}}{kT} \right)^2 + \frac{1-2\beta-2\beta^2}{6} \left(\frac{e_0 U_{pt}}{kT} \right)^2 + \cdots \right] \quad (6.40)$$

The listed leading-order approximation indicates that the photocurrent has a linear relationship with overpotential.

$$j_g = \frac{j_0 e_0}{kT} U_{pt} \quad (6.41)$$

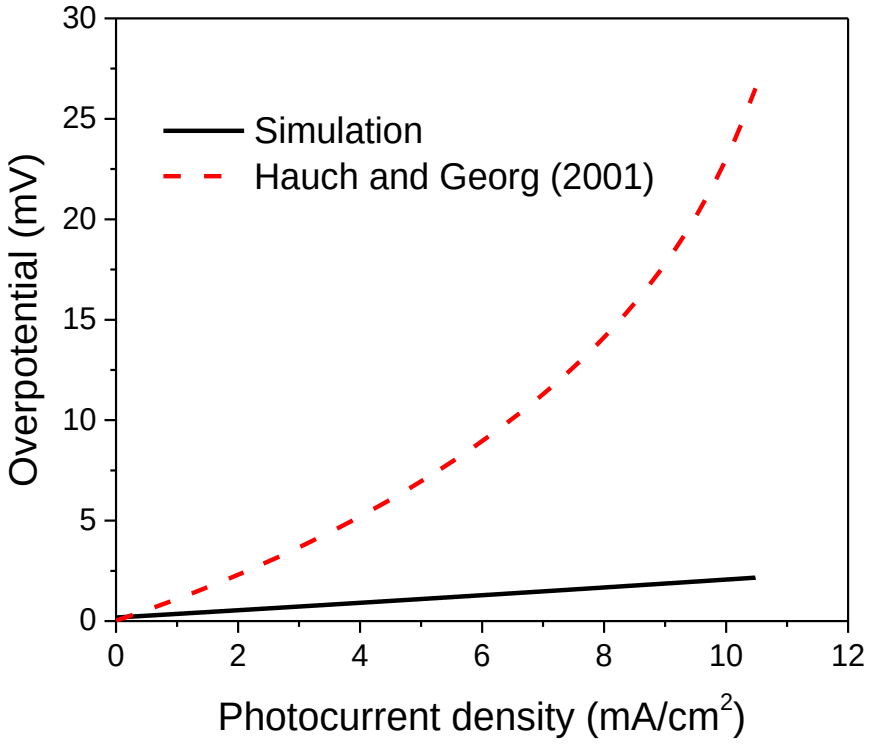

Figure 6.12. Comparison of the simulated results with theoretically predicted diffusion overpotential [177].

In general, the exchange current density (j_0) is higher for an electrochemical reaction which is quicker and more reversible. The value of j_0 can range from 10^{-60} A/cm^2 in a very slow and irreversible reaction to 10^{-1} A/cm^2 in a fast and reversible reaction. The thermally produced Pt catalyst has j_0 of approximately 0.05-0.35 A/cm^2 [196]. In this study, 0.1 A/cm^2 was adopted which

corresponds to overpotential less than 5 mV at short-circuit condition. Such small overpotential is usually expected in the DSSCs, because they utilize highly efficient catalyst materials such as platinum and graphene nanoplatelets [19]. However, it is reported in the literature [197] that for carbonaceous materials which are highly porous, the diffusion overpotential of redox couple through the pores may become a limiting factor. Due to the large excess of I^- in the electrolyte, only the I_3^- diffusion limits the current [198]. Hence, the depletion of I_3^- at the counter electrode leads to the diffusion overpotential. Ideally, for a 2-nm thin layer Pt [177, 199], the diffusion overpotential (η_D) is given as:

$$\eta_D = \frac{kT}{e_0}\ln(1 - \frac{I}{I_{lim}}) \tag{6.42}$$

The diffusion-limiting current (I_{lim}) was measured to be $I_{lim} = 120\ mA$. It can be seen from Figure 6.12 that, as photocurrent density of Pt catalyst increases to 10.5 mA/cm^2, the η_D increases of Pt catalyst exponentially from 0 to 26.5 mV which is one order of magnitude larger than the simulated results (2.2 mV). The discrepancy between diffusion overpotential and the simulated results of the current study can be attributed to the low limiting current ($I_{lim} = 120\ mA$) which reflects a diffusion controlled electrode reaction at the counter electrode surface. For platinum counter electrode, the short-circuit current density could reach up to $200\ mA$ and hence a much lower η_D can be expected. It is worth noting that compared to the maximum attainable voltage (700 mV), the overpotential values are small and can be neglected for platinum catalyst based DSSCs [15].

6.4. Summary

A macroscopic, one-dimensional mathematical model of dye-sensitized solar cells has been presented. This model improved the simplified electrical model [15] through incorporating the interfacial charge transport phenomenon at TiO_2/TCO and electrolyte/counter electrode contacts. Due to these improvements, the present model fitted the experimental J-V characteristics more accurately compared to the conventional diffusion model. The prediction accuracy was increased by adding an equivalent electrical circuit, which correlates internal resistance to sheet resistance and current leakage to shunt resistance. The calculated overall conversion efficiencies agree well with experimental results, which confirms the validity of the proposed model. The effect of important parameters such as series resistance, shunt resistance, $E_{cb} - E_{Redox}$, and interfacial overpotential on J-V characteristics was simulated. The simulated results showed a linear relationship between open-circuit voltage (V_{oc}) and photoanode temperature (T) with a slope of -1 mV/°C, which is in agreement with published results. This bulk and interfacial model gives an insight into the relation between physical processes in DSSCs and their photovoltaic performance. It can serve as an effective tool for studying various cell designs and operating parameters. Also, it can be tailored to simulate the performance of novel DSSCs using promising energy materials such as polymer electrolyte, and graphene-based counter electrode.

7. CONCLUSIONS & FUTURE RESEARCH

7.1. Summary of Main Conclusions

In this dissertation, two rational synthesis routes have been successfully formulated for fabrication of two nanostructured electrode materials (i.e. SnO_2 nanofibers and activated graphene nanoplatelets) for use as photoanode and counter electrode in dye-sensitized solar cells. The main objective of the research is to explore the favorable charge transport features of SnO_2 nanofiber network and simultaneously replace the high-priced conventional electrocatalytic nanomaterials (e.g. Pt nanoparticles) used in existing counter electrode of DSSCs. To achieve this objective, a detailed quantitative physical model was developed to optimize various design parameters and cell configurations.

During the study, porous and hollow SnO_2 nanofibers were prepared by electrospinning technique via a single capillary from PVP/Sn precursor/dual solvents system, followed by controlled carbonization. In the carbonization process, PVP as a sacrificial template was gradually decomposed to maintain fibrous structures of SnO_2 network, which was further incorporated with P25-TiO_2 nanoparticles to form an innovative SnO_2 nanofiber/TiO_2 nanoparticle structure. This hybrid structure guarantees the high photovoltaic performance of the resulting DSSCs with noticeably enhanced power conversion efficiency. Particularly, the continuous SnO_2/TiO_2 networks functioned as the excellent current transport pathways to suppress the charge recombination of the photoanode due to their high electron mobility and excellent topological connectivity.

Furthermore, activated graphene nanoplatelets (aGNP) were successfully produced from pristine graphene nanoplatelets (GNP) through a hydrothermal method using KOH as the activating agent. These porous structured aGNP possessed excellent electrocatalytic activity for

triiodide reduction at the interface between electrolyte and counter electrode. The power conversion efficiency achieved using this aGNP based counter electrode was comparable to the counter electrodes using conventional solution-processed Pt.

Detailed microstructural and photovoltaic characterization were successfully performed by means of SEM, TEM, XRD, Raman spectrometry, and EIS. The photovoltaic performances of the two porous nanostructured materials synthesized in this study are presented in Table 7.1.

Table 7.1. Photovoltaic parameters of the DSSC devices based on (a) photoanodes made from SnO_2 nanofibers and SnO_2/TiO_2 composites; and (b) counter electrodes made from aGNP and Pt.

Electrode	Material	V_{oc} (V)	J_{sc} ($mAcm^{-2}$)	FF	η (%)
Photoanode	SnO_2 (I) nanofiber	0.70	5.90	0.41	1.68
	SnO_2 (I)/TiO_2 compos	0.79	10.10	0.57	4.54
	SnO_2 (II) nanofiber	0.75	10.75	0.50	4.06
	SnO_2 (II)/TiO_2 composite	0.80	11.97	0.60	5.72
Counter electrode	aGNP	0.73	22.54	0.47	7.73
	Pt	0.80	17.28	0.59	8.16

Note: The SnO_2 nanofibers are denoted as SnO_2 (I) for those carbonized at 500 °C and SnO_2 (II) for those carbonized at 600 °C, respectively.

From Table 7.1, it can be found that the innovative hybrid structured SnO_2/TiO_2 composites can significantly enhance their photovoltaic performance compared to electrospun SnO_2 nanofibers by increasing their specific surface area. The values of power conversion efficiency

(PCE) of SnO_2 (I)/TiO_2 and SnO_2 (II)/TiO_2 as photoanode materials of DSSCs are 4.54% and 5.72% against electrospun SnO_2 nanofibers with the PCE values of 1.68% and 4.06%. In addition, by introducing the activated graphene nanoplatelets via a facile hydrothermal route, the values of PCE of the resulting aGNP based DSSCs are 7.73% which is near close to the Pt (8.16%). Also, these advanced graphene electrode materials exhibit very good stability.

In addition, a macroscopic one-dimensional mathematical model of dye-sensitized solar cells has been presented. This model was improved over the simplified electrical model [15] through incorporating the interfacial charge transport phenomenon at TiO_2/TCO and electrolyte/counter electrode contacts. The proposed model was validated by experimental measurements. Compared to the simple diffusion model, it fitted the experimental J-V characteristics more accurately. The accuracy of the model prediction is greatly improved due to the addition of a constructed electrical circuit which correlates internal resistance to sheet resistances and current leakage to shunt resistance. The calculated overall conversion efficiencies agree reasonably well with experimental results, which confirms the validity of the proposed model. The effect of the series resistance, shunt resistance, $E_{cb} - E_{redox}$, and interfacial overpotential on J-V characteristics was simulated. The simulated results showed a linear relationship between open-circuit voltage (V_{oc}) and photoanode temperature (T) with a slope of -1 mV/°C, which is in agreement with experimental data published in the literature [191, 192]. This bulk and interfacial charge-transfer model provides a deep understanding into the relation between physical processes in DSSCs and overall cell performance. It can serve as an effective tool for studying various cell designs and operating parameters. Also, it can be tailored to simulate the performance of novel DSSCs using promising energy materials such as polymer electrolyte and graphene-based counter electrode.

7.2. Future Research

DSSCs are becoming the future of energy production because of their cost-effectiveness and increasing conversion efficiency levels. Towards full commercialization, challenges remain in further improvement of device stability as well as reduction of material and manufacturing costs. The present study attempted to address these challenges by exploring promising low-cost but high-efficient energy nanomaterials (SnO_2 nanofibers and aGNP). In addition, theoretical modeling carried out in this dissertation provides insight into the principles of newly designed devices. The experimental work along with theoretical study also opens up several future potential investigations in this field.

7.2.1. Hybrid nanostructures

One-dimensional nanostructured SnO_2 metal oxides have proven salient advantages over conventional TiO_2 nanoparticles in terms of higher charge mobility and stronger light harvesting capability at long wavelengths (600-800 nm). However, the relatively low specific surface area and insufficient dye attachment are the major limitations of SnO_2 nanofiber based DSSCs. A hybrid structure of nanofibers and nanoparticles has potential to retain the favorable features (e.g. high mobility and light scattering) while compensating the loss for surface area and dye attachments. To realize this objective, further studies can focus on optimizing SnO_2 nanofiber diameter, controlling ratios of nanofibers and nanoparticles, increasing the crystallinity, and reducing surface defects on the SnO_2 nanofibers.

7.2.2. Graphene electrodes

Graphene and its composites are promising alternatives to Pt as counter electrode materials due to their high transparent (>85%) and good electrocatalytic activity. Experimental results have shown that aGNP which are rich in hydroxyl group exhibit higher catalytic activity than pristine

graphene. These findings confirm that electrocatalytic properties of graphene nanoplatelets are proportional to the concentration of active sites (defects, and functional groups), independent of the electrolyte medium [91]. Therefore, to further enhance the electrocatalytic activity, one practical research direction is to develop effective synthetic methods that can introduce defects and functional groups to porous aGNP. Recently, Tang et al. developed a new solar cell by integrating an electron-enriched graphene electrode for electric signal outputs on rainy days with a dye-sensitized solar cell (DSSC) for photoelectric conversion on sunny days [200]. The new concept of using graphene electrodes as energy conversion device provides guidance on the design of advanced all-weather solar cells.

7.2.3. Low temperature processing

One limitation of current processing techniques for both the dominant platinum catalyst and the activated graphene nanoplatelets is the high sintering temperatures (~400 °C). High temperature processing increases the costs associated with manufacturing, and it severely limits the substrates available for production. Developing methods to obtain high surface area, stable, and ideally highly conductive electrodes at heat treatments below 200 °C would greatly reduce costs. Recently, Seo et al. [201] developed graphene oxide nanosheets based counter electrode on plastic substrates using electrochemical control at low temperature (≤ 100 °C). This work opens up opportunities for using a variety of common plastics as substrates.

7.2.4. Theoretical modeling

A number of extensions to the modeling work are possible, which could improve the predictive qualities of the proposed models and enable future studies on novel energy materials and cell configurations. One important extension is to investigate the transient response of DSSCs. The model equations presented in this study could be further extended to include the rate of change

for each differential equation. However, careful consideration would be required to determine the time step size in the numerical algorithm, which must account for ultrafast injection from excited dye molecules. In addition, the system of governing equations is expected to be extremely stiff, so not only is the time step size important but also the choice of numerical solver/algorithm.

REFERENCES

[1] U.S. fossil fuel energy consumption from 1985 to 2016. http://www.statista.com/statistics/183617/us-energy-consumption-from-fossil-fuels-since-1985/.

[2] Li B, Wang L, Kang B, Wang P, Qiu Y. Review of recent progress in solid-state dye-sensitized solar cells. Solar Energy Materials and Solar Cells. 2006;90:549-73.

[3] Cohen MR. A Clean Energy Economy for North Dakota: Analysis of the Rural Economic Development Potential of Renewable Resources. 2010.

[4] Pimentel D, Patzek TW. Ethanol production using corn, switchgrass, and wood; biodiesel production using soybean and sunflower. Natural Resources Research. 2005;14:65-76.

[5] Renewables 2010 global status report. http://www.ren21.net/Portals/0/documents/activities/gsr/REN21_GSR_2010_full_revised%20Sept2010.pdf.

[6] Solarbuzz, technologies. www.solarbuzz.com/going-solar/understanding/technologies.

[7] Administration USEI. Levilized Cost of New Generation Resources in the Annual Energy Outlook 2011.

[8] Administration USEI. What is U.S. electricity generation by energy source.

[9] Heliatek sets new organic photovoltaic world record efficiency of 13.2%. http://www.heliatek.com/en/press/press-releases/details/heliatek-sets-new-organic-photovoltaic-world-record-efficiency-of-13-2.

[10] Gevorgyan SA, Madsen MV, Dam HF, Jørgensen M, Fell CJ, Anderson KF, et al. Interlaboratory outdoor stability studies of flexible roll-to-roll coated organic photovoltaic modules: stability over 10,000 h. Solar Energy Materials and Solar Cells. 2013;116:187-96.

[11] O'regan B, Grätzel M. A low-cost, high-efficiency solar cell based on dye-sensitized colloidal TiO_2 films. Nature. 1991;353:737-40.

[12] Burschka J, Pellet N, Moon S-J, Humphry-Baker R, Gao P, Nazeeruddin MK, et al. Sequential deposition as a route to high-performance perovskite-sensitized solar cells. Nature. 2013;499:316-9.

[13] Gong J, Sumathy K, Liang J. Polymer electrolyte based on polyethylene glycol for quasi-solid state dye sensitized solar cells. Renewable Energy. 2012;39:419-23.

[14] Mathew S, Yella A, Gao P, Humphry-Baker R, Curchod BF, Ashari-Astani N, et al. Dye-sensitized solar cells with 13% efficiency achieved through the molecular engineering of porphyrin sensitizers. Nature Chemistry. 2014;6:242-7.

[15] Gong J, Sumathy K, Liang J. A simplified electrical model of the dye-sensitised photoelectrochemical cell. International Journal of Sustainable Energy. 2014;35:75-87.

[16] Gong J, Liang J, Sumathy K. Review on dye-sensitized solar cells (DSSCs): fundamental concepts and novel materials. Renewable and Sustainable Energy Reviews. 2012;16:5848-60.

[17] Gong J, Qiao H, Sigdel S, Elbohy H, Adhikari N, Zhou Z, et al. Characteristics of SnO_2 nanofiber/TiO_2 nanoparticle composite for dye-sensitized solar cells. AIP Advances. 2015;5:067134.

[18] Sigdel S, Elbohy H, Gong J, Adhikari N, Sumathy K, Qiao H, et al. Dye-sensitized solar cells based on porous hollow tin oxide nanofibers. IEEE Transactions on Electron Devices. 2015;62:2027-32.

[19] Gong J, Zhou Z, Sumathy K, Yang H, Qiao Q. Activated graphene nanoplatelets as a counter electrode for dye-sensitized solar cells. Journal of Applied Physics. 2016;119:135501.

[20] Ferber J, Stangl R, Luther J. An electrical model of the dye-sensitized solar cell. Solar Energy Materials and Solar Cells. 1998;53:29-54.

[21] Korfiatis D, Potamianou S, Thoma K-AT. Modeling of dye-sensitized titanium dioxide solar cells. Ionics. 2008;14:545-8.

[22] Joshi P, Korfiatis D, Potamianou S, Thoma K-AT. Optimum oxide thickness for dye-sensitized solar cells—effect of porosity and porous size. A numerical approach. Ionics. 2013;19:571-6.

[23] Bavarian M, Nejati S, Lau KK, Lee D, Soroush M. Theoretical and experimental study of a dye-sensitized solar cell. Industrial & Engineering Chemistry Research. 2013;53:5234-47.

[24] Gentilini D, D'Ercole D, Gagliardi A, Brunetti A, Reale A, Brown T, et al. Analysis and simulation of incident photon to current efficiency in dye sensitized solar cells. Superlattices and Microstructures. 2010;47:192-6.

[25] Ni M, Leung MKH, Leung DYC, Sumathy K. Theoretical modeling of TiO_2/TCO interfacial effect on dye-sensitized solar cell performance. Solar Energy Materials and Solar Cells. 2006;90:2000-9.

[26] Ogiya K, Lv C, Suzuki A, Sahnoun R, Koyama M, Tsuboi H, et al. Simulation of electron diffusion in TiO_2 porous structures in dye-sensitized solar cells. Japanese Journal of Applied Physics. 2009;48:04C166.

[27] Onodera M, Ogiya K, Suzuki A, Tsuboi H, Hatakeyama N, Endou A, et al. Modeling of dye-sensitized solar cells based on TiO_2 electrode structure model. Japanese Journal of Applied Physics. 2010;49:04DP10.

[28] Ogiya K, Lv C, Suzuki A, Sahnoun R, Koyama M, Tsuboi H, et al. Development of multiscale simulator for dye-sensitized TiO_2 nanoporous electrode based on quantum chemical calculation. Japanese Journal of Applied Physics. 2008;47:3010.

[29] Ni M, Leung MK, Leung DY, Sumathy K. Theoretical modeling of TiO_2/TCO interfacial effect on dye-sensitized solar cell performance. Solar Energy Materials and Solar Cells. 2006;90:2000-9.

[30] Onodera M, Nagumo R, Miura R, Suzuki A, Tsuboi H, Hatakeyama N, et al. Multiscale simulation of dye-sensitized solar cells considering schottky barrier effect at photoelectrode. Japanese Journal of Applied Physics. 2011;50:04DP6.

[31] Andrade L, Sousa J, Ribeiro HA, Mendes A. Phenomenological modeling of dye-sensitized solar cells under transient conditions. Solar Energy. 2011;85:781-93.

[32] Mitroi MR, Fara L, Ciurea ML. Numerical procedure for optimizing dye-sensitized solar cells. Journal of Nanomaterials. 2014;2014:2.

[33] Filipič M, Berginc M, Smole F, Topič M. Analysis of electron recombination in dye-sensitized solar cell. Current Applied Physics. 2012;12:238-46.

[34] Shockley W, Read Jr W. Statistics of the recombinations of holes and electrons. Physical Review. 1952;87:835.

[35] Marcus RA. On the theory of electron-transfer reactions. VI. Unified treatment for homogeneous and electrode reactions. The Journal of Chemical Physics. 1965;43:679-701.

[36] Nithyanandam K, Pitchumani R. Analysis and design of dye-sensitized solar cell. Solar Energy. 2012;86:351-68.

[37] Tanaka S. Performance simulation for dye-sensitized solar cells: toward high efficiency and solid state. Japanese Journal of Applied Physics. 2001;40:97.

[38] Fredin K, Rühle S, Grasso C, Hagfeldt A. Studies of coupled charge transport in dye-sensitized solar cells using a numerical simulation tool. Solar Energy Materials and Solar Cells. 2006;90:1915-27.

[39] Chitambar M, Wang Z, Liu Y, Rockett A, Maldonado S. Dye-sensitized photocathodes: efficient light-stimulated hole injection into p-GaP under depletion conditions. Journal of the American Chemical Society. 2012;134:10670-81.

[40] Liu Y, Sun Y, Rockett A. A new simulation software of solar cells—wxAMPS. Solar Energy Materials and Solar Cells. 2012;98:124-8.

[41] Miettunen K, Halme J, Visuri A-M, Lund P. Two-dimensional time-dependent numerical modeling of edge effects in dye solar cells. The Journal of Physical Chemistry C. 2011;115:7019-31.

[42] Gagliardi A, der Maur MA, Gentilini D, Di Carlo A. Modeling of dye sensitized solar cells using a finite element method. Journal of Computational Electronics. 2009;8:398-409.

[43] Gagliardi A, der Maur MA, Gentilini D, Di Carlo A. Simulation of dye solar cells: through and beyond one dimension. Journal of Computational Electronics. 2011;10:424-36.

[44] Gagliardi A, Maur D, Auf M, Carlo AD. Theoretical investigation of a dye solar cell wrapped around an optical fiber. IEEE Journal of Quantum Electronics. 2011;47:1214-21.

[45] Nelson J. Continuous-time random-walk model of electron transport in nanocrystalline TiO_2 electrodes. Physical Review B. 1999;59:15374.

[46] Usami A, Ozaki H. Computer simulations of charge transport in dye-sensitized nanocrystalline photovoltaic cells. The Journal of Physical Chemistry B. 2001;105:4577-83.

[47] Nelson J, Chandler RE. Random walk models of charge transfer and transport in dye sensitized systems. Coordination Chemistry Reviews. 2004;248:1181-94.

[48] Wang Y, Wu D, Fu L-M, Ai X-C, Xu D, Zhang J-P. Density of state determination of two types of intra-gap traps in dye-sensitized solar cells and its influence on device performance. Physical Chemistry Chemical Physics. 2014;16:11626-32.

[49] Hsiao P-T, Tung Y-L, Teng H. Electron transport patterns in TiO_2 nanocrystalline films of dye-sensitized solar cells. The Journal of Physical Chemistry C. 2010;114:6762-9.

[50] Kopidakis N, Neale NR, Zhu K, van de Lagemaat J, Frank AJ. Spatial location of transport-limiting traps in TiO_2 nanoparticle films in dye-sensitized solar cells. Applied Physics Letters. 2005;87:202106.

[51] Van de Lagemaat J, Frank A. Effect of the surface-state distribution on electron transport in dye-sensitized TiO_2 solar cells: nonlinear electron-transport kinetics. The Journal of Physical Chemistry B. 2000;104:4292-4.

[52] Wang Y, Wu D, Fu LM, Ai XC, Xu D, Zhang JP. Correlation between Energy and Spatial Distribution of Intragap Trap States in the TiO_2 Photoanode of Dye-Sensitized Solar Cells. ChemPhysChem. 2015.

[53] Villanueva-Cab J, Jang S-R, Halverson AF, Zhu K, Frank AJ. Trap-free transport in ordered and disordered TiO_2 nanostructures. Nano Letters. 2014;14:2305-9.

[54] Nelson J, Haque SA, Klug DR, Durrant JR. Trap-limited recombination in dye-sensitized nanocrystalline metal oxide electrodes. Physical Review B. 2001;63:205321.

[55] Ansari-Rad M, Abdi Y, Arzi E. Monte Carlo random walk simulation of electron transport in dye-sensitized nanocrystalline solar cells: influence of morphology and trap distribution. The Journal of Physical Chemistry C. 2012;116:3212-8.

[56] Han L, Koide N, Chiba Y, Mitate T. Modeling of an equivalent circuit for dye-sensitized solar cells. Applied Physics Letters. 2004;84:2433-5.

[57] Bisquert J, Mora-Sero I. Simulation of steady-state characteristics of dye-sensitized solar cells and the interpretation of the diffusion length. Journal of Physical Chemistry Letters. 2010;1:450-6.

[58] Hanmin T, Xiaobo Z, Shikui Y, Xiangyan W, Zhipeng T, Bin L, et al. An improved method to estimate the equivalent circuit parameters in DSSCs. Solar Energy. 2009;83:715-20.

[59] Wang L, Fang XM, Zhang ZG. Two-step precise determination of the parameters of the single-diode equivalent circuit model for dye-sensitized solar cells. Heat Transfer Engineering. 2014;35:1007-13.

[60] Sarker S, Seo HW, Lee K-S, Jin Y-K, Ju H, Kim DM. Exact analytical analysis of current density-voltage curves of dye-sensitized solar cells. Solar Energy. 2015;115:390-5.

[61] Huang Y, Dai S, Chen S, Zhang C, Sui Y, Xiao S, et al. Theoretical modeling of the series resistance effect on dye-sensitized solar cell performance. Applied Physics Letters. 2009;95:243503.

[62] Giannuzzi R, Manca M, Gigli G. A new electrical model for the analysis of a partially shaded dye-sensitized solar cells module. Progress in Photovoltaics: Research and Applications. 2013;21:1520-30.

[63] Tian H, Zhang J, Wang X, Yu T, Zou Z. Influence of capacitance characteristic on I-V measurement of dye-sensitized solar cells. Measurement. 2011;44:1551-5.

[64] Cid JJ, Yum JH, Jang SR, Nazeeruddin MK, Martínez-Ferrero E, Palomares E, et al. Molecular cosensitization for efficient panchromatic dye-sensitized solar cells. Angewandte Chemie. 2007;119:8510-4.

[65] Chen Y, Zeng Z, Li C, Wang W, Wang X, Zhang B. Highly efficient co-sensitization of nanocrystalline TiO_2 electrodes with plural organic dyes. New Journal of Chemistry. 2005;29:773-6.

[66] Robertson N. Catching the rainbow: light harvesting in dye-sensitized solar cells. Angewandte Chemie International Edition. 2008;47:1012-4.

[67] Mishra A, Fischer MK, Bäuerle P. Metal-free organic dyes for dye-sensitized solar cells: from structure: property relationships to design rules. Angewandte Chemie International Edition. 2009;48:2474-99.

[68] Clifford JN, Palomares E, Nazeeruddin MK, Thampi R, Grätzel M, Durrant JR. Multistep electron transfer processes on dye co-sensitized nanocrystalline TiO_2 films. Journal of the American Chemical Society. 2004;126:5670-1.

[69] Choi H, Kim S, Kang SO, Ko J, Kang MS, Clifford JN, et al. Stepwise cosensitization of nanocrystalline TiO_2 films utilizing Al_2O_3 layers in dye-sensitized solar cells. Angewandte Chemie International Edition. 2008;47:8259-63.

[70] Yella A, Lee H-W, Tsao HN, Yi C, Chandiran AK, Nazeeruddin MK, et al. Porphyrin-sensitized solar cells with cobalt (II/III)–based redox electrolyte exceed 12 percent efficiency. Science. 2011;334:629-34.

[71] Lee K, Park SW, Ko MJ, Kim K, Park N-G. Selective positioning of organic dyes in a mesoporous inorganic oxide film. Nature Materials. 2009;8:665-71.

[72] Miao Q, Wu L, Cui J, Huang M, Ma T. A new type of dye-sensitized solar cell with a multilayered photoanode prepared by a film-transfer technique. Advanced Materials. 2011;23:2764-8.

[73] Chen X, Mao SS. Titanium dioxide nanomaterials: synthesis, properties, modifications, and applications. Chem Reviews. 2007;107:2891-959.

[74] Usami A. Theoretical study of application of multiple scattering of light to a dye-sensitized nanocrystalline photoelectrochemical cell. Chemical Physics Letters. 1997;277:105-8.

[75] Usami A. Theoretical simulations of optical confinement in dye-sensitized nanocrystalline solar cells. Solar Energy Materials and Solar Cells. 2000;64:73-83.

[76] Ferber J, Luther J. Computer simulations of light scattering and absorption in dye-sensitized solar cells. Solar Energy Materials and Solar Cells. 1998;54:265-75.

[77] Chiba Y, Islam A, Watanabe Y, Komiya R, Koide N, Han L. Dye-sensitized solar cells with conversion efficiency of 11.1%. Japanese Journal of Applied Physics. 2006;45:L638.

[78] Hore S, Vetter C, Kern R, Smit H, Hinsch A. Influence of scattering layers on efficiency of dye-sensitized solar cells. Solar Energy Materials and Solar Cells. 2006;90:1176-88.

[79] Chang YJ, Kong EH, Park YC, Jang HM. Broadband light confinement using a hierarchically structured TiO_2 multi-layer for dye-sensitized solar cells. Journal of Materials Chemistry A. 2013;1:9707-13.

[80] Joshi P, Zhang L, Davoux D, Zhu Z, Galipeau D, Fong H, et al. Composite of TiO_2 nanofibers and nanoparticles for dye-sensitized solar cells with significantly improved efficiency. Energy & Environmental Science. 2010;3:1507-10.

[81] Kawamura G, Ohmi H, Tan WK, Lockman Z, Muto H, Matsuda A. Ag nanoparticle-deposited TiO_2 nanotube arrays for electrodes of dye-sensitized solar cells. Nanoscale Research Letters. 2015;10:1-6.

[82] Kondo Y, Yoshikawa H, Awaga K, Murayama M, Mori T, Sunada K, et al. Preparation, photocatalytic activities, and dye-sensitized solar-cell performance of submicron-scale TiO_2 hollow spheres. Langmuir. 2008;24:547-50.

[83] Wang X, Tian J, Fei C, Lv L, Wang Y, Cao G. Rapid construction of TiO_2 aggregates using microwave assisted synthesis and its application for dye-sensitized solar cells. RSC Advances. 2015;5:8622-9.

[84] Li C, Luo Y, Guo X, Li D, Mi J, Sø L, et al. Mesoporous TiO_2 aggregate photoanode with high specific surface area and strong light scattering for dye-sensitized solar cells. Journal of Solid State Chemistry. 2012;196:504-10.

[85] Zhang Q, Myers D, Lan J, Jenekhe SA, Cao G. Applications of light scattering in dye-sensitized solar cells. Physical Chemistry Chemical Physics. 2012;14:14982-98.

[86] Qian J, Liu P, Xiao Y, Jiang Y, Cao Y, Ai X, et al. TiO_2-coated multilayered SnO_2 hollow microspheres for dye-sensitized solar cells. Advanced Materials. 2009;21:3663-7.

[87] Lim CK, Wang Y, Zhang L. Facile formation of a hierarchical TiO_2-SnO_2 nanocomposite architecture for efficient dye-sensitized solar cells. RSC Advances. 2016;6:25114-22.

[88] Wali Q, Fakharuddin A, Ahmed I, Ab Rahim MH, Ismail J, Jose R. Multiporous nanofibers of SnO_2 by electrospinning for high efficiency dye-sensitized solar cells. Journal of Materials Chemistry A. 2014;2:17427-34.

[89] Elumalai NK, Jose R, Archana PS, Chellappan V, Ramakrishna S. Charge transport through electrospun SnO_2 nanoflowers and nanofibers: role of surface trap density on electron transport dynamics. Journal of Physical Chemistry C. 2012;116:22112-20.

[90] Krishnamoorthy T, Tang MZ, Verma A, Nair AS, Pliszka D, Mhaisalkar SG, et al. A facile route to vertically aligned electrospun SnO_2 nanowires on a transparent conducting oxide substrate for dye-sensitized solar cells. Journal of Materials Chemistry. 2012;22:2166-72.

[91] Kavan L, Yum JH, Grätzel M. Optically transparent cathode for dye-sensitized solar cells based on graphene nanoplatelets. ACS Nano. 2010;5:165-72.

[92] Roy-Mayhew JD, Bozym DJ, Punckt C, Aksay IA. Functionalized graphene as a catalytic counter electrode in dye-sensitized solar cells. ACS Nano. 2010;4:6203-11.

[93] Hong W, Xu Y, Lu G, Li C, Shi G. Transparent graphene/PEDOT-PSS composite films as counter electrodes of dye-sensitized solar cells. Electrochemistry Communications. 2008;10:1555-8.

[94] Trancik JE, Barton SC, Hone J. Transparent and catalytic carbon nanotube films. Nano Letters. 2008;8:982-7.

[95] Chen J, Li K, Luo Y, Guo X, Li D, Deng M, et al. A flexible carbon counter electrode for dye-sensitized solar cells. Carbon. 2009;47:2704-8.

[96] Gregg BA. Interfacial processes in the dye-sensitized solar cell. Coordination Chemistry Reviews. 2004;248:1215-24.

[97] Cameron PJ, Peter LM. How does back-reaction at the conducting glass substrate influence the dynamic photovoltage response of nanocrystalline dye-sensitized solar cells? The Journal of Physical Chemistry B. 2005;109:7392-8.

[98] Cameron PJ, Peter LM, Hore S. How important is the back reaction of electrons via the substrate in dye-sensitized nanocrystalline solar cells? The Journal of Physical Chemistry B. 2005;109:930-6.

[99] Yu H, Zhang S, Zhao H, Will G, Liu P. An efficient and low-cost TiO_2 compact layer for performance improvement of dye-sensitized solar cells. Electrochimica Acta. 2009;54:1319-24.

[100] Lee S, Noh JH, Han HS, Yim DK, Kim DH, Lee J-K, et al. Nb-doped TiO_2: a new compact layer material for TiO_2 dye-sensitized solar cells. Journal of Physical Chemistry C. 2009;113:6878-82.

[101] Guan J, Zhang J, Yu T, Xue G, Yu X, Tang Z, et al. Interfacial modification of photoelectrode in ZnO-based dye-sensitized solar cells and its efficiency improvement mechanism. RSC Advances. 2012;2:7708-13.

[102] Huang N, Liu Y, Peng T, Sun X, Sebo B, Tai Q, et al. Synergistic effects of ZnO compact layer and $TiCl_4$ post-treatment for dye-sensitized solar cells. Journal of Power Sources. 2012;204:257-64.

[103] Palomares E, Clifford JN, Haque SA, Lutz T, Durrant JR. Control of charge recombination dynamics in dye sensitized solar cells by the use of conformally deposited metal oxide blocking layers. Journal of the American Chemical Society. 2003;125:475-82.

[104] Elbohy H, Thapa A, Poudel P, Adhikary N, Venkatesan S, Qiao Q. Vanadium oxide as new charge recombination blocking layer for high efficiency dye-sensitized solar cells. Nano Energy. 2015;13:368-75.

[105] Wali Q, Fakharuddin A, Jose R. Tin oxide as a photoanode for dye-sensitised solar cells: current progress and future challenges. Journal of Power Sources. 2015;293:1039-52.

[106] Chen X, Liu L, Peter YY, Mao SS. Increasing solar absorption for photocatalysis with black hydrogenated titanium dioxide nanocrystals. Science. 2011;331:746-50.

[107] Su T, Yang Y, Na Y, Fan R, Li L, Wei L, et al. An insight into the role of oxygen vacancy in hydrogenated TiO_2 nanocrystals in the performance of dye-sensitized solar cells. ACS Applied Materials & Interfaces. 2015;7:3754-63.

[108] Guai GH, Song QL, Lu ZS, Ng CM, Li CM. Tailor and functionalize TiO_2 compact layer by acid treatment for high performance dye-sensitized solar cell and its enhancement mechanism. Renewable Energy. 2013;51:29-35.

[109] Wang Z-S, Zhou G. Effect of surface protonation of TiO_2 on charge recombination and conduction band edge movement in dye-sensitized solar cells. The Journal of Physical Chemistry C. 2009;113:15417-21.

[110] Ronca E, Marotta G, Pastore M, De Angelis F. Effect of sensitizer structure and TiO_2 protonation on charge generation in dye-sensitized solar cells. Journal of Physical Chemistry C. 2014;118:16927-40.

[111] Kim Y, Yoo BJ, Vittal R, Lee Y, Park N-G, Kim K-J. Low-temperature oxygen plasma treatment of TiO_2 film for enhanced performance of dye-sensitized solar cells. Journal of Power Sources. 2008;175:914-9.

[112] Kim JT, Kim SH. Surface modification of TiO_2 electrode by various over-layer coatings and O_2 plasma treatment for dye sensitized solar cells. Solar Energy Materials and Solar Cells. 2011;95:336-9.

[113] Lee B-K, Kim J-J. Enhanced efficiency of dye-sensitized solar cells by UV-O_3 treatment of TiO_2 layer. Current Applied Physics. 2009;9:404-8.

[114] Kim HJ, Kim J, Hong B. Effect of hydrogen plasma treatment on nano-structured TiO_2 films for the enhanced performance of dye-sensitized solar cell. Applied Surface Science. 2013;274:171-5.

[115] Wu W-Y, Shih T-W, Chen P, Ting J-M, Chen J-M. Plasma surface treatments of TiO_2 photoelectrodes for use in dye-sensitized solar cells. Journal of the Electrochemical Society. 2011;158:K101-K6.

[116] He J, Lindström H, Hagfeldt A, Lindquist S-E. Dye-sensitized nanostructured p-type nickel oxide film as a photocathode for a solar cell. The Journal of Physical Chemistry B. 1999;103:8940-3.

[117] Qin P, Zhu H, Edvinsson T, Boschloo G, Hagfeldt A, Sun L. Design of an organic chromophore for p-type dye-sensitized solar cells. Journal of the American Chemical Society. 2008;130:8570-1.

[118] Morandeira A, Fortage J, Edvinsson T, Le Pleux L, Blart E, Boschloo G, et al. Improved photon-to-current conversion efficiency with a nanoporous p-type NiO electrode by the use of a sensitizer-acceptor dyad. The Journal of Physical Chemistry C. 2008;112:1721-8.

[119] Le Pleux L, Smeigh AL, Gibson E, Pellegrin Y, Blart E, Boschloo G, et al. Synthesis, photophysical and photovoltaic investigations of acceptor-functionalized perylene monoimide dyes for nickel oxide p-type dye-sensitized solar cells. Energy & Environmental Science. 2011;4:2075-84.

[120] Mori S, Fukuda S, Sumikura S, Takeda Y, Tamaki Y, Suzuki E, et al. Charge-transfer processes in dye-sensitized NiO solar cells. The Journal of Physical Chemistry C. 2008;112:16134-9.

[121] Odobel F, Le Pleux L, Pellegrin Y, Blart E. New photovoltaic devices based on the sensitization of p-type semiconductors: challenges and opportunities. Accounts of Chemical Research. 2010;43:1063-71.

[122] Zhu H, Hagfeldt A, Boschloo G. Photoelectrochemistry of mesoporous NiO electrodes in iodide/triiodide electrolytes. The Journal of Physical Chemistry C. 2007;111:17455-8.

[123] Li L, Gibson EA, Qin P, Boschloo G, Gorlov M, Hagfeldt A, et al. Double-layered NiO photocathodes for p-type DSSCs with record IPCE. Advanced Materials. 2010;22:1759-62.

[124] Powar S, Wu Q, Weidelener M, Nattestad A, Hu Z, Mishra A, et al. Improved photocurrents for p-type dye-sensitized solar cells using nano-structured nickel (II) oxide microballs. Energy & Environmental Science. 2012;5:8896-900.

[125] Xiong D, Wang H, Zhang W, Zeng X, Chang H, Zhao X, et al. Preparation of p-type $AgCrO_2$ nanocrystals through low-temperature hydrothermal method and the potential application in p-type dye-sensitized solar cell. Journal of Alloys and Compounds. 2015;642:104-10.

[126] Xiong D, Xu Z, Zeng X, Zhang W, Chen W, Xu X, et al. Hydrothermal synthesis of ultrasmall $CuCrO_2$ nanocrystal alternatives to NiO nanoparticles in efficient p-type dye-sensitized solar cells. Journal of Materials Chemistry. 2012;22:24760-8.

[127] Xiong D, Zhang W, Zeng X, Xu Z, Chen W, Cui J, et al. Enhanced performance of p-type dye-sensitized solar cells based on ultrasmall Mg-doped $CuCrO_2$ nanocrystals. ChemSusChem. 2013;6:1432-7.

[128] Nattestad A, Zhang X, Bach U, Cheng Y-B. Dye-sensitized $CuAlO_2$ photocathodes for tandem solar cell applications. Journal of Photonics for Energy. 2011;1:011103-9.

[129] Xu Z, Xiong D, Wang H, Zhang W, Zeng X, Ming L, et al. Remarkable photocurrent of p-type dye-sensitized solar cell achieved by size controlled $CuGaO_2$ nanoplates. Journal of Materials Chemistry A. 2014;2:2968-76.

[130] Huang Z, He M, Yu M, Click K, Beauchamp D, Wu Y. Dye-controlled interfacial electron transfer for high-current indium tin oxide photocathodes. Angewandte Chemie International Edition. 2015;54:6857-61.

[131] Shi Z, Lu H, Liu Q, Deng K, Xu L, Zou R, et al. $NiCo_2O_4$ Nanostructures as a promising alternative for NiO photocathodes in p-type dye-sensitized solar cells with high efficiency. Energy Technology. 2014;2:517-21.

[132] Yamaguchi T, Uchida Y, Agatsuma S, Arakawa H. Series-connected tandem dye-sensitized solar cell for improving efficiency to more than 10%. Solar Energy Materials and Solar Cells. 2009;93:733-6.

[133] Kinoshita T, Dy JT, Uchida S, Kubo T, Segawa H. Wideband dye-sensitized solar cells employing a phosphine-coordinated ruthenium sensitizer. Nature Photonics. 2013;7:535-9.

[134] Dürr M, Bamedi A, Yasuda A, Nelles G. Tandem dye-sensitized solar cell for improved power conversion efficiencies. Applied Physics Letters. 2004;84:3397-9.

[135] Yanagida M, Onozawa-Komatsuzaki N, Kurashige M, Sayama K, Sugihara H. Optimization of tandem-structured dye-sensitized solar cell. Solar Energy Materials and Solar Cells. 2010;94:297-302.

[136] He J, Lindström H, Hagfeldt A, Lindquist S-E. Dye-sensitized nanostructured tandem cell-first demonstrated cell with a dye-sensitized photocathode. Solar Energy Materials and Solar Cells. 2000;62:265-73.

[137] Nattestad A, Mozer AJ, Fischer MK, Cheng Y-B, Mishra A, Bäuerle P, et al. Highly efficient photocathodes for dye-sensitized tandem solar cells. Nature Materials. 2010;9:31-5.

[138] Liska P, Thampi K, Grätzel M, Bremaud D, Rudmann D, Upadhyaya H, et al. Nanocrystalline dye-sensitized solar cell/copper indium gallium selenide thin-film tandem showing greater than 15% conversion efficiency. Applied Physics Letters. 2006;88:203103.

[139] Jeong W-S, Lee J-W, Jung S, Yun JH, Park N-G. Evaluation of external quantum efficiency of a 12.35% tandem solar cell comprising dye-sensitized and CIGS solar cells. Solar Energy Materials and Solar Cells. 2011;95:3419-23.

[140] Wang W, Lin H, Zhang J, Li X, Yamada A, Konagai M, et al. Experimental and simulation analysis of the dye sensitized solar cell/Cu(In,Ga)Se_2 solar cell tandem structure. Solar Energy Materials and Solar Cells. 2010;94:1753-8.

[141] Moon SH, Park SJ, Kim SH, Lee MW, Han J, Kim JY, et al. Monolithic DSSC/CIGS tandem solar cell fabricated by a solution process. Scientific Reports. 2015;5.

[142] Ito S, Dharmadasa I, Tolan G, Roberts J, Hill G, Miura H, et al. High-voltage (1.8 V) tandem solar cell system using a GaAs/$Al_XGa_{(1-X)}$As graded solar cell and dye-sensitised solar cells with organic dyes having different absorption spectra. Solar Energy. 2011;85:1220-5.

[143] Snaith HJ, Ducati C. SnO_2-based dye-sensitized hybrid solar cells exhibiting near unity absorbed photon-to-electron conversion efficiency. Nano Letters. 2010;10:1259-65.

[144] Xia X, Li S, Wang X, Liu J, Wei Q, Zhang X. Structures and properties of SnO_2 nanofibers derived from two different polymer intermediates. Journal of Materials Science. 2013;48:3378-85.

[145] Kasaudhan R, Elbohy H, Sigdel S, Qiao H, Wei QF, Qiao QQ. Incorporation of TiO_2 nanoparticles into SnO_2 nanofibers for higher efficiency dye-sensitized solar cells. IEEE Electron Device Letters. 2014;35:578-80.

[146] Ahn SH, Kim DJ, Chi WS, Kim JH. One-dimensional hierarchical nanostructures of TiO_2 nanosheets on SnO_2 nanotubes for high efficiency solid-state dye-sensitized solar cells. Advanced Materials. 2013;25:4893-7.

[147] Kavan L, Grätzel M. Highly efficient semiconducting TiO_2 photoelectrodes prepared by aerosol pyrolysis. Electrochimica Acta. 1995;40:643-52.

[148] Liu M, Johnston MB, Snaith HJ. Efficient planar heterojunction perovskite solar cells by vapour deposition. Nature. 2013;501:395-8.

[149] Bard AJ, Faulkner LR. Electrochemical methods: fundamentals and applications: Wiley New York.

[150] O'Regan BC, Lenzmann F. Charge transport and recombination in a nanoscale interpenetrating network of n-type and p-type semiconductors: transient photocurrent and photovoltage studies of TiO_2/dye/CuSCN photovoltaic cells. The Journal of Physical Chemistry B. 2004;108:4342-50.

[151] O'Regan BC, Scully S, Mayer AC, Palomares E, Durrant J. The effect of Al_2O_3 barrier layers in TiO_2/dye/CuSCN photovoltaic cells explored by recombination and DOS characterization using transient photovoltage measurements. The Journal of Physical Chemistry B. 2005;109:4616-23.

[152] Snaith HJ, Moule AJ, Klein C, Meerholz K, Friend RH, Gratzel M. Efficiency enhancements in solid-state hybrid solar cells via reduced charge recombination and increased light capture. Nano Letters. 2007;7:3372-6.

[153] Wang X, Karanjit S, Zhang L, Fong H, Qiao Q, Zhu Z. Transient photocurrent and photovoltage studies on charge transport in dye sensitized solar cells made from the composites of TiO_2 nanofibers and nanoparticles. Applied Physics Letters. 2011;98:082114.

[154] Wijeratne K, Akilavasan J, Thelakkat M, Bandara J. Enhancing the solar cell efficiency through pristine 1-dimentional SnO_2 nanostructures: comparison of charge transport and carrier lifetime of SnO_2 particles vs. nanorods. Electrochimica Acta. 2012;72:192-8.

[155] Zhang Y, He X, Li J, Miao Z, Huang F. Fabrication and ethanol-sensing properties of micro gas sensor based on electrospun SnO_2 nanofibers. Sensors and Actuators B-Chemical. 2008;132:67-73.

[156] Birkel A, Lee Y-G, Koll D, Van Meerbeek X, Frank S, Choi MJ, et al. Highly efficient and stable dye-sensitized solar cells based on SnO_2 nanocrystals prepared by microwave-assisted synthesis. Energy & Environmental Science. 2012;5:5392-400.

[157] Gubbala S, Chakrapani V, Kumar V, Sunkara MK. Band-edge engineered hybrid structures for dye-sensitized solar cells based on SnO_2 nanowires. Advanced Functional Materials. 2008;18:2411-8.

[158] Sommeling PM, O'Regan BC, Haswell RR, Smit HJP, Bakker NJ, Smits JJT, et al. Influence of a $TiCl_4$ post-treatment on nanocrystalline TiO_2 films in dye-sensitized solar cells. Journal of Physical Chemistry B. 2006;110:19191-7.

[159] Singh J, Gusain A, Saxena V, Chauhan AK, Veerender P, Koiry SP, et al. XPS, UV-Vis, FTIR, and EXAFS Studies to investigate the binding mechanism of N719 dye onto oxalic acid treated TiO_2 and its implication on photovoltaic properties. The Journal of Physical Chemistry C. 2013;117:21096-104.

[160] Thapa A, Zai J, Elbohy H, Poudel P, Adhikari N, Qian X, et al. TiO_2 coated urchin-like SnO_2 microspheres for efficient dye-sensitized solar cells. Nano Research. 2014;7:1154-63.

[161] Zheng D, Lv M, Wang S, Guo W, Sun L, Lin C. A combined TiO_2 structure with nanotubes and nanoparticles for improving photoconversion efficiency in dye-sensitized solar cells. Electrochimica Acta. 2012;83:155-9.

[162] Fadadu KB, Soni SS. Spectral sensitization of TiO_2 by new hemicyanine dyes in dye solar cell yielding enhanced photovoltage: probing chain length effect on performance. Electrochimica Acta. 2013;88:270-7.

[163] Tiwana P, Docampo P, Johnston MB, Snaith HJ, Herz LM. Electron mobility and injection dynamics in mesoporous ZnO, SnO_2, and TiO_2 films used in dye-sensitized solar cells. ACS Nano. 2011;5:5158-66.

[164] Jung WH, Kwak N-S, Hwang TS, Yi KB. Preparation of highly porous TiO_2 nanofibers for dye-sensitized solar cells (DSSCs) by electro-spinning. Applied Surface Science. 2012;261:343-52.

[165] Adachi M, Sakamoto M, Jiu J, Ogata Y, Isoda S. Determination of parameters of electron transport in dye-sensitized solar cells using electrochemical impedance spectroscopy. The Journal of Physical Chemistry B. 2006;110:13872-80.

[166] Zhu Y, Murali S, Stoller MD, Ganesh K, Cai W, Ferreira PJ, et al. Carbon-based supercapacitors produced by activation of graphene. Science. 2011;332:1537-41.

[167] Lillo-Ródenas M, Cazorla-Amorós D, Linares-Solano A. Understanding chemical reactions between carbons and NaOH and KOH: an insight into the chemical activation mechanism. Carbon. 2003;41:267-75.

[168] Sun L, Tian C, Li M, Meng X, Wang L, Wang R, et al. From coconut shell to porous graphene-like nanosheets for high-power supercapacitors. Journal of Materials Chemistry A. 2013;1:6462-70.

[169] Wang Z, Zhang X, Liu X, Lv M, Yang K, Meng J. Co-gelation synthesis of porous graphitic carbons with high surface area and their applications. Carbon. 2011;49:161-9.

[170] Naebe M, Wang J, Amini A, Khayyam H, Hameed N, Li LH, et al. Mechanical property and structure of covalent functionalised graphene/epoxy nanocomposites. Scientific Reports. 2014;4:4375.

[171] Zhao C, Chen X, Zhao C, Liu Y. Carbonation and hydration characteristics of dry potassium-based sorbents for CO_2 capture. Energy & Fuels. 2009;23:1766-9.

[172] Xu Z, Ao Z, Chu D, Younis A, Li CM, Li S. Reversible hydrophobic to hydrophilic transition in graphene via water splitting induced by UV irradiation. Scientific Reports. 2014;4:6450.

[173] Zimmermann E, Ehrenreich P, Pfadler T, Dorman JA, Weickert J, Schmidt-Mende L. Erroneous efficiency reports harm organic solar cell research. Nature Photonics. 2014;8:669-72.

[174] Snaith HJ. How should you measure your excitonic solar cells? Energy & Environmental Science. 2012;5:6513-20.

[175] Yen M-Y, Teng C-C, Hsiao M-C, Liu P-I, Chuang W-P, Ma C-CM, et al. Platinum nanoparticles/graphene composite catalyst as a novel composite counter electrode for high performance dye-sensitized solar cells. Journal of Materials Chemistry. 2011;21:12880-8.

[176] Wang G, Xing W, Zhuo S. Application of mesoporous carbon to counter electrode for dye-sensitized solar cells. Journal of Power Sources. 2009;194:568-73.

[177] Hauch A, Georg A. Diffusion in the electrolyte and charge-transfer reaction at the platinum electrode in dye-sensitized solar cells. Electrochimica Acta. 2001;46:3457-66.

[178] Ju MJ, Jeon IY, Kim JC, Lim K, Choi HJ, Jung SM, et al. Graphene nanoplatelets doped with N at its edges as metal-free cathodes for organic dye-sensitized solar cells. Advanced Materials. 2014;26:3055-62.

[179] Raga SR, Fabregat-Santiago F. Temperature effects in dye-sensitized solar cells. Physical Chemistry Chemical Physics. 2013;15:2328-36.

[180] Soedergren S, Hagfeldt A, Olsson J, Lindquist S-E. Theoretical models for the action spectrum and the current-voltage characteristics of microporous semiconductor films in photoelectrochemical cells. The Journal of Physical Chemistry. 1994;98:5552-6.

[181] Boschloo G, Hagfeldt A. Characteristics of the iodide/triiodide redox mediator in dye-sensitized solar cells. Accounts of Chemical Research. 2009;42:1819-26.

[182] Nazeeruddin MK, Kay A, Rodicio I, Humphry-Baker R, Mueller E, Liska P, et al. Conversion of light to electricity by cis-X_2bis(2,2'-bipyridyl-4,4'-dicarboxylate)ruthenium(II) charge-transfer sensitizers (X = Cl^-, Br^-, I^-, CN^-, and SCN^-) on nanocrystalline titanium dioxide electrodes. Journal of the American Chemical Society. 1993;115:6382-90.

[183] Murakoshi K, Kano G, Wada Y, Yanagida S, Miyazaki H, Matsumoto M, et al. Importance of binding states between photosensitizing molecules and the TiO_2 surface for efficiency in a dye-sensitized solar cell. Journal of Electroanalytical Chemistry. 1995;396:27-34.

[184] Oda T, Tanaka S, Hayase S. Differences in characteristics of dye-sensitized solar cells containing acetonitrile and ionic liquid-based electrolytes studied using a novel model. Solar Energy Materials and Solar Cells. 2006;90:2696-709.

[185] Gong J, Sumathy K. A theoretical study on third generation photovoltaic technology: dye-sensitized solar cells. International Conference on Renewable Energies and Power Quality (ICREPQ'12); 2012 Mar 28-30; Santiago de Compostela, Spain.

[186] Zhou Z, Sigdel S, Gong J, Vaagensmith B, Elbohy H, Yang H, et al. Graphene-beaded carbon nanofibers with incorporated Ni nanoparticles as efficient counter-electrode for dye-sensitized solar cells. Nano Energy. 2016;22:558-63.

[187] Ni M, Leung MKH, Leung DYC. Theoretical modelling of the electrode thickness effect on maximum power point of dye-sensitized solar cell. Canadian Journal of Chemical Engineering. 2008;86:35-42.

[188] Noh SI, Ahn HJ, Riu DH. Photovoltaic property dependence of dye-sensitized solar cells on sheet resistance of FTO substrate deposited via spray pyrolysis. Ceramics International. 2012;38:3735-9.

[189] Koide N, Islam A, Chiba Y, Han L. Improvement of efficiency of dye-sensitized solar cells based on analysis of equivalent circuit. Journal of Photochemistry and Photobiology A: Chemistry. 2006;182:296-305.

[190] Amiri O, Salavati-Niasari M. High efficiency dye-sensitized solar cells (9.3%) by using a new compact layer: decrease series resistance and increase shunt resistance. Materials Letters. 2015;160:24-7.

[191] Rock SE, Shi X, Garland JE, Roy D. Experimental considerations for temperature controlled measurements of fast charge recombination times in dye sensitized solar cells using open circuit voltage decay and impedance spectroscopy. Measurement. 2014;53:71-82.

[192] Usami A, Seki S, Mita Y, Kobayashi H, Miyashiro H, Terada N. Temperature dependence of open-circuit voltage in dye-sensitized solar cells. Solar Energy Materials and Solar Cells. 2009;93:840-2.

[193] Macaira J, Andrade L, Mendes A. Modeling, simulation and design of dye sensitized solar cells. RSC Advances. 2014;4:2830-44.

[194] Daeneke T, Uemura Y, Duffy NW, Mozer AJ, Koumura N, Bach U, et al. Aqueous dye-sensitized solar cell electrolytes based on the ferricyanide-ferrocyanide redox couple. Advanced Materials. 2012;24:1222-5.

[195] Yum J-H, Baranoff E, Kessler F, Moehl T, Ahmad S, Bessho T, et al. A cobalt complex redox shuttle for dye-sensitized solar cells with high open-circuit potentials. Nature Communication. 2012;3:631.

[196] Papageorgiou N, Maier W, Grätzel M. An iodine/triiodide reduction electrocatalyst for aqueous and organic media. Journal of the Electrochemical Society. 1997;144:876-84.

[197] Zheng M, Huo J, Tu Y, Wu J, Hu L, Dai S. Flowerlike molybdenum sulfide/multi-walled carbon nanotube hybrid as Pt-free counter electrode used in dye-sensitized solar cells. Electrochimica Acta. 2015;173:252-9.

[198] Papageorgiou N, Athanassov Y, Armand M, Bonho P, Pettersson H, Azam A, et al. The performance and stability of ambient temperature molten salts for solar cell applications. Journal of the Electrochemical Society. 1996;143:3099-108.

[199] Vetter KJ. Elektrochemische kinetik: Springer-Verlag; 2013.

[200] Tang Q, Wang X, Yang P, He B. A solar cell that is triggered by sun and rain. Angewandte Chemie International Edition. 2016;55:5243-6.

[201] Seo SH, Jeong EJ, Han JT, Kang HC, Cha SI, Lee DY, et al. Efficient low-temperature transparent electrocatalytic layers based on graphene oxide nanosheets for dye-sensitized solar cells. ACS Applied Materials & Interfaces. 2015;7:10863-71.

APPENDIX A. NUMERICAL ASPECTS

In relaxation methods we replace ODEs by approximate finite-difference equations (FDEs) on a grid or mesh of points that spans the domain of interest.

As a typical example, we could replace a general first-order differential equation

$$\frac{dy}{dx} = g(x, y) \tag{A.1}$$

with an algebraic equation relating function values at two points k, $k-1$:

$$y_k - y_{k-1} - (x_k - x_{k-1}) g\left[\frac{1}{2}(x_k + x_{k-1}), \frac{1}{2}(y_k + y_{k-1})\right] = 0 \tag{A.2}$$

When the problem involves N coupled first-order ODEs represented by FDEs on a mesh of M points, a solution consists of values for N dependent functions given at each of the M mesh points, or $N \times M$ variables in all. The relaxation method determines the solution by starting with a guess and improving it, iteratively. As the iterations improve the solution, the results is said to relax to the true solution.

We use the notation $\boldsymbol{y}_k$ to refer to the entire set of dependent variables $y_1, y_2, \ldots, y_N$ at point x_k. At an arbitrary point k in the middle of the mesh, we approximate the set of N first-order ODEs by algebraic relations of the form

$$0 = \boldsymbol{E}_k \equiv \boldsymbol{y}_k - \boldsymbol{y}_{k-1} - (x_k - x_{k-1}) \boldsymbol{g}_k(x_k, x_{k-1}, \boldsymbol{y}_k, \boldsymbol{y}_{k-1}), k = 2,3, \ldots, M \tag{A.3}$$

Thus the FDEs provide a total of $(M-1)N$ equations for the MN unknowns. The remaining N equations come from the boundary conditions.

At the first boundary we have

$$0 = \boldsymbol{E}_1 \equiv \boldsymbol{B}(x_1, \boldsymbol{y}_1) \tag{A.4}$$

While at the second boundary

$$0 = \boldsymbol{E}_{M+1} \equiv \boldsymbol{C}(x_M, \boldsymbol{y}_M) \tag{A.5}$$

Equations for the increments are developed by expanding the FDEs in first-order Taylor series with respect to small changes $\Delta\mathbf{y}_k$. At an interior point, $k = 2,3,\ldots,M$ this gives:

$$\mathbf{E}_k(\mathbf{y}_k + \Delta\mathbf{y}_k, \mathbf{y}_{k-1} + \Delta\mathbf{y}_{k-1}) \approx \mathbf{E}_k(\mathbf{y}_k, \mathbf{y}_{k-1}) + \sum_{n=1}^{N} \frac{\partial \mathbf{E}_k}{\partial y_{n,k-1}} \Delta y_{n,k-1} + \sum_{n=1}^{N} \frac{\partial \mathbf{E}_k}{\partial y_{n,k}} \Delta y_{n,k} \tag{A.6}$$

For a solution we want the updated value $\mathbf{E}(\mathbf{y} + \Delta\mathbf{y})$ to be zero, so the general set of equations at an interior point can be written in matrix form as

$$\sum_{n=1}^{N} S_{j,n} \Delta y_{n,k-1} + \sum_{n=N+1}^{2N} S_{j,n} \Delta y_{n-N,k} = -E_{j,k}, \qquad j = 1,2,\ldots,N \tag{A.7}$$

where

$$S_{j,n} = \frac{\partial E_{j,k}}{\partial y_{n,k-1}}, \qquad S_{j,n+N} = \frac{\partial E_{j,k}}{\partial y_{n,k}}, \qquad n = 1,2,\ldots,N \tag{A.8}$$

APPENDIX B. LIST OF PUBLICATIONS

1. Gong J, Sumathy K, Zhou Z, Qiao Q. Modeling of interfacial and bulk charge transfer in dye-sensitized solar cells. Cogent Engineering, 4(1): 1287231, 2017.

2. Gong J, Sumathy K, Zhou Z, Qiao Q. Review on dye-sensitized solar cells (DSSCs): advanced techniques and research trends. Renewable & Sustainable Energy Reviews, 68(1):234-246, 2017.

3. Gong J, Zhou Z, Sumathy K, Yang H, Qiao Q. Activated graphene nanoplatelets as a counter electrode for dye-sensitized solar cells. Journal of Applied Physics, 119(13):135501, 2016.

4. Gong J, Qiao H, Sigdel S, Elbohy H, Adhikari N, Zhou Z, Sumathy K, Wei Q, Qiao Q. Characteristics of SnO_2 nanofiber/TiO_2 nanoparticle composite for dye-sensitized solar cells. AIP Advances, 15(6):067134, 2015.

5. Gong J, with Sigdel S, Elbohy H, Adhikari N, Sumathy K, Qiao H, Wei Q, Sayyad MH, Zai J, Qian X, Qiao Q. Dye-sensitized solar cells based on porous hollow tin oxide nanofibers. IEEE Transactions on Electron Devices, 62(6):2027-2032, 2015.

6. Gong J, Sumathy K, Zhou Z, Qiao Q. Effect of graphene nanoplatelet thickness on electrochemical performance of dye-sensitized solar cell. Proceeding of 2016 IEEE Intentional Conference on Electro/Information Technology (IEEE eit2016), Grand Forks, North Dakota, USA, May 19-21, 2016. (Invited Talk)

7. Gong J, Qiao Q, Sumathy K. Porous SnO_2 nanofiber network for energy efficient dye-sensitized solar cells. International Mechanical Engineering Congress & Exposition (IMECE'15), Houston, USA, November 17-19, 2015. (Technical Presentation)

8. Zhou Z, Sigdel S, Gong J, Vaagensmith B, Elbohy H, Yang H, Sumathy K, Wu XF, Qiao Q. Graphene-beaded carbon nanofibers with incorporated Ni nanoparticles as efficient counter-electrode for dye-sensitized solar cells. Nano Energy, 22:558-563, 2016.